UNIVERSITÀ DEGLI STUDI DELL'AQUILA
DIPARTIMENTO DI SCIENZE FISICHE E CHIMICHE

Dottorato di Ricerca in Scienze Fisiche e Chimiche

XXXIII ciclo

Polarization-entanglement distribution
in fiber-optic channels

SSD FIS/03

Dottorando

Gabriele Riccardi

<table>
<tr><td>Coordinatore del corso</td><td>Tutor</td></tr>
<tr><td>Prof. Antonio Mecozzi</td><td>Prof. Antonio Mecozzi</td></tr>
<tr><td></td><td>Prof. Cristian Antonelli</td></tr>
<tr><td></td><td>Prof. Michael Brodsky</td></tr>
</table>

A.A. 2019/2020

Contents

Abstract

Entanglement is a key ingredient in many quantum communication protocols, and robust quantum channels are needed for its fast and reliable distribution over long distances. As quantum communication technology matures, it moves towards utilizing actual fibers, which leads to a growing need for physical models describing decoherence and the other effects that take place in this kind of media.

In this work, we analyze how two phenomena that are ever-present in fiber-optic based networks, namely *polarization-mode dispersion* (PMD) and *polarization-dependent loss* (PDL), affect the distribution of polarization-entangled photons. The former represents the main source of decoherence in a fiber-optic channel, while the latter is an example of modal filtering.

We start by considering the distribution of polarization-entangled photon pairs through optical fibers where PMD acts as a decoherence mechanism. We analyze both the case in which PMD is present in the channel of one photon only, and the case in which the propagation of both photons is affected by PMD. We quantify the entanglement quality of the received two-photon states by means of a well known entanglement metric, known as *concurrence*, and we analyze how this is impacted by the main system parameters. We also develop a a treatment of this problem in the framework of quantum information theory, where the total correlations between different parts of a system are quantified by making use of the von Neumann entropy and the quantum mutual information. We discuss the concept of nonlocal PMD compensation and quantify its beneficial effect on entanglement in terms of concurence and quantum mutual information restoration.

We then move on to analyzing the case in which PMD and PDL are present in the channel of one photon of a polarization-entangled pair. The primary challenge when dealing with these combined effects is to concisely account for numerous elements that in general are distributed along a lengthy optical path. We approach this by starting with an analytical model of a channel with just two lumped elements, one representing PMD and the other representing PDL. Interestingly, we find that, while the order and relative orientation of the two elements produce a wealth of different biphoton states, the amount of entanglement in all those states is exactly the same, a result that we explained also in simple, intuitive terms. Then, we conduct experiments that implement this channel and verify our analytical findings. We turn our attention to the most general fiber polarization channel, comprised of a statistically

significant number of arbitrarily oriented elements. We show that, over an ample range of parameters, our two-element analytical model is quite accurate in describing the fiber channel, which makes it an effective tool for gaining insights into channel decoherence. We conclude this part by extending the analysis to the case in which PDL affects the propagation of both photons, in conjunction with PMD in one optical path.

Finally, we show how the presence of PMD and PDL alone can lead to the formation of peculiar entangled states that can't be detected by a conceptually simple and experimentally prevalent class of entanglement witnesses, known as fidelity witnesses. These states, usually referred to as *unfaithful* states, are exceedingly common among bipartite states, especially for higher dimensional systems. In this work, we show that even among two-qubit states, the simplest of all entangled states, unfaithful states can be created through a suitable application of PMD and PDL to a Bell state. We also show that the faithfulness is not monotonic to entanglement, as measured by the concurrence. Finally, we experimentally verify our predictions and specifically demonstrate a situation where an unfaithful state is brought to faithfulness at the expense of further reducing the entanglement of the state.

Publications

Papers appended to this thesis:

1. G. Riccardi, D. E. Jones, X.D. Yu, O. Gühne, B. T. Kirby, "Exploring the relationship between the faithfulness and entanglement of two qubits," *Physical Review A* **103** (4), 042417 (2021).

2. G. Riccardi, C. Antonelli, D. E. Jones, M. Brodsky, "Simultaneous Decoherence and Mode Filtering in Quantum Channels: Theory and Experiment," *Physical Review Applied* **15** (1), 014060 (2021).

3. D.E. Jones, B.T. Kirby, G. Riccardi, C. Antonelli, M. Brodsky, "Exploring classical correlations in noise to recover quantum information using local filtering," *New Journal of Physics* **22** (7), 073037 (2020).

Papers not appended to this thesis:

1. C. Antonelli, G. Riccardi, T. Hayashi, A. Mecozzi, "Role of polarization-mode coupling in the crosstalk between cores of weakly-coupled multi-core fibers," *Optics express* **28** (9), 12847-12861 (2020).

Conference papers and contributed talks:

C1 G. Riccardi, C. Antonelli, D.E. Jones, M. Brodsky, "Polarization-entaglement distribution in fiber-optic channels," SPIE – Photonics West 2021, Quantum Computing, Communication, and Simulation. Vol. 11699. International Society for Optics and Photonics (Invited Talk).

C2 G. Riccardi, C. Antonelli, D.E. Jones, M. Brodsky, "Directional asymmetry of quantum channels," Frontiers in Optics 2020 – Optical Society of America, paper FM7A. 7.

C3 D. E. Jones, G. Riccardi, B.T. Kirby, C. Antonelli, and M. Brodsky, "Entanglement preservation based on classical correlations," Conference on Lasers and Electro-Optics, OSA Technical Digest (Optical Society of America, 2020), paper FTh1D.3.

C4 G. Riccardi, C. Antonelli, D.E. Jones, M. Brodsky, "Reproducing the most general

quantum channel in the lab: is it possible?," IEEE Photonics Conference (IPC) 2020 (pp. 1-2).

C5 D.E. Jones, G. Riccardi, C. Antonelli, M. Brodsky, "Mapping quantum channel decoherence," IEEE Photonics Conference (IPC) 2020 (pp. 1-2).

C6 D.E. Jones, C. Antonelli, G. Riccardi, M. Brodsky, B.T. Kirby, "Upper bound on mutual quantum information between two partially mixed qubits," IEEE Photonics Conference (IPC) 2020 (pp. 1-2).

C7 G. Riccardi, B.T. Kirby, D.E. Jones, C. Antonelli and M. Brosdky, "Quantification of Information Loss and Recovery in Nonlocal PMD Compensation," Italian Conference on Optics and Photonics 2020 (Talk).

C8 G. Riccardi, B.T. Kirby, C. Antonelli, M. Brodsky, "An information-theoretical treatment of nonlocal PMD compensation," SPIE – Photonics West 2020, Quantum Computing, Communication, and Simulation. Vol. 11295, paper 112950T. International Society for Optics and Photonic.

Introduction

The ability to generate and distribute quantum entanglement among distant locations is of great relevance in numerous quantum protocols. Entanglement distribution is at the basis of many applications of quantum information science, ranging from quantum cryptography to metrology and sensing. Thus, robust quantum channels are needed for fast and reliable distribution of entanglement over long distances.

In the context of distributing entanglement, polarization-entangled photon pairs are particularly useful because of the ease with which light polarization can be manipulated using off-the-shelf equipment, and the numerous sources of polarization-entangled photon pairs suitable for use with standard single-mode fibers (SLM). However, polarization entanglement is rather fragile, and can be significantly degraded by the presence of decoherence and modal filtering mechanisms. In fiber-optic communications, the former manifests itself in the form of polarization-mode dispersion (PMD), which originates from the presence of random birefringence in the fiber, and the latter in the form of polarization-dependent loss (PDL). The joint presence of these two effects in a fiber-optic channel creates complex phenomena, whose description is rather involved, mostly because PMD and PDL accumulate in a random fashion along the channel. The study we propose here intends to solve this complexity with the introduction of a simple, but physically representative model for the description of how the joint action of PMD and PDL affects the distribution of polarization-entangled photons. It is important to notice that even if PMD and PDL concern specifically fiber-optic communications, as mentioned before they are actually representative of more general phenomena that affect every kind of quantum communications, namely decoherence and modal filtering, respectively. The results obtained here can thus be adapted rather straightforwardly to other scenarios.

The thesis is organized as follows. In the first two Chapters, we introduce some concepts that are useful to understand the main results presented later in detail. Specifically, in Chapter 1 we provide the reader with some of the basics of quantum mechanics and quantum information theory. The density matrix formalism is introduced to represent the state of a system, and the representation for two-qubits states is derived. We describe the concept of entanglement, and give some insights into how it can be characterized. Then, von Neumann entropy and quantum mutual information are used to build entropic Venn diagrams, which allow one to graphically represent how the information is distributed among different parts

of a system. In Chapter 2 we review the fundamentals of PMD and PDL, with a particular focus on the quantities that are used in the subsequent chapters. We give a qualitative description of birefringence and mode coupling, and we define the PMD vector, which in the framework of the so-called first-order picture can be used to characterize completely the PMD of a fiber. After obtaining the dynamical PMD equation, we move on with the description of the main PDL parameters, and we briefly explain the complexity in the joint description of PMD and PDL.

In Chapter 3 the effect of PMD on polarization-entangled photons is thoroughly investigated. We start with the description of a simple scenario involving a single photon propagating in a channel affected by the presence of PMD. We then move on to describing how the presence of PMD impacts the degree of entanglement of a polarization-entangled two-photon state. We cover both the case in which only one of the two photons experiences PMD (while the other one is kept in proximity of the source), and the case in which both photons travel through channels affected by PMD. We show how the use of additional controlled PMD in one of the two optical paths can restore the original degree of entanglement fully or in part, depending on the system configuration, in a nonlocal fashion. Using the quantum analog of the Shannon entropy, the von Neumann entropy, we evaluate the quantum mutual information of propagated polarization-entangled photon pairs as a function of the fiber-channel PMD, and quantify the beneficial effect of nonlocal PMD compensation in terms of mutual quantum information restoration. We use the graphical aid of entropic Venn diagrams introduced in Chapter 1 to show how the presence of PMD causes flow of information towards the environment as the polarization of the photons gets coupled with the time-dependent part of the state.

In Chapter 4 we focus on the joint effect of PMD and PDL in a quantum channel. We start by introducing a simple but representative two-element model, and use it to describe the case in which PMD and PDL affect the propagation of one photon in a Bell state, while the second photon is kept in the proximity of the source. We investigate the role played by the orientation and the ordering in which the two effects act on the photon, and we compare the accuracy of our model in describing the way in which the concurrence of the state is affected with respect to a general polarization channel. Finally, we explore the scenario in which a PDL element is also present in the path of the second photon, discussing the effectiveness of nonlocal PDL compensation and its consequences on the design of an optical network.

To conclude this work, in Chapter 5 we focus on a specific class of entanglement witnesses, which are based on fidelity. We introduce the concept of faithfulness, and show how simple application of PMD and PDL on a pair of entangled qubits can lead to the formation of unfaithful entanglement, that is, entangled states that can't be detected by any fidelity witness. We reproduce this scenario experimentally, and we show how certain unfaithful

states can be made detectable at the cost of further reducing their entanglement.

Basic concepts of quantum mechanics and quantum information

In this chapter some basic concepts of quantum mechanics and quantum information are introduced that will be useful in the comprehension of the text. We start by introducing the density matrix formalism and describing two-level systems, both of paramount importance in the definition of a *qubit*. We then briefly explain the concept of entanglement and discuss the properties that an entanglement measure should satisfy, to introduce the well-known metric *concurrence*. We give some hints of quantum information theory, defining the von Neumann entropy and the quantum mutual information, and introduce the reader to the entropic Venn diagrams, which provide us with the possibility of visualizing how information is shared between different parts of a system. Finally, we conclude the Chapter discussing how the evolution of a state can be represented by quantum channels, and discuss their properties. All the sections in this chapter represent a review of existing literature.

1.1 The density matrix

Pure states are ensembles of physical systems represented (using the Dirac notation) by the same *ket* $|\psi\rangle$ that belongs to a Hilbert space $\mathcal{H}$. When dealing with practical situations, it is pretty rare to encounter pure states, and it is way more likely that one has to work with mixed ensembles, in which a certain portion of the system is in the state $|\psi_1\rangle$, another in the state $|\psi_2\rangle$, and so on. A useful way to describe mixed states (as well as pure ones) was introduced by John von Neumann in 1927 [1]: the density operator, representend in some basis by the density matrix.

Suppose to have N ensembles, n_i of which described by the state vector $|\psi_i\rangle$; the expected value of an observable A evaluated on the mixture will be equal to the sum of the expected values of A on the states $|\psi_i\rangle$ that make up the mixture, each of which multiplied by the

corresponding probability p_i.

$$\langle A \rangle = \sum_i p_i \langle \psi_i | A | \psi_i \rangle, \tag{1.1}$$

where

$$p_i = \frac{n_i}{N} \quad \text{and} \quad \sum_i p_i = 1.$$

Using a generic basis $\{|\phi_k\rangle\}$, the expected vaue of A can be written as:

$$\langle A \rangle = \sum_i \sum_k p_i \langle \psi_i | \phi_k \rangle \langle \phi_k | A | \psi_i \rangle = \sum_i \sum_k p_i \langle \phi_k | A | \psi_i \rangle \langle \psi_i | \phi_k \rangle$$
$$= \sum_k \langle \phi_k | \left[\sum_i p_i | \psi_i \rangle \langle \psi_i | \right] A | \phi_k \rangle. \tag{1.2}$$

This line of reasoning leads to define the density operator as:

$$\rho \equiv \sum_i p_i | \psi_i \rangle \langle \psi_i |, \tag{1.3}$$

which, in turn, means that the expected value of A on the mixture described by the density matrix ρ can be expressed as

$$\langle A \rangle = \sum_k \langle \phi_k | \rho A | \phi_k \rangle = \text{Tr}(\rho A), \tag{1.4}$$

where $\text{Tr}(\cdot)$ denotes the trace operation[1].

The density matrix has the following properties [2]:

$$\rho^\dagger = \rho \qquad \qquad \text{(hermiticity)} \tag{1.5a}$$

$$\text{Tr}(\rho) = 1 \qquad \qquad \text{(unit trace)} \tag{1.5b}$$

$$\rho \geq 0 \qquad \qquad \text{(positive semidefinite)} \tag{1.5c}$$

According to this definition, the density operator fully describes the physical system under study, whether this is a mixture of states or a pure state. In the latter scenario, the density matrix will just be

$$\rho_i \equiv | \psi_i \rangle \langle \psi_i |, \tag{1.6}$$

and it will thus be possible to express the density matrix of a mixture of states as the convex

---

[1]A really useful property of the trace operation when working with density matrices is the cyclic invariance, that is, given three matrices A, B e C one has $\text{Tr}(ABC) = \text{Tr}(CAB) = \text{Tr}(BCA)$. This property also implies that the trace is invariant under unitary transformations: $\text{Tr}(U^\dagger A U) = \text{Tr}(A)$

sum of density matrices of pure states

$$\rho^{\mathrm{mix}} = \sum_i p_i \rho_i. \tag{1.7}$$

It is also worth noticing that if the state is pure (and only when it's pure) the following relation holds:

$$\mathrm{Tr}(\rho^2) = 1. \tag{1.8}$$

The equation that rules the time evolution of a density matrix can be obtained starting from the Schrödinger equation; in fact, for a mixture described by the density matrix ρ, one can write

$$
\begin{aligned}
i\hbar \frac{\partial}{\partial t}\rho &= i\hbar \sum_i p_i(|\dot{\psi}_i\rangle \langle \psi_i| + |\psi_i\rangle \langle \dot{\psi}_i|) \\
&= \sum_i p_i(H\rho_i - \rho_i H) = [H, \rho],
\end{aligned}
\tag{1.9}
$$

or

$$\frac{\partial}{\partial t}\rho = -\frac{i}{\hbar}[H, \rho] \tag{1.10}$$

which is known as von Neumann equation. The solution to (1.10) can always be expressed as

$$\rho(t) = U\rho(0)U^\dagger, \tag{1.11}$$

where

$$U(t, t_0) = e^{-\frac{i}{\hbar}H(t - t_0)} \tag{1.12}$$

is the *propagator*, meaning that the time evolution of the expected value of an operator can be evaluated by letting either the operator itself or the density matrix propagate (the former being equivalent to the Heisenberg picture, while the latter corresponds to the Schrödinger picture). This can be easily shown by making use of the cyclic invariance of the trace and the definition of expected value in terms of the density matrix:

$$
\begin{aligned}
\langle A(t) \rangle &= \mathrm{Tr}[A\rho(t)] \\
&= \mathrm{Tr}[AU\rho(0)U^\dagger] \\
&= \mathrm{Tr}[A(t)\rho(0)].
\end{aligned}
\tag{1.13}
$$

1.2   Two-level systems

The *ket* representing a state can always be expressed by a column vector in a certain basis; the components of this vector are simply the coefficients in the expansion in said basis.

When the dimensionality of the space is two (as in the case of spin-$\frac{1}{2}$ particles or photons' polarization) it will be possible to express a generic state $|\psi\rangle$ as a linear combination of the basis *kets* $|0\rangle$ and $|1\rangle$, and thus use a two-dimensional vector. The basis vectors can be expressed as:

$$|0\rangle \equiv \begin{pmatrix} 1 \\ 0 \end{pmatrix} \quad \text{and} \quad |1\rangle \equiv \begin{pmatrix} 0 \\ 1 \end{pmatrix} \tag{1.14}$$

The state $|\psi\rangle$ will thus be in the form:

$$|\psi\rangle = \alpha |0\rangle + \beta |1\rangle \equiv \begin{pmatrix} \alpha \\ \beta \end{pmatrix} \tag{1.15}$$

with

$$|\alpha|^2 + |\beta|^2 = 1.$$

One usually refers to column vectors, such as the one in (1.15), as two-components spinors, which belong to a two-dimensional Hilbert space. The coefficients α e β are generally complex; it will thus be possible to express them as

$$\alpha \equiv r_0 e^{i\phi_0}, \qquad \beta \equiv r_1 e^{i\phi_1},$$

so that the state $|\psi\rangle$ becomes

$$|\psi\rangle = r_0 e^{i\phi_0} |0\rangle + r_1 e^{i\phi_1} |1\rangle,$$

where the normalization implies

$$r_0^2 + r_1^2 = 1.$$

By making use of the angle δ one can express the absolute values of α e β as $r_0 = \cos(\delta)$ and $r_1 = \sin(\delta)$. Equating $\delta = \theta/2$ we have:

$$|\psi\rangle = e^{i\gamma}(\cos(\theta/2) |0\rangle + e^{i\varphi} sin(\theta/2) |1\rangle), \tag{1.16}$$

with $\varphi = \phi_1 - \phi_0$ and $\gamma = \phi_0$, $0 \leq \phi \leq 2\pi$. Since the global phase $e^{i\gamma}$ is physically immaterial, it can be ignored, leading to:

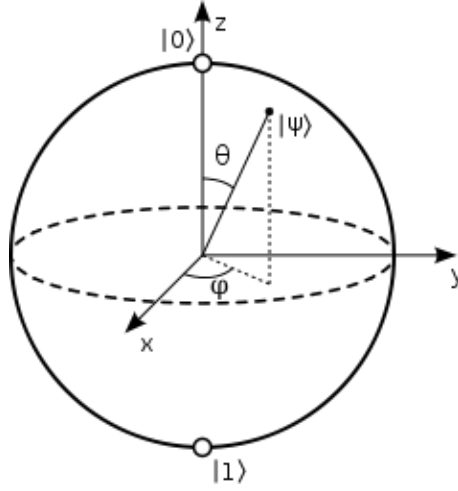$$|\psi\rangle = \cos(\theta/2) |0\rangle + e^{i\varphi} \sin(\theta/2) |1\rangle. \tag{1.17}$$

Figure 1.1: The Bloch sphere.

Since the two-level system in Eq.(1.17) is fully characterized by the angles θ and ϕ, all the
states can be represented as unit-length vectors on the surface of a sphere, called the *Bloch
sphere.* [2]. In this representation, the angles θ and ϕ in (1.17) thus coincide with the spherical
coordinates, and a one-to-one relation between the points of the Bloch sphere and the states
described by (1.17) is established: the North pole usually corresponds to $|0\rangle$, the South pole
to $|1\rangle$, and all the other points are combinations of the two. All the unit-length vectors
represent pure states, while mixed states have a length that is less than unity, and are thus
represented by points within the sphere.

For two-level systems, the density operator introduced in Section 1.1 is a 2×2 matrix;
according to the properties (1.5), this matrix is Hermitian and has unit trace, and is thus
fully described by three independent real-valued parameters. If the state is pure, again one
only needs two parameters, as the density matrix corresponding to the state (1.17) becomes

$$\rho = \begin{pmatrix} \cos^2 \frac{\theta}{2} & \cos \frac{\theta}{2} \sin \frac{\theta}{2} e^{-i\varphi} \\ e^{i\varphi} \sin \frac{\theta}{2} \cos \frac{\theta}{2} & \sin^2 \frac{\theta}{2} \end{pmatrix}. \tag{1.18}$$

The density matrices belong to a Hilbert-Schmidt space. For two-dimensional systems, one

---

[2]The Bloch sphere is equivalent to the *Poincaré sphere*, used in classical optics to describe the state of
polarization of light, and to which we will refer in Chapter 2.

usually picks the basis composed of the three Pauli matrices

$$\sigma_x = \sigma_1 = \begin{pmatrix} 0 & 1 \\ 1 & 0 \end{pmatrix}, \qquad \sigma_y = \sigma_2 = \begin{pmatrix} 0 & -i \\ i & 0 \end{pmatrix}, \qquad \sigma_z = \sigma_3 = \begin{pmatrix} 1 & 0 \\ 0 & -1 \end{pmatrix},$$

along with the identity matrix $\mathbb{I}$. Every density matrix can thus be expressed as a linear combination of the matrices of the basis as

$$\rho = \sum_{i=0}^{3} \frac{1}{2} \operatorname{Tr}[\rho \sigma_i] \sigma_i, \qquad (1.19)$$

where $\sigma_0 \equiv \mathbb{I}$. Defining $n_i \equiv tr[\rho \sigma_i]$ leads to

$$\rho = \frac{\mathbb{I} + \hat{n} \cdot \vec{\sigma}}{2} \qquad (1.20)$$

where

$$\hat{n} = \begin{pmatrix} n_x \\ n_y \\ n_z \end{pmatrix}, \qquad \vec{\sigma} = \begin{pmatrix} \sigma_x \\ \sigma_y \\ \sigma_z \end{pmatrix}.$$

The coefficients n_i, which fully describe the state, are the coordinates of a point on a Bloch sphere, and can directly be measured (since the basis made of the Pauli matrices is hermitian) as $n_i = \langle \sigma_i \rangle$, so that for pure states one can write

$$\hat{n} = \langle \psi | \vec{\sigma} | \psi \rangle. \qquad (1.21)$$

Multi-qubit states belong to the composite space that is the tensor product of Hilbert spaces $\mathcal{H}_1 \otimes \mathcal{H}_2 \otimes \ldots \otimes \mathcal{H}_n$. The notation we have just introduced can be extended to cover the case of multiple qubits by taking the tensor product of all the combinations of single-qubit Pauli matrices as

$$\frac{1}{2^n} \sum_{i_1,\ldots,i_n}^{3} a_{i_1,\ldots,i_n} \sigma_{i_1} \otimes \ldots \otimes \sigma_{i_n}, \qquad (1.22)$$

where n is the number of qubits (in most of what follows we will have $n = 2$) and the normalization coefficient $\frac{1}{2^n}$ arises from the fact that the only non traceless combination of Pauli matrices is $\sigma_0 \otimes \ldots \otimes \sigma_0$, whose trace equals 2^n. Again, all the coefficients in the expansion are real-valued and can be expressed as $a_{i_1,\ldots,i_n} = \langle \sigma_{i_1} \otimes \ldots \otimes \sigma_{i_n} \rangle$.

It might happen that one only has access to a number $k < n$ of parties. This is the case

when, for example, one is limited to measure in the laboratory at most k different subsystems at the same time. The state of this subsystem can be obtained by performing a partial trace on the density matrix describing the complete state. Focusing to the case of bipartite systems (since it's most relevant to our work), the partial trace Tr_B maps the complete density matrix ρ_{AB} on the space $\mathcal{H}_A \otimes \mathcal{H}_B$ onto the density matrix ρ_A on $\mathcal{H}_A$. If $\{|a_i\rangle\}$ and $\{|b_i\rangle\}$ are a basis of $\mathcal{H}_A$ and $\mathcal{H}_B$, respectively, any density matrix ρ_{AB} can be decomposed as $\rho_{AB} = \sum_{ijkl} c_{ijkl} |a_i\rangle \langle a_j| \otimes |b_k\rangle \langle b_l|$. Using this decomposition, one can see that the partial trace can be obtained as

$$\text{Tr}_B(\rho_{AB}) = \sum_{ijkl} c_{ijkl} \langle b_l|b_k\rangle |a_i\rangle \langle a_j| . \tag{1.23}$$

Clearly, one can define the partial trace Tr_A over subsystem A in a similar way, and the result will be the density matrix ρ_B on $\mathcal{H}_B$.

1.3 Entanglement

Entanglement has been defined as the "*the* characteristic trait of quantum mechanics" [3], and is considered to be the most nonclassical manifestation of the quantum formalism. Its characterization and quantification have been the subject of deep interest ever since it was discovered, and its usefulness as a resource for quantum computation and information is no longer in question [4]. The topic of characterizing and quantifying entanglement is very vast and complex, and gets even more so as the dimensionality of the system increases. Here we provide the reader with a brief introduction on how entanglement can be quantified in two-qubit systems, since in this work we will only consider this kind of states, with the exception of Chapter 3, where we will briefly discuss three-qubit states.

A bipartite pure quantum state is said to be separable iff it can be written as

$$|\psi\rangle = |\phi_A\rangle \otimes |\phi_B\rangle , \tag{1.24}$$

where $|\phi_{A,B}\rangle$ are single-particle states. The same concept can be extended to non-pure states, where using the formalism of density matrices a separable state can be written as [5]

$$\rho_s = \sum_{i=1}^{k} p_i \rho_i^A \otimes \rho_i^B , \tag{1.25}$$

for some probabilities p_i and corresponding density matrices ρ_i^A, ρ_i^B. States that are not separable are said to be entangled, and *are the ones that cannot be simulated by classical correlations* [6].

For bipartite two-level systems, one can introduce the four maximally entangled Bell states

$$|\Psi^{\pm}\rangle = \frac{1}{\sqrt{2}}(|01\rangle \pm |10\rangle), \qquad |\Phi^{\pm}\rangle = \frac{1}{\sqrt{2}}(|00\rangle \pm |11\rangle), \tag{1.26}$$

which are also often referred to as EPR states and constitute a basis to span the Hilbert space of two qubits $\mathcal{H} = \mathcal{H}_1 \otimes \mathcal{H}_2$, with $\dim \mathcal{H}_1 = \dim \mathcal{H}_2 = 2$. Notice that none of these four states can be decomposed into a separable state of the form (1.24), meaning that they are entangled. Whenever a measure is performed only at one subsystem, the latter will be found with equal probabilities in the state $|0\rangle$ or $|1\rangle$. However, the outcomes of the measurements on both subsystems are perfectly correlated: we know nothing about the two subsystems alone, but we can have perfect knowledge of the system as a whole.

In general, telling whether a mixed state is entangled or not can be really complicated, and it has been shown to be an NP-hard problem [7] to solve. Many entanglement criteria exist, but they are necessary and sufficient only for some special cases.

A well known necessary criterion is the positive partial transpose (PPT) one, which for two-qubit mixed states also becomes sufficient. This criterion states that if ρ is separable, then the new matrix ρ^{Γ} with matrix elements defined in some fixed product basis as

$$\langle m| \langle \mu| \rho^{\Gamma} |n\rangle |\nu\rangle = \langle m| \langle \nu| \rho |n\rangle |\mu\rangle$$

is a density operator (i.e. has non-negative spectrum). If ρ on the other hand is entangled, ρ^{Γ} is not a valid state anymore. Notice that if the two-photon state is represented in a block form

$$\rho = \begin{pmatrix} A_{00} & A_{01} \\ A_{10} & A_{11} \end{pmatrix}, \tag{1.27}$$

then ρ^{Γ} can be expressed has

$$\rho^{\Gamma} = \begin{pmatrix} A_{00}^T & A_{01}^T \\ A_{10}^T & A_{11}^T \end{pmatrix}. \tag{1.28}$$

This criterion allows one to tell if a state is entangled or not, but tells nothing about the degree of entanglement of said state. Luckily, *entanglement measures* exist, which assign a numerical value to a state based on some properties. Many definitions for entanglement measures are present in the literature. Following [8], we call a map E an entanglement measure if it fulfills the following properties:

1. If ρ is separable, then $E(\rho) = 0$.

2. It should be invariant under local changes of basis.

3. It should not increase under any local operation assisted by classical communication (LOCC).

4. It should be convex, that is $E(\sum_i p_i \rho_i) \leq \sum_i p_i E(\rho_i)$.

5. It should be extensive, meaning that $E(\rho^{\otimes n}) = nE(\rho)$.

6. It should be subadditive, that is $E(\rho \otimes \sigma) \leq E(\rho) + E(\sigma)$.

The maps that only satisfy properties 2 and 3 are referred to as *entanglement monotones* [9].

A very common entanglement measure for two qubit states, and the one that we will employ in the rest of this work, is concurrence [10, 11]. For a pure state $|\psi\rangle$, concurrence C can be expressed as [4]

$$C = \langle \psi | \theta | \psi \rangle, \tag{1.29}$$

where θ is the antiunitary transformation $\theta\psi = \sigma_y \otimes \sigma_y \psi^*$, with * denoting the complex conjugation. As it's common to basically any entanglement measure, its generalization to mixed states requires a convex roof construction

$$C(\rho) = \min_{\rho = \sum_i p_i |\psi_i\rangle\langle\psi_i|} \sum_i p_i C(|\psi_i\rangle), \tag{1.30}$$

where the minimization is taken over all pure states decomposition of ρ. Nonetheless, in the case of two-qubits a closed form also exists for mixed states. Defining $\tilde{\rho} = \theta\rho\theta$ we can consider the operator

$$\omega = \sqrt{\rho}\sqrt{\tilde{\rho}}. \tag{1.31}$$

If we call $\lambda_1, \ldots, \lambda_4$ its singular values in decreasing order, concurrence can explicitly be expressed as

$$C(\rho) = \max\{0, \lambda_1 - \lambda_2 - \lambda_3 - \lambda_4\}. \tag{1.32}$$

The concurrence of a state ranges between 0 for separable states and 1 for fully entangled ones. Clearly, all four Bell states introduced earlier have $C = 1$.

1.4 Quantum Information Theory

In recent years, an information theory for quantum physics has been developed that could reproduce the role played in classical physics by Shannon information theory [12]. The latter associates the amount of information with the randomness that is shared by two parties. Clearly, the first problem that one encounters in a transition towards quantum information theory is that it has to deal with qubits (instead of classical bits) which obey laws that

are quite different. The main difference lies in the fact that qubits can exist in coherent superpositions, and quantum information theory thus has to be built on a mathematical construction that accounts for the relative phases in said superpositions. This is why the role of classical variables is replaced by the density matrix.

In classical information theory the Shannon entropy of an alphabet x_i, where the probability of each symbol is given by $p(x_i) = p_i$, is defined as [12]

$$H(p) = -\sum_i p_i \log_2 (p_i). \tag{1.33}$$

From now on we will assume the base of the logarithm to be two and we will omit the subscript.

In quantum information theory a quantity that is analogous to the Shannon entropy exists, namely the von Neumann Entropy, defined for a density matrix ρ as [13]

$$S(\rho) = -\operatorname{Tr}\left[\rho \log(\rho)\right] = -\sum_i \lambda_i \log(\lambda_i), \tag{1.34}$$

where λ_i are the eigenvalues of the density matrix and the second equality holds because ρ and $\log(\rho)$ are diagonal in the same basis. So, basically, the von Neumann entropy corresponds to the Shannon entropy of the eigenvalues of ρ and is related to the "mixedness" of a state: if $S(\rho) = 0$, then the state is pure; if $S(\rho) = \log(n)$ then the state is maximally mixed. All the off-diagonal terms in a density matrix reflect the relative quantum phases in superpositions (and that's why they are often referred to as "coherence" terms).

When ρ describes a pure state, the von Neumann entropy of the reduced density matrices are related to its entanglement. Entangled states are in fact the only ones for which the von Neumann entropy of the reduced density matrix can be higher than that of the whole state, meaning that a single subsystem is more disordered that the complete state (which is something that can never happen in classical information theory). For example, the four Bell states all have $S(\rho) = 0$, since they are pure states; their marginal states of either subsystem A or B on the other hand are given by $\rho_A = \rho_B = \mathbb{I}/2$, meaning that their von Neumann entropy is maximum.

Closely related to the von Neumann entropy are two other quantities: the conditional entropy $S(A|B)$ and the quantum mutual information $I(A:B)$. The former is the quantum equivalent of the conditional entropy in classical information, and for bipartite systems is defined as

$$S(A|B) = S(AB) - S(B), \tag{1.35}$$

where AB stands for the complete system described by the density matrix ρ_{AB}, and B is
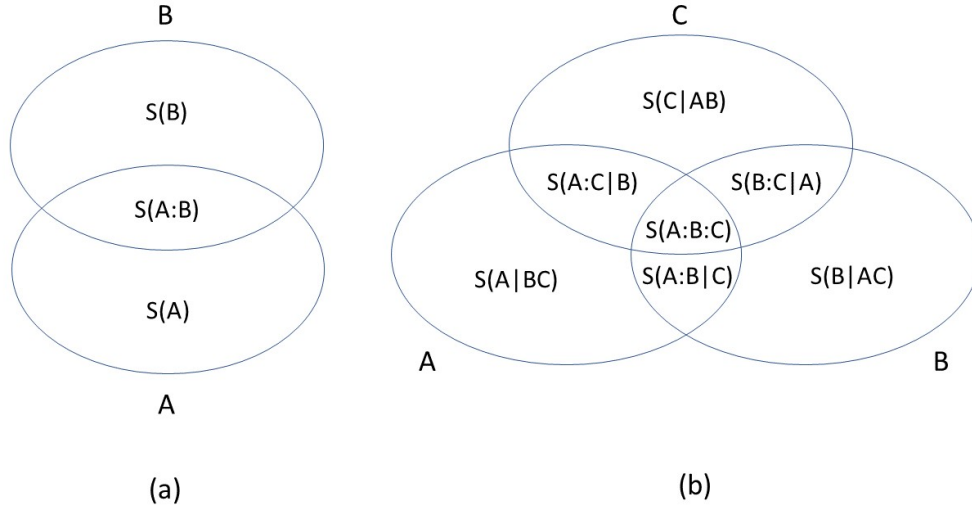
Figure 1.2: Entropic Venn diagrams for a quantum bipartite system AB (a) and a tripartite system ABC (b). All the entries of these diagrams are von Neumann entropies. Intersections between different sets contain the quantum mutual information shared among those parties.

the subsystem described by ρ_B obtained after tracing over subsystem A. Notice that from now on we will use the notation $S(AB) = S(\rho_{AB})$ (and similarly for the reduced partial matrices). Equation (1.35) implies that the conditional entropy can be negative, which happens whenever the entropy of the subsystem B is larger than that of the whole system AB. Again, this can only happen if the initial state is entangled.

The second quantity of interest is the quantum mutual information $I(A:B)$, defined as

$$I(A:B) = S(A) - S(A|B), \tag{1.36}$$

which quantifies the total correlations that can be shared between the parties A and B – both the classical and the quantum ones. It can also be written as

$$I(A:B) = S(A) + S(B) - S(AB), \tag{1.37}$$

from which it becomes evident that, in the case of two-qubit systems, $I(A:B)$ can be greater than unity. This behavior is only possible if the state is entangled, but, in general, the quantum mutual information does not separate correlation and entanglement (which is why it can't be used as an entanglement measure).

A very useful way of visualizing how different parts of a system are correlated among each other was introduced in [13], and has more recently been used to describe specific phenomena

such as the quantum erasure process [14]. This method consists in building entropic Venn diagrams, that is Venn-like diagrams where each set represents a subpart of the whole system and all the entries are entropies. Two examples of such diagrams are presented in Fig 1.2: in (a) the complete system is made of two parts, while in (b) a tri-partite system is depicted.

From Fig. 1.2(a) one can clearly recognize the relations in Eqs. (1.35) and (1.36). In particular, the intersection between two sets gives the quantum mutual information shared between those parties. If A and B are completely uncorrelated, the corresponding entropies in the diagram would be (1,0,1), and if they are classically correlated it would become (0,1,0). If they are perfectly entangled, on the other hand, one would obtain a non-classical diagram given by (-1,2,-1), which is the case, for example, of the four maximally entangled Bell states.

When a system is comprised of three parts a similar diagram can be built, as shown in Fig. 1.2(b). The conditional entropies $S(A|BC)$, $S(B|AC)$ and $S(C|AB)$ are simply generalizations of the conditional entropies in bipartite systems, so that for example one has

$$S(A|BC) = S(ABC) - S(BC), \tag{1.38}$$

and analogous relations for the other cases. The other quantities can be evaluated according to

$$S(A:B|C) = S(A|C) - S(A|BC) = S(AC) + S(BC) - S(C) - S(ABC), \tag{1.39}$$

and the ternary mutual information

$$S(A:B:C) = S(A) + S(B) + S(C) - S(AC) - S(AB) - S(BC) + S(ABC). \tag{1.40}$$

Using these relations all the entries of a tripartite system's diagram can be evaluated starting from the complete density matrix or from the partial ones. In Chapter 3 we will speak in more detail about these diagram as we study their application in a scenario of practical interest.

1.5 Quantum channels

Once a state is generated, it usually evolves and undergoes transformations, which are often represented by linear maps called *quantum channels*.

A quantum channel $M(\rho)$ maps a density operator into another density operator, and thus needs to satisfy the following properties [15]:

1. *Linearity*: $M(\alpha\rho_1 + \beta\rho_2) = \alpha M(\rho_1) + \beta M(\rho_2)$.

2. *Preserves Hermiticity*: if $\rho = \rho^\dagger$ then $M(\rho) = M(\rho)^\dagger$.

3. *Preserves positivity*: if $\rho \geq 0$ then $M(\rho) \geq 0$

4. *Preserves trace*: $\text{Tr}\left(M(\rho)\right) = \text{Tr}\left(\rho\right)$.

Quantum channels can be represented in many ways. A very useful representation is the so-called *operator-sum representation*. Basically, the initial state ρ is subjected to the linear map $M(\rho)$ that transforms it according to [15, 16]

$$M(\rho) = \sum_a K_a \rho K_a^\dagger, \tag{1.41}$$

where the operators K_a are called the Kraus operators (or operation elements) and obey the completeness relation

$$\sum_a K_a^\dagger K_a = I. \tag{1.42}$$

Also, the Kraus operators can always be chosen to be orthogonal, that is, $\text{Tr}\left(K_i^\dagger K_j\right) \propto \delta_{ij}$, where δ_{ij} represents the Kronecker delta function.

The word "channel" is clearly taken from the communication jargon: the initial state ρ is transmitted by the sender through a communication link, and the other party receives the state that has evolved according to Eq. (1.41).

The importance of quantum channels lies in the fact that they provide a formalism to treat the decoherence of a state, namely the process according to which a pure state evolves to become a mixed one. Suppose that an initial system A is in a pure state, and is combined in a separable state with a second system B. One can always think that the operator-sum representation in Eq. (1.41) arises from a unitary transformation U_{AB} that, acting on both systems, entangles A with B, followed by a partial trace performed on B that causes the state of A to become mixed. A unitary evolution of A is a special case where the operator sum only has one term. A very important consequence of this latter statement is that only unitary quantum channels can be inverted, which means that decoherence is irreversible: when system A becomes entangled with system B, we can't revert the damage unless we have access to B. Usually the system B represents the environment, namely everything over which we don't have control: decoherence thus causes quantum information to leak to the environment.

CHAPTER 2

Polarization-Mode Dispersion and Polarization-Dependent Loss

In this chapter we introduce the fundamentals of the main polarization effects that are present in fiber-optic-based communication networks, namely *polarization-mode dispersion* (PMD) and *polarization-dependent loss* (PDL). The physical mechanisms behind these phenomena are explained, and a thorough description of how they affect the propagation of a pulse is presented. We introduce the reader to the main parameters that characterize the two effects, which are of great importance in the comprehension of the results presented in the subsequent chapters. Notice that, even if the description that we provide here is purely classical, the formalism that we use (which is the same as the one in [17]) is completely analogous to the quantum description of states that we gave in Chapter 1. All the sections in this chapter represent a review of existing literature.

2.1   Polarization-mode dispersion

Polarization-mode dispersion originates from the presence of optical birefringence in fibers [17–19]. Due to the manifacturing process, in fact, the presence of asymmetries and imperfections is inevitable: these perturbations usually lead to the rise of linear birefringence [20]. One has to notice that even the so-called *single-mode fibers* support two modes of propagation, which are distinguished by their polarization. When an optical pulse propagates along a fiber, birefringence causes the two modes to travel with different group velocities, and the random nature of the change in birefringence results in a random coupling between them. The most immediate consequences of PMD in an optical channel are pulse distortion and system impairments, which may limit the transmission rate, in the absence of mitigation [21].

2.1.1 Birefringence and polarization-mode coupling

In a short section of fiber, one can usually assume the birefringence to be uniform. The electric field vectors of the slow (s) and fast (f) modes are aligned with with the axes of the fiber, and the difference between the respective propagation constants can be written as

$$\Delta\beta = \beta_s - \beta_f = \frac{\omega n_s}{c} - \frac{\omega n_f}{c} = \frac{\omega \Delta n}{c}, \tag{2.1}$$

where c is the speed of light in the vacuum, $\Delta n = n_s - n_f$ is the differential effective refractive index between the slow and the fast modes, and ω is is the angular optical frequency.

The differential refractive index allows to define the beat length $L_b = \lambda/\Delta n$, where $\lambda = 2\pi c/\omega$ is the wavelength. The beat length represents the distance for which a 2π phase difference accumulates between the two modes (meaning that the polarization has rotated through a full cycle).

Since the two modes travel along the fiber with different group velocity, they will be detected at distinct times; the time difference between the two modes is usually referred to as *differential group delay* (DGD), $\Delta\tau$, and can be found from the frequency derivative of the difference in propagation constants according to

$$\Delta\tau = L\frac{d}{d\omega}\left(\frac{\Delta n \omega}{c}\right) = L\left(\frac{\Delta n}{c} + \frac{\omega}{c}\frac{d\Delta n}{d\omega}\right), \tag{2.2}$$

where L represents the length of a short piece of fiber.

Because of the presence of this group delay, the resulting pulse at the output of the birefringent fiber can be heavily distorted. In this very simple scenario that we just described, the states of polarization of the birefringence are the fiber eigenstates, as they do not change with the propagation distance, and are not affected by pulse distortion.

The situation described above, while potentially detrimental for optical communication systems, could be easily addressed: for example, one could just launch the signal into one of the eigenmodes, so that it wouldn't be distorted with propagation. The problem with real telecommunication fibers is that they can be hundreds or even thousands of kilometers long, and the issues one has to face are much more complex. In these scenarios in fact, the presence of local stress, curvature and geometrical imperfections induces continuous changes in the birefringence, both in terms of eigenpolarizations and difference between effective indices. Usually, this complex phenomenon is modeled through a concatenation of very short fibers, each characterized by a constant birefringence, such that the birefringence axes and the propagation constants change randomly along the whole fiber. As shown in Fig. 2.2, the output pulse is the result of many splits that happen within each section, and its distortion can be very complicated. Clearly, from the random nature of the phenomena underlying
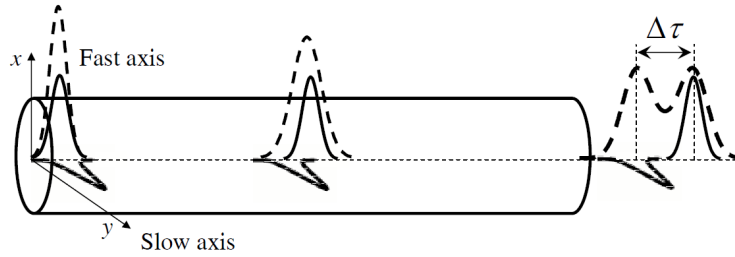
Figure 2.1: Effect of birefringence (or, analogously, of PMD in a short piece of fiber) in the time domain. The input pulse is split into two pulses that propagate with different group velocities and accumulate a time difference $\Delta\tau$.
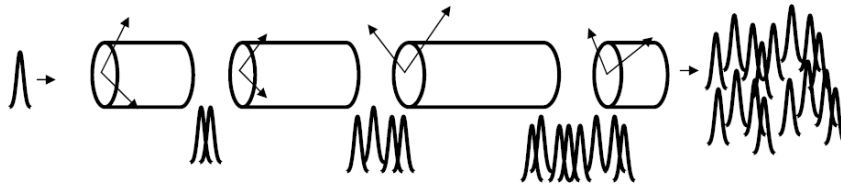

Figure 2.2: A long fiber can be modeled as a concatenation of many birefringent elements. Each element splits the incoming pulse into two replicas, and the parameters characterizing each element are random, so that the output pulse is distorted in a very complex way.

birefringence, a statistical approach is the best way to characterize how different polarization modes are coupled in fibers [22, 23].

Luckily, if the signal bandwidth is narrow enough, the distortion that it experiences is equivalent to the one caused by constant birefringence, and a simpler description exists. Basically, one replaces the link with a fiber of constant birefringence with some well defined delay and eigenpolarizations that would distort the signal in an equivalent manner; this description is usually referred to as *first-order* PMD approximation [24], and we will assume that it holds for the rest of this work.

2.1.2   PMD parameters

In this section we will make use of the notation introduced in [17], which has the quality of being easily translated into the quantum formalism. It is well known that propagation in a lossless birefringent medium (like a fiber) can be described in the Jones representation as a 2×2 complex matrix that includes the frequency dependency in it [25]. This matrix relates

the input state of polarization $|s\rangle$ to the output $|t\rangle$ according to

$$|t\rangle = \mathbf{T}(\omega)\,|s\rangle = e^{i\phi_0(\omega)}\mathbf{U}(\omega)\,|s\rangle, \tag{2.3}$$

where ϕ_0 is a phase term of the transmission matrix $\mathbf{T}(\omega)$, and both $\mathbf{T}(\omega)$ and $\mathbf{U}(\omega)$ are unitary matrices to account for the absence of loss, that is

$$\mathbf{T}^\dagger(\omega)\mathbf{T}(\omega) = \mathbf{U}^\dagger(\omega)\mathbf{U}(\omega) = \mathbb{I}. \tag{2.4}$$

The operator $\mathbf{U}(\omega)$ will then have orthogonal and unit magnitude eigenvalues, meaning that it can be expanded as

$$\mathbf{U} = e^{-i\varphi/2}\,|r\rangle\,\langle r| + e^{i\varphi/2}\,|r_-\rangle\,\langle r_-|, \tag{2.5}$$

where $|r\rangle$ and $|r_-\rangle$ are its eigenvectors with corresponding eigenvalues $e^{\pm i\varphi}$. By making use of Eq. (1.20) with r replacing n, the operator U can be written as

$$\mathbf{U} = \mathbb{I}\cos\left(\varphi/2\right) - i\,(\hat{r}\cdot\vec{\sigma})\sin\left(\varphi/2\right), \tag{2.6}$$

or, in a more concise fashion as

$$\mathbf{U} = e^{-i(\varphi/2)\hat{r}\cdot\vec{\sigma}}. \tag{2.7}$$

Analogous relations can clearly be found for another well known representation, namely the Stokes representation. In Stokes space, the polarization state is described as a real-valued 3-D vector (in an analogous manner as is done for qubits in Bloch space), and the output state of polarization is related to the input one by

$$\hat{t} = \mathbf{R}(\omega)\hat{s} \tag{2.8}$$

where $\mathbf{R}$ is a 3×3 unitary matrix, which is isomorphic to the Jones matrix $\mathbf{U}$. In Stokes space, lossless propagation is thus represented as a rotation on the Poincarè/Bloch sphere. The relation between $\mathbf{R}$ and $\mathbf{U}$ is given by

$$\mathbf{R}\vec{\sigma} = \mathbf{U}^\dagger\vec{\sigma}\mathbf{U}. \tag{2.9}$$

From the combination of Eqs. (2.6) and (2.9) one gets an explicit rotational form for $\mathbf{R}$:

$$\mathbf{R} = \mathbb{I} + \sin\left(\varphi\right)\hat{r}\times[1 - \cos\left(\varphi\right)](\hat{r}\times)(\hat{r}\times), \tag{2.10}$$

with the crossproduct operator $\hat{r}\times$ being defined as

$$\hat{r}\times = \begin{pmatrix} 0 & -r_3 & r_2 \\ r_3 & 0 & -r_1 \\ -r_2 & r_1 & 0 \end{pmatrix}. \tag{2.11}$$

From Eq. (2.10), it is clear that for any Stokes vector $\hat{s}$, $\mathbf{R}\hat{s}$ represents a right-handed rotation of $\hat{s}$ through an angle φ about the direction $\hat{r}$ [17].

A surprising aspect of PMD is that, as noted by Poole *et al.* in [26], regardless of how long a fiber is, one can always find two polarization states (that, in the absence of polarization-dependent loss are orthogonal) with the peculiar property that a light pulse launched in one of these two polarization states results in an output pulse whose polarization does not change to first order in frequency. These are the so-called *principal states of polarization* (PSP), and light polarized along these axes has the minimum and maximum group delays – which is why one usually refers to them as *fast* and *slow* PSP, respectively. The difference between these two delays is called *differential group delay* (DGD), and its typical mean values can range from 1 to 50 ps for fibers that are few hundreds of kilometers long. The DGD and the PSP allow one to define a very important quantity, which in the first order picture completely characterizes the PMD of a fiber, namely the PMD vector $\vec{\tau}$, whose magnitude is equal to the DGD τ and whose direction is that of the slow PSP $\hat{p}$ [1], such that

$$\vec{\tau} = \tau\hat{p}. \tag{2.12}$$

The PMD vector can easily be derived starting from Eq. (2.3). If we make the assumption that the polarization of the input pulse is frequency-independent, that is, $|s\rangle_\omega = 0$ [2] (meaning that $\hat{s}_\omega = 0$), from Eq. (2.3) one obtains for the output

$$|t\rangle_\omega = -i(d\phi_0/d\omega + i\mathbf{U}_\omega\mathbf{U}^\dagger)|t\rangle. \tag{2.13}$$

Thus for most input polarizations, the output polarization will change with frequency to first order, and the frequency derivative of the phase term ϕ_0 allows one to define a group delay τ_0 that is common to all polarizations $\tau_0 = d\phi_0/d\omega$. Nonetheless, as noted in [26], if $|t\rangle$ is either one of the two eigenstates of the operator $i\mathbf{U}_\omega\mathbf{U}^\dagger$, then $\hat{t}_\omega = 0$, and $|t\rangle_\omega$ can be

---

[1]In the original notation of Poole *et al.* the PMD vector is aligned along the *fast* axis, instead. We follow the notation introduced by Gordon in [17], where the PMD vector is defined for a right-circular Stokes space.

[2]Consistently with the notation used in [17], for the rest of this work we will often denote differentiation with respect to frequency with a subscript ω - i.e., $d|s\rangle/d\omega = |s\rangle_\omega$

written in the form

$$|t\rangle_\omega = -i(d\phi/d\omega)|t\rangle, \tag{2.14}$$

where ϕ identifies with the phase of $|t\rangle$, such that the term $d\phi/d\omega$ represents a group delay τ_g. Since $\mathbf{U}$ is a unitary operator, one can show that the operator $i\mathbf{U}_\omega\mathbf{U}^\dagger$ is unitary, too, and it also has zero trace. This means that its eigenvalues are real and add up to zero, and we will call them $\tau/2$ and $-\tau/2$. Comparing Eqs. (2.13) and (2.14), and using the definitions of τ_0 and τ_g thus leads to

$$\tau_g = \tau_0 \pm \tau/2. \tag{2.15}$$

If we designate the eigenstate of $i\mathbf{U}_\omega\mathbf{U}^\dagger$ corresponding to the largest eigenvalue (that is, the highest group delay) with $|p\rangle$, so that the orthogonal eigenstate having the smaller eigenvalue becomes $|p'\rangle$, we have recovered the slow and fast axes corresponding to the PSP. We remind the reader that these Jones vectors are associated to Stokes vectors; since they are orthogonal in Jones space, they will be counter-aligned in Stokes space, such that $|p\rangle$ corresponds to $\hat{p}$ and $|p'\rangle$ to $-\hat{p}$.

The slow PSP $|p\rangle$ satisfies the Jones matrix eigenvector equation

$$\frac{1}{2}\tau|p\rangle = i\mathbf{U}_\omega\mathbf{U}^\dagger|p\rangle, \tag{2.16}$$

and according to Eq. (2.15), the DGD is given by τ. An expression for τ can be obtained as

$$\tau = 2\sqrt{\det\mathbf{U}_\omega}. \tag{2.17}$$

So, in conclusion, the PMD vector $\vec{\tau}$ is the Stokes vector of $|p\rangle$ multiplied by the DGD, as previously stated in Eq. (2.12). A very useful expansion for the operator $i\mathbf{U}_\omega\mathbf{U}^\dagger$ exixts in terms of the components of the PMD vector, namely

$$i\mathbf{U}_\omega\mathbf{U}^\dagger = \frac{1}{2}\vec{\tau}\cdot\vec{\sigma} = \frac{1}{2}\tau\hat{\tau}\cdot\vec{\sigma}. \tag{2.18}$$

2.1.3 The dynamical PMD equation

Until now, we've studied how the polarization of light evolves along the fiber in the Jones domain. Clearly, one could do the same in the Stokes space as well, and this leads to an equation describing the evolution PMD vector along the fiber.

The PMD vector directly affects how the polarization state changes with frequency. This can be seen by noticing that an analogous equation to Eq. (1.21) exists that relates a Stokes vector $\hat{t}$ to its Jones counterpart $|t\rangle$, namely

$$\hat{t} = \langle t | \vec{\sigma} | t \rangle. \tag{2.19}$$

Combined with Eq. (2.8), the latter leads to an expression for the frequency derivative of the polarization state:

$$\frac{\partial \hat{t}}{\partial \omega} = 2\text{Re}\{\langle t | \vec{\sigma} \mathbf{T}_\omega \mathbf{T}^\dagger | t \rangle\}. \tag{2.20}$$

Now, using Eq. (2.18) allows to express $\mathbf{T}_\omega \mathbf{T}^\dagger$ as

$$\mathbf{T}_\omega \mathbf{T}^\dagger = i\tau_0 \mathbb{I} + \mathbf{U}_\omega \mathbf{U}^\dagger = i\left(\tau_0 \mathbb{I} - \frac{\vec{\tau} \cdot \vec{\sigma}}{2}\right), \tag{2.21}$$

which, combined with the properties of the Pauli matrices [17] $\vec{\sigma}(\vec{a} \cdot \sigma) = \vec{a}\mathbf{I} + i\vec{a} \times \vec{\sigma}$ and $\langle t | \vec{a} \times \vec{\sigma} | t \rangle = \vec{a} \times \hat{t}$, leads to

$$\frac{\partial \hat{t}}{\partial \omega} = \vec{\tau} \times \hat{t}. \tag{2.22}$$

This equation shows how the variation with frequency of the output polarization state is governed by the PMD vector, and its geometrical interpretation is shown in Fig. 2.3: when the PMD vector is frequency-independent (meaning that the first-order approximation is valid) the output state of polarization rotates around the PMD vector as the frequency changes, the rotation rate being determined by the magnitude of $\vec{\tau}$, which coincides with the DGD. This situation is shown in panel (a) of Fig. 2.3. If, on the other hand, the PMD vector does depend on frequency, then the state of polarization follows a complicated path on the Poincaré/Bloch sphere as ω varies, since the axis of rotation instantaneously changes. This behavior is depicted in Fig. 2.3(b).

The same rotation can be expressed in terms of Muller matrices. Differentiating Eq. (2.8) with respect to angular frequency ω leads in fact to

$$\frac{\partial \hat{t}}{\partial \omega} = \mathbf{R}_\omega \hat{s} = \mathbf{R}_\omega \mathbf{R}^\dagger \hat{t}, \tag{2.23}$$

which combined with Eq. (2.22) gives

$$\vec{\tau} \times = \mathbf{R}_\omega \mathbf{R}^\dagger, \tag{2.24}$$

that is the Stokes-space equivalent of Eq. (2.18).

We have discussed how the PMD vector determines the frequency dependence of the polarization state at the output of the fiber. We now want to investigate how the state of polarization evolves along the fiber, at a generic distance z from the transmitting station. Clearly, the transmission matrix $\mathbf{T}$ and the output state of polarization will have to reflect this dependence on the distance, so that the output state can be expressed as a function of
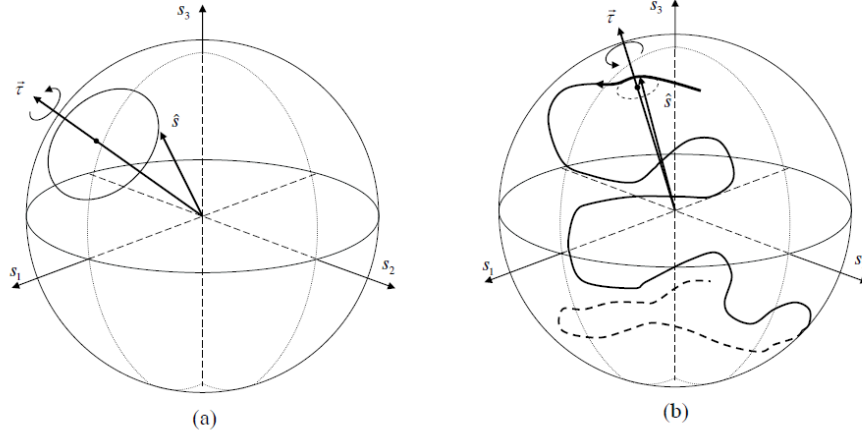
Figure 2.3: (a) When the PMD vector is frequency-independent (meaning that the first-order approximation is valid) the effect of PMD in the frequency domain can be seen as a frequency-dependent rotation around the PMD vector. (b) If the PMD vector depends on frequency, then the output polarization state follows a complicated trajectory as the frequency changes.

the input as

$$|t(z)\rangle = \mathbf{T}(z, \omega) |s\rangle. \tag{2.25}$$

An expression for the matrix $i\mathbf{T}_z\mathbf{T}^\dagger$ can be found to be

$$i\mathbf{T}_z\mathbf{T}^\dagger = i\left(\beta_0\mathbb{I} - \frac{\vec{\beta}\cdot\vec{\sigma}}{2}\right), \tag{2.26}$$

where $\beta_0 = \partial\phi_0/\partial z$ and the three-dimensional vector $\vec{\beta}(z)$ represents the local birefringence vector.

Similarly to how Eq. (2.22) was obtained, one can derive the equation governing the spatial evolution of the state of polarization, namely

$$\frac{\partial\hat{t}}{\partial z} = \vec{\beta} \times \hat{t}. \tag{2.27}$$

From the combination of the two main equations obtained in this Section, namely Eqs. (2.22) and (2.27), one can obtain the *dynamical PMD equation* [27]

$$\frac{\partial\vec{\tau}}{\partial z} = \frac{\partial\vec{\beta}}{\partial\omega} + \vec{\beta} \times \vec{\tau}. \tag{2.28}$$

The local birefringence vector thus determines the evolution of the PMD vector along the fiber.

Even though the topic won't be covered in this work, it is important to stress that the statistical description of PMD is based on the dynamical PMD equation, and can be developed once a statistical model for the birefringence vector is assumed [28]. This description allows one to obtain, for example, one of the best known results about PMD, namely that the mean DGD increases with the squared root of the fiber length [22], as is characteristic of a random-walk problem. This is particularly relevant since, as discussed in [29], virtually every general statistical property of PMD in long fibers is uniquely determined by the mean DGD. As an example, the autocorrelation bandwidth of the PMD vector is shown in [29] to be equal to $0.25/\sqrt{\langle\tau\rangle}$, where $\langle\tau\rangle$ is the mean DGD (the result is expressed in the units of natural frequency). This quantifies the range over which the PMD vector can be assumed to be almost constant – or, equivalently, over which the first-order approximation can be employed.

2.2 Polarization-dependent loss

We've discussed how the presence of PMD in fibers affects the state of polarization of the propagating pulse. A second effect that is ever-present in fiber-optic networks is polarization-dependent loss (PDL), which mostly arises from the presence of the optical components (such as polarization controllers, adapters, connectors, etc.) along the route.

Polarization-dependent loss refers to the energy loss that depends on the polarization state of the pulse [30]. We've already shown how, in the Jones picture, a generic polarization state can be expressed in a certain basis with a two-component vector; the action of PDL can be visualized as an attenuation that affects one of the two axes more than the other, and can thus be seen as a partial polarizer (on the contrary, we've seen how PMD tends to de-polarize by creating frequency dispersion of polarization).

Typically, PDL is quantified as [30]

$$\mathrm{PDL_{dB}} = 10\log\left(\frac{T_{\max}}{T_{\min}}\right), \tag{2.29}$$

where $T_{\max}$ and $T_{\min}$ are the maximum and minimum transmission intensities. The maximum transmission intensity clearly occurs when the polarization state of the light beam is aligned with the maximum transmission axis of the PDL element, and the minimum for the one that is orthogonal on the Poincaré sphere.

If we consider a very simple example of a PDL element aligned along the horizontal direction,

then the corresponding Jones matrix $\mathbf{P}$, such that the output vector $|t\rangle$ is related to the input $|s\rangle$ through

$$|t\rangle = \mathbf{P}|s\rangle, \tag{2.30}$$

can be written as

$$\mathbf{P} = \begin{pmatrix} 1 & 0 \\ 0 & e^{-\gamma} \end{pmatrix}, \tag{2.31}$$

where the loss coefficient γ is related to the PDL in dB as

$$\mathrm{PDL}_{\mathrm{dB}} = \gamma(20\log \mathrm{e}), \tag{2.32}$$

the coefficient 20 arising from the fact that PDL is defined as a ratio between intensities rather than the fields themselves. This relation is independent of the orientation of the PDL element; in general, in fact, the latter will not be aligned with the horizontal direction, but the resulting operator can always be written as $\mathbf{P}' = \mathbf{U}\mathbf{P}\mathbf{V}^{\dagger}$, where $\mathbf{U}$ and $\mathbf{V}$ are unitary operators. Using the exponential form (and dropping the apex), the generic PDL operator can be written as

$$\mathbf{P} = \mathrm{e}^{-\gamma/2}\exp\left(\frac{\vec{\gamma}\cdot\vec{\sigma}}{2}\right), \tag{2.33}$$

in which the local PDL vector $\vec{\gamma} = \gamma\hat{\gamma}$ was implicitly defined, with $\hat{\gamma}$ representing a unit-length vector in Stokes space aligned with the direction of maximum transmission. The exponential can be expanded as we did for the PMD operator leading to

$$\mathbf{P} = \mathrm{e}^{-\gamma/2}[\mathbb{I}\cosh(\gamma/2) + (\hat{\gamma}\cdot\vec{\sigma})\sinh(\gamma/2)]. \tag{2.34}$$

As it's evident from the definition of the corresponding operator, PDL is not unitary, meaning that the inner product will not be preserved during propagation. If the input-output relation is again given by Eq. (2.30) and we assume that the input vector has unit length such that $\langle s|s\rangle = 1$, then one has for the output state

$$\langle t|t\rangle = \langle s|\mathbf{P}^{\dagger}\mathbf{P}|s\rangle = e^{-\gamma}(\cosh\gamma + (\hat{\gamma}\cdot\hat{s})\sinh\gamma). \tag{2.35}$$

The quantity $\langle t|t\rangle$ is usually referred to as *transmission intensity* T_p, and clearly depends not only on the loss coefficient γ but also on the relative orientation of the incoming polarization state and the PDL vector γ. The maximum and minimum transmission intensities are thus given by

$$T_p = \begin{cases} 1 & \hat{\gamma}\cdot\hat{s} = 1 \\ \mathrm{e}^{-2\gamma} & \hat{\gamma}\cdot\hat{s} = -1, \end{cases} \tag{2.36}$$

from which PDL in dB can be calculated, and the result coincides with Eq. (2.32). It should be clear now, that if in the channel a cascade of two PDL elements is present, such that the resulting operator is given by $\mathbf{P}_{\text{tot}} = \mathbf{P}_2 \mathbf{P}_1$, the transmission coefficient in general will not be just the product of the individual ones, as a result of the relative orientations of the PDL vectors and the polarization state.

If the input state is completely depolarized, the transmission must be averaged over all polarization states. Unpolarized light can be considered as an equal mixture on any pair of orthogonal polarization states. In particular, one can pick the ones corresponding to the maximum and minimum transmission coefficients, and the transmission coefficient fo unpolarized light T_{depol} is simply the average of the two [31]

$$T_{\text{depol}} = \frac{T_{\text{max}} + T_{\text{min}}}{2} = \frac{1 + e^{-2\gamma}}{2}, \qquad (2.37)$$

where Eq. (2.36) was used. In [31] the parameter Γ was introduced to quantify the PDL as

$$\Gamma = \frac{T_{\text{max}} + T_{\text{min}}}{T_{\text{max}} - T_{\text{min}}} = \tanh \gamma, \qquad (2.38)$$

which is related to the transmission coefficient for unpolarized light by

$$T_{\text{depol}} = \frac{1}{1 + \Gamma}. \qquad (2.39)$$

Recalling that the PDL in dB is given by Eq. (2.29) allows one to formulate a relation between the two definitions as

$$\text{PDL}_{\text{dB}} = 10 \log \left(\frac{1 + \Gamma}{1 - \Gamma} \right). \qquad (2.40)$$

2.2.1 PDL and PMD

The description of PMD and PDL we've just introduced becomes considerably more involved when they coexist in an optical channel, and their combination creates effects that can't be explained by analyzing the two phenomena separately [32, 33]. For example, PDL is usually a frequency-independent effect, but the joint presence of PMD in the channel can give rise to frequency-dependent PDL [34]. This is due to the fact that PMD rotates the polarization state by an amount that depends on the frequency. Different frequency components will then result in different polarization states, whose relative alignment with the PDL vector will thus vary, resulting in a different attenuation. Another complication induced by the joint presence of PDL and PMD is that the overall DGD might be higher than the one induced by PMD alone [30], and the PSP usually end up not being orthogonal [33].

It should be clear, then, that in general the presence of PMD and PDL in a channel causes impairments and distortions whose characterization is more complex than for the ones caused by the two effects individually. The description of such a channel is also complicated by the fact that the two effects are usually distributed along the optical link. This is what lead us to try to develop a simple and intuitive model (that we introduce in Chapter IV) that could reproduce at least the most relevant features of a channel comprising both PMD and PDL, without needing to rely on the mathematical complexity of the complete formal description. Our model also has the advantage of being easy to reproduce in the laboratory with off-the shelf equipment, and gives a strong intuition to the physics of the two phenomena.

CHAPTER 3

PMD in a quantum channel

In this chapter we thoroughly investigate the effects of the presence of polarization-mode dispersion (PMD) in a quantum channel. The penalties introduced by the presence of PMD in channels used for classical communications are well known, and are mostly related to pulse distortion and limitations in the transmission rate that can be achieved. In the case of quantum states propagating in a fiber-based channel, on the other hand, polarization-mode dispersion represents the main source of decoherence, namely, the process that turns the initial pure state into a mixed one by entangling the state with the environment.

We will investigate the effect of PMD on polarization-entangled photons, referring to the scenario that is schematically depicted in Fig. 3.1: the two photons of an initial Bell state are propagated towards two users (usually called Alice and Bob) in channels affected by the presence of PMD, which clearly impacts the quality of the polarization entanglement. In light of what we discussed in Chapter 2, in fact, the main effect of PMD is that of coupling the time of arrival of a photon with its polarization, which corrupts the polarization entanglement of a photon pair, by introducing a certain degree of distinguishability – the higher the amount of PMD in the channel, the easier it will be to tell the photon polarization based on its time of arrival. We also develop a description of the effect of PMD on polarization-entangled photons in the framework of quantum information theory. The first section of this chapter presents a review of pre-existing results, while the following sections contain original work. Some of the results obtained are presented in paper C8.

3.1 Effect of PMD on a single photon

Suppose that a photon is propagating in a channel characterized by a PMD vector $\vec{\tau}$. The initial state can be described by

$$|\Psi\rangle = |f(t)\rangle \otimes |\psi_P\rangle , \qquad (3.1)$$

Figure 3.1: Schematic of the scenario of interest. A pulsed-pump source generates polarization-entangled photon pairs. The two photons of each pair are filtered apart and sent to remote users (Alice and Bob) via two fibers impaired by PMD.

where $|f(t)\rangle = \int f(t) |t\rangle \, dt$ accounts for the time-dependent part of the state and $|\psi_P\rangle$ accounts for the polarization part of the state, the latter being represented in the standard basis as

$$|\psi_P\rangle = \alpha |h\rangle + \beta |v\rangle, \tag{3.2}$$

with $\{\alpha, \beta\} \in \mathbb{C}$ and $|\alpha|^2 + |\beta|^2 = 1$. Before PMD is applied, the time-dependent and the polarization parts of the state are clearly separable, as its evident from Eq. (3.1).

To account for the effect of PMD, it is convenient to represent $|\psi_P\rangle$ in the PSP basis $\{|p\rangle, |p'\rangle\}$, that is

$$|\psi_P\rangle = a |p\rangle + b |p'\rangle, \tag{3.3}$$

with

$$a = \alpha \langle p|h\rangle + \beta \langle p|v\rangle, \quad b = \alpha \langle p'|h\rangle + \beta \langle p'|v\rangle. \tag{3.4}$$

As it was shown in Chapter 2, in the context of first-order approximation PMD can be fully described by the PMD vector $\vec{\tau}$; this means that we can represent its effect as a delay $\tau = |\vec{\tau}|$ between the two replicas that propagate along the slow and fast axis, respectively. The output state can thus be written as

$$|\Psi_{PMD}\rangle = a |p\rangle \otimes |f(t - \tau/2)\rangle + b |p'\rangle \otimes |f(t + \tau/2)\rangle. \tag{3.5}$$

The polarization density matrix of the received photon can be obtained by tracing over the time modes, to account for the fact that the detectors are insensitive of the photon's time of arrival; one then has

$$\rho = \int dt \, \langle t|\Psi_{\text{PMD}}\rangle \langle \Psi_{\text{PMD}}|t\rangle = \begin{pmatrix} |a|^2 & ab^* R(\tau) \\ a^*b R^*(\tau) & |b|^2 \end{pmatrix}, \tag{3.6}$$

where the function $R(\tau)$ is defined in the frequency domain as

$$R(\tau) = \int \frac{d\omega}{2\pi} |\tilde{f}(\omega)|^2 e^{i\tau\omega}, \tag{3.7}$$

with $\tilde{f}(\omega)$ representing the Fourier transform of $f(t)$. The function $R(\tau)$ is normalized such that $|R(0)|^2 = 1$, and describes the overlap integral between the original waveform and the delayed replica. From its definition, it is clear that one has $R(\tau)^* = R(-\tau)$. The orientation of the PMD vector does not affect the value of the function $R(\tau)$, which only depends on the DGD in the channel and on the bandwidth of the photon. Notice that once the time modes have been traced out of the complete density matrix, all the parameters that affect the time/frequency-dependent part of the state enter the received density matrix through this function. The density matrix in Eq. (3.7) is represented in the basis of the PSP; knowing how these are aligned with respect to the $\{h, v\}$ basis through the parameters a and b, allows one to apply the rotation needed to represent it in the standard basis.

Let's now consider two exemplary scenarios that show how the orientation of the PMD vector influences the received photon. If the PSP are aligned with the $\{h, v\}$ basis, then Eq. (3.7) is already expressed in the standard basis, and the density matrix becomes

$$\rho = \begin{pmatrix} |\alpha|^2 & \alpha\beta^* R(\tau) \\ \alpha^*\beta R^*(\tau) & |\beta|^2 \end{pmatrix} = (1-p)\rho_{\text{in}} + p\sigma_3\rho_{\text{in}}\sigma_3, \tag{3.8}$$

where $p = (1 - R(\tau))/2$ and $\rho_{\text{in}} = |\psi_P\rangle \langle\psi_P|$ is the polarization density matrix of the initial state. The effect of PMD in this case is that of a phase-flipping channel with probabilistic action on the qubit; the probability p that the error occurs increases with the amount of PMD in the channel.

A second interesting scenario is the one in which the PSP and the vectors of the standard basis are orthogonal on the Bloch sphere. In this case, it is easy to show (assuming, for example, to start with the $|h\rangle$ or $|v\rangle$ state), that the final density matrix can be written as

$$\rho = (1-p)\rho_{\text{in}} + p\sigma_1\rho_{\text{in}}\sigma_1, \tag{3.9}$$

where the qantity p is defines in the same way as before. The effect of orthogonal PMD is thus that of propagation through a probabilistic bit-flip channel; the rate at which the error introduced by channel occurs is again regulated by the amount of PMD.

3.2 Effect of PMD on polarization-entangled photons

Now that the effect of PMD on a single photon has been described, we can move on to studying the case of a polarization-entangled two-photon state. The reason why the presence of PMD in the channel of propagating photons can be detrimental to the degree of polarization entanglement arises from the fact that it couples the time of arrival of a photon to its polarization. Suppose that PMD is present only in one channel, say, that of Alice. One can expand the initial state of polarization of the photon in terms of the PSP of her fiber. After we let the two photons propagate, hers will be detected earlier or later than Bob's photon, depending on whether the initial polarization has collapsed on the fast or slow PSP. In practice, since the time-accuracy of most detectors is larger than the typical delays introduced by fibers, this information is lost to the environment, which leads to the decoherence of the state and to a reduction of its entanglement content [35].

We start by briefly describing the generated two-photon state, and we then move to a formal description of how PMD affects its quantum properties.

3.2.1 Generated two-photon state

A polarization-entangled two-photon state, which can be generated either via a χ^2 (such as parametric down conversion) or a χ^3 (such as four-wave mixing) process, can be written as

$$|\Psi\rangle = |\tilde{f}(\omega_A, \omega_B)\rangle \otimes \frac{|h_A, h_B\rangle + e^{i\alpha} |v_A, v_B\rangle}{\sqrt{2}}, \tag{3.10}$$

where h_i and v_i are orthogonal polarization basis states of photons A and B, and α is an arbitrary fixed phase factor, such that when $\alpha = 0$ a Φ^+ state is generated. The frequency-dependent part of the state is described by the ket $|\tilde{f}(\omega_A, \omega_B)\rangle$, which can be expressed as [36]

$$|\tilde{f}(\omega_A, \omega_B)\rangle = \int \int d\omega_A d\omega_B \tilde{f}(\omega_A, \omega_B) |\omega_A, \omega_B\rangle, \tag{3.11}$$

where the function $\tilde{f}(\omega_A, \omega_B)$ accounts for the shape and bandwidth of the pump and filters used in the generation of the entangled photons. It also depends on the nature of the process that is employed; in the case of parametric down conversion one has

$$\tilde{f}^{(2)}(\omega_A, \omega_B) = H_A(\omega_A) H_B(\omega_B) \tilde{E}_p(\omega_A + \omega_B). \tag{3.12}$$

Here, $\tilde{E}_p(\omega)$ denotes the Fourier transform of the pump waveform $E_p(t)$, and $H_A(\omega_A)$ and $H_B(\omega_B)$ denote the transfer functions of the filters applied to the two photons prior to transmission.

In the case of four-wave mixing we have

$$\tilde{f}^{(3)}(\omega_A, \omega_B) = H_A(\omega_A) H_B(\omega_B) \int d\omega' \tilde{E}_p(\omega') \tilde{E}_p(\omega_A + \omega_B - \omega'). \tag{3.13}$$

Notice that in the rest of this work we will assume that the photon pair is generated via four-wave mixing, so that we are consistent with the apparatus used in the experiments, and the frequency-dependent part of the initial two-photon state will thus always be described by Eq. (3.13).

Equation (3.11) can also be expressed in the time domain, which can be useful in certain circumstances, as

$$|f(t_A, t_B)\rangle = \int \int dt_A dt_B f(t_A, t_B) |t_A, t_B\rangle. \tag{3.14}$$

The function $f(t_A, t_B)$ is the inverse Fourier transform of $\tilde{f}(\omega_A, \omega_B)$, and its absolute value $|f(t_A, t_B)|^2$ is proportional to the probability that the two photons overlap in time; it is normalized such that $\int dt_A dt_B |f(t_A, t_B)|^2 = 1$.

3.2.2 Phase-matching function

In the previous section we assumed the phase-matching conditions to be satisfied within the bandwidth of the two filters (i.e. we assumed phase-matching function to be constant over the frequency range of interest). This might not always be the case, especially with an increasing pump bandwidth.
In order to include the effects of a non-uniform phase-matching function, we write down again the frequency (or time) dependent part of the state in the following way:

$$\tilde{f}(\omega_A, \omega_B) = H_A(\omega_A) H_B(\omega_B) \int d\omega' \tilde{E}_p(\omega') \tilde{E}_p(\omega_A + \omega_B - \omega') \Phi(\omega', \omega_A, \omega_B), \tag{3.15}$$

where the new term $\Phi(\omega)$ is the phase matching function which can be expressed as [36]

$$\Phi(\omega', \omega_A, \omega_B) = \int_0^L dz \exp(-i\Delta k z) = \mathrm{sinc}\left(\frac{\Delta k L}{2}\right) \exp\left(i\frac{\Delta k L}{2}\right), \tag{3.16}$$

with L being the length of the fiber in which the process takes place.
The term $\Delta k = k_{p1} + k_{p2} - k_s - k_i$ is the wave-vector mismatch, which can more explicitly be written as:

$$\Delta k = \frac{\omega'}{c} n(\omega') + \frac{\omega_A + \omega_B - \omega'}{c} n(\omega_A + \omega_B - \omega') - \frac{\omega_A}{c} n(\omega_A) - \frac{\omega_B}{c} n(\omega_B).$$

3.2.3 Effect of PMD

As we discussed earlier in this work, the effect of first-order PMD is easily described in the basis made of the PSP: when the incoming polarization corresponds to either one of the PSP, in fact, PMD advances or delays the time of arrival of the photon, depending on whether the initial state is aligned with the fast or slow PSP, respectively. Therefore, it is convenient to write the initial state in terms of the PSP basis $\{|p_i\rangle, |p_i'\rangle\}$, as we did for the case of a single photon, with the difference that we now have two different fibers, each with its own pair of PSP. In this basis, the initial state becomes

$$|\psi_{PSP}\rangle = |f(t_A, t_B)\rangle \otimes \left[\frac{\eta_1}{\sqrt{2}} (|p_A, p_B\rangle + e^{i\alpha_1} |p_A', p_B'\rangle) + \frac{\eta_2}{\sqrt{2}} (|p_A, p_B'\rangle - e^{i\alpha_1} |p_A', p_B\rangle) \right] \tag{3.17}$$

where

$$\eta_1 = \langle p_A|h_A\rangle \langle p_B|h_B\rangle + e^{i\alpha} \langle p_A|v_A\rangle \langle p_B|v_B\rangle$$

$$\eta_2 = \langle p_A|h_A\rangle \langle p_B'|h_B\rangle + e^{i\alpha} \langle p_A|v_A\rangle \langle p_B'|v_B\rangle$$

and α_i is defined through the relation $\eta_i = |\eta_i|e^{i(\alpha-\alpha_i)/2}$. The coefficients $\eta_{1,2}$ account for the relative orientation between the PSP's of the two fibers, or, equivalently, between the PSP of fiber A and the $\{|h\rangle, |v\rangle\}$ basis. Their absolute values are related by $|\eta_1|^2 = 1 - |\eta_2|^2$; when $|\eta_1| = 1$ (so that $|\eta_2| = 0$) the PMD vectors of the two fibers are aligned, and the initial state can still be expressed as a Φ^+ state when expanded in the basis of the PMD. As $|\eta_2|$ increases, on the other hand, the state becomes a coherent superposition of a Φ^+ and a Ψ^- state, as it's evident from Eq. (3.17).

In this convenient basis, time delays resulting from PMD in the fibers can now be easily accounted for, and the state after PMD can be written as

$$\begin{aligned} |\psi_{PMD}\rangle = &\frac{\eta_1}{\sqrt{2}} |f(t_A - \frac{\tau_A}{2}, t_B - \frac{\tau_B}{2})\rangle \otimes |p_A, p_B\rangle \\ &+ \frac{\eta_2}{\sqrt{2}} |f(t_A - \frac{\tau_A}{2}, t_B + \frac{\tau_B}{2})\rangle \otimes |p_A, p_B'\rangle \\ &- \frac{\eta_2 e^{i\alpha_2}}{\sqrt{2}} |f(t_A + \frac{\tau_A}{2}, t_B - \frac{\tau_B}{2})\rangle \otimes |p_A', p_B\rangle \\ &+ \frac{\eta_1 e^{i\alpha_1}}{\sqrt{2}} |f(t_A + \frac{\tau_A}{2}, t_B + \frac{\tau_B}{2})\rangle \otimes |p_A', p_B'\rangle \end{aligned} \tag{3.18}$$

To account for the integration time of the photon detectors, the time modes need to be

traced out of the full density matrix $|\psi_{\mathrm{PMD}}\rangle \langle \psi_{\mathrm{PMD}}|$, that is

$$
\begin{aligned}
\rho &= \int \int dt'_A dt'_B \, \langle t'_A, t'_B | \psi_{PMD} \rangle \, \langle \psi_{PMD} | t'_A, t'_B \rangle \\
&= \int \int d\omega'_A d\omega'_B \, \langle \omega'_A, \omega'_B | \psi_{PMD} \rangle \, \langle \psi_{PMD} | \omega'_A, \omega'_B \rangle \, .
\end{aligned}
$$

This calculation leads to the following density matrix:

$$
\rho = \frac{1}{2}
\begin{pmatrix}
|\eta_1|^2 & \eta_1 \eta_2^\dagger R^\dagger(0, \tau_B) & -\eta_1 \eta_2 e^{-i\alpha} R^\dagger(\tau_A, 0) & \eta_1^2 e^{-i\alpha} R^\dagger(\tau_A, \tau_B) \\
\eta_1^\dagger \eta_2 R(0, \tau_B) & |\eta_2|^2 & -(\eta_2)^2 e^{-i\alpha} R^\dagger(\tau_A, -\tau_B) & \eta_1 \eta_2 e^{-i\alpha} R^\dagger(\tau_A, 0) \\
-\eta_1^\dagger \eta_2^\dagger e^{i\alpha} R(\tau_A, 0) & -(\eta_2^\dagger)^2 e^{i\alpha} R(\tau_A, -\tau_B) & |\eta_2|^2 & -\eta_1 \eta_2^\dagger R^\dagger(0, \tau_B) \\
(\eta_1^\dagger)^2 e^{i\alpha} R(\tau_A, \tau_B) & \eta_1^\dagger \eta_2^\dagger e^{i\alpha} R(\tau_A, 0) & -\eta_1^\dagger \eta_2 R(0, \tau_B) & |\eta_1|^2
\end{pmatrix}
\tag{3.19}
$$

where the quantity $R(\tau_A, \tau_B)$ is again an overlap integral, and is defined similarly to how we did in the case of a single photon going through a PMD element. In the frequency domain we have

$$
R(\tau_A, \tau_B) = \int \int d\omega_A d\omega_B f^\dagger(\omega_A, \omega_B) f(\omega_A, \omega_B) e^{i\tau_A \omega_A} e^{i\tau_B \omega_B}, \tag{3.20}
$$

and in the case of a $\chi^{(3)}$ process $f(\omega_A, \omega_B)$ is given by Eq. (3.13). Again, we assume the state is normalized such that $R(0, 0) = 1$.

The full knowledge of the density matrix in Eq. (3.19) allows one to obtain quantities of interest about the received two-photon state. In Chapter 1 we have introduced *concurrence*, and we use it here as the entanglement monotone of choice. Finding an analytical expression for concurrence is not an easy task for a generic orientation of the PMD vectors. In order to address this issue, in the next section we introduce a convenient representation for the density matrix, namely the Fano representation.

3.2.4 Fano representation

A generic two-qubit state ρ can be expressed as [37]

$$
\rho = \frac{1}{4} \left(\sigma_0 \otimes \sigma_0 + \vec{r} \cdot \vec{\sigma} \otimes \sigma_0 + \sigma_0 \otimes \vec{s} \cdot \vec{\sigma} + \sum_{m,n=1}^{3} t_{mn} \sigma_m \otimes \sigma_n \right), \tag{3.21}
$$

where $\vec{r}$ and $\vec{s}$ are are local parameters, since they determine the marginals of ρ according to

$$
\begin{aligned}
\rho_A &= \mathrm{Tr}_B \, \rho = \frac{1}{2}(\sigma_0 + \vec{r} \cdot \vec{\sigma}), \\
\rho_B &= \mathrm{Tr}_A \, \rho = \frac{1}{2}(\sigma_0 + \vec{\sigma} \cdot \vec{s}),
\end{aligned}
\tag{3.22}
$$

and the real elements $t_{m,n} = \text{Tr}\left(\rho \sigma_m \otimes \sigma_n\right)$ form a 3×3 matrix that is usually referred to as T. When both photons experience PMD, so that the received state is represented by the density matrix in Eq. (3.19), one can easily see that the reduced density matrices are maximally mixed, namely

$$\rho_A = \rho_B = \frac{1}{2}\begin{pmatrix} 1 & 0 \\ 0 & 1 \end{pmatrix}, \tag{3.23}$$

meaning that $\vec{r}$ and $\vec{s}$ are null and the state belongs to the class of Bell-diagonal states, represented by

$$\rho = \frac{1}{4}\left(\sigma_0 \otimes \sigma_0 + \sum_{m,n=1}^{3} t_{mn}\sigma_m \otimes \sigma_n\right). \tag{3.24}$$

For the density matrix (3.19), one can analytically evaluate T and express it in terms of the system parameters. If we make the realistic assumption on the symmetry of the two filters $|H_A(\omega_A)H_B(-\omega_B)| = |H_A(-\omega_A)H_B(\omega_B)|$, then the function $R(\tau_A, \tau_B)$ is real-valued. Additionally, we can always choose an appropriate basis in which the parameters η_1 and η_2 are real; this makes the matrix in (3.19) real-valued, and finding T becomes a simpler task. Straightforward algebra leads in fact to

$$T = \begin{pmatrix} R(\tau_A, \tau_B)\eta_1^2 - R(\tau_A, -\tau_B)\eta_2^2 & 0 & -2R(\tau_A, 0)\eta_1\eta_2 \\ 0 & -R(\tau_A, \tau_B)\eta_1^2 - R(\tau_A, -\tau_B)\eta_2^2 & 0 \\ 2R(0, \tau_B)\eta_1\eta_2 & 0 & 1 - 2\eta_2^2 \end{pmatrix}. \tag{3.25}$$

Equation (3.24) can be further simplified by noting that a product transformation $U_1 \otimes U_2$ can always be found that transforms ρ into a form with a diagonal T [37]. In fact, for every 2×2 unitary transformation U, there exists a 3×3 rotation matrix O, such that

$$U\hat{n} \cdot \vec{\sigma} U^\dagger = (O\hat{n}) \cdot \vec{\sigma}. \tag{3.26}$$

When a product transformation $U_1 \otimes U_2$ is applied to a state ρ, the corresponding parameters are transformed to

$$\begin{aligned} \vec{r}\,' &= O_1\vec{r} \\ \vec{s}\,' &= O_2\vec{s} \\ T' &= O_1 T O_2^\dagger, \end{aligned} \tag{3.27}$$

where the connection between O_i and U_i is given by Eq.(3.26).

Finding the rotations O_1 and O_2 is not an easy task; it is usually a lot easier to solve the equivalent problem of diagonalizing the operator $TT^\dagger = O_1^\dagger T' O_2 O_2^\dagger T'^\dagger O_1 = O_1^\dagger T' T'^\dagger O_1$.

Writing down the operator as

$$TT^\dagger = \begin{pmatrix} m_{11} & 0 & m_{13} \\ 0 & m_{22} & 0 \\ m_{13} & 0 & m_{33} \end{pmatrix},$$

(3.28)

with

$$m_{11} = [R(\tau_A, \tau_B)\eta_1^2 - R(\tau_A, -\tau_B)\eta_2^2]^2 + 4R(\tau_A, 0)$$
$$m_{13} = 2R(0, \tau_B)\eta_1\eta_2[R(\tau_A, \tau_B)\eta_1^2 - R(\tau_A, -\tau_B)\eta_2^2] - 2R(\tau_A, 0)(1 - 2\eta_2^2)$$
$$m_{22} = [R(\tau_A, \tau_B)\eta_1^2 + R(\tau_A, -\tau_B)\eta_2^2]^2$$
$$m_{33} = 4R^2(0, \tau_B)\eta_1^2\eta_2^2 + (1 - 2\eta_2^2)^2,$$

(3.29)

we can compute the eigenvalues of $TT^\dagger$:

$$\lambda_1 = m_{22}$$
$$\lambda_2 = \frac{m_{11} + m_{33} - \sqrt{4m_{13}^2 + (m_{11} - m_{33})^2}}{2}$$
$$\lambda_3 = \frac{m_{11} + m_{33} + \sqrt{4m_{13}^2 + (m_{11} - m_{33})^2}}{2}.$$

(3.30)

The coefficients t_i' that constitute the diagonal matrix T', can now be evaluated from the eigenvalues λ_i by simply taking either one of the corresponding squared roots; since not all combinations lead to valid density matrices, we will pick them according to

$$t_1' = \sqrt{\lambda_1}$$
$$t_2' = -\sqrt{\lambda_2}$$
$$t_3' = \sqrt{\lambda_3}.$$

(3.31)

After dropping the apex of the coefficients, the state ρ becomes

$$\rho = \frac{1}{4}\left(\sigma_0 \otimes \sigma_0 + \sum_{i=1}^{3} t_i\sigma_i \otimes \sigma_i\right),$$

(3.32)

and we are now in a position to express the concurrence of the two-photon state in terms of
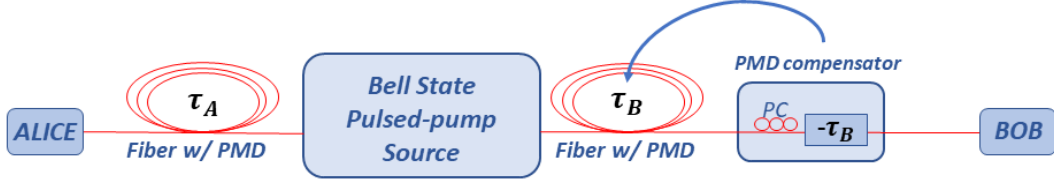
Figure 3.2: Schematic of an entanglement distribution system in which only one of the two photons (photon A) experiences PMD during its propagation. Bob has a PMD compensator that can be adjusted both in magnitude and orientation (via the polarization controller PC) to compensate for the PMD on his side.

the system parameters. Equation (3.32) can in fact be written as

$$
\rho = \frac{1}{4}
\begin{pmatrix}
1 + t_3 & 0 & 0 & t_1 - t_2 \\
0 & 1 - t_3 & t_1 + t_2 & 0 \\
0 & t_1 + t_2 & 1 - t_3 & 0 \\
t_1 - t_2 & 0 & 0 & 1 + t_3
\end{pmatrix},
\tag{3.33}
$$

that is, Bell diagonal states are a particular realization of the so-called *X-states*, for which concurrence can be analytically evaluated to be [38]

$$
\begin{aligned}
C &= 2 \max \left\{ 0, |\rho_{23}| - \sqrt{\rho_{11}\rho_{44}}, |\rho_{14}| - \sqrt{\rho_{22}\rho_{33}} \right\} \\
&= \frac{1}{2} \max \left\{ 0, |t_1 + t_2| - 1 - t_3, |t_1 - t_2| - 1 + t_3 \right\},
\end{aligned}
\tag{3.34}
$$

where we can remove the absolute value arising from taking the squared root of $(1 \pm t_3)^2$ because $|t_3| \leq 1$. Using Eq.(3.31), we can finally write the concurrence as

$$
C = \frac{1}{2} \max \left\{ 0, \sqrt{\lambda_1} + \sqrt{\lambda_2} + \sqrt{\lambda_3} - 1 \right\}.
\tag{3.35}
$$

3.3   PMD in one arm

The density matrix in Eq. (3.19) describes the received two-photon state in the general case in which both photons propagate in channels affected by the presence of PMD. Both the magnitude and the orientation of the two PMD vectors can be changed to obtain specific configurations. In this section we consider the scenario where the presence of PMD only affects the channel of the photon propagating towards Alice, that is, $\tau_B = 0$. This may be

the case in a series of scenarios: the second photon could be kept in the proximity of the source (as several protocols require), or simply Bob could have a tunable PMD element that could use to compensate for the PMD on his side, as schematically depicted in Fig. 3.2.

When $\tau_B = 0$, the initial state can always be expressed as a Φ^+ state in terms of the PSP of the fiber in channel A, regardless of their relative alignment with the $\{h, v\}$ basis [39]. The consequence is that we can always assume that in this specific scenario $|\eta_1| = 1$ and $|\eta_2| = 0$, so that the density matrix of the received state becomes

$$\rho = \frac{1}{2} \begin{pmatrix} 1 & 0 & 0 & R^\dagger(\tau_A, 0) \\ 0 & 0 & 0 & 0 \\ 0 & 0 & 0 & 0 \\ R(\tau_A, 0) & 0 & 0 & 1 \end{pmatrix}. \tag{3.36}$$

The concurrence of this state is given by

$$C = |R(\tau_A, 0)|, \tag{3.37}$$

which is clearly orientation-independent, and only depends on the amount of PMD in the channel. The behavior of concurrence as a function of the DGD in channel A is shown as a dashed line in Fig. 3.3(a); one can see how the degree of entanglement asymptotically approaches zero as the DGD in the channel increases.

From the density matrix in Eq. (3.36) it is also easy to find an analytical expression for the mutual information, that is

$$I(\rho) = 1 + \frac{|R(\tau_A, 0)|}{2} \log_2 \left(\frac{1 + |R(\tau_A), 0|}{1 - |R(\tau_A, 0)|} \right) + \frac{1}{2} \log_2 \left(1 - |R(\tau_A, 0)|^2 \right). \tag{3.38}$$

This quantity is again orientation-independent, and its behavior as a function of the amount of PMD in channel A is presented in Fig. 3.3(b) as a dashed line. As the DGD in the channel is increased, the mutual information of the two-photon state asymptotically approaches one from above. Notice that since the concurrence is given by $C = |R(\tau_A, 0)|$, in this scenario the mutual information and concurrence are in a one-to-one correspondence, which is usually not the case. The fact that the mutual information is bounded to be above one implies the presence of correlations that are stronger than the classical ones, and that can thus only exist when the state is entangled (i.e., $C > 0$).
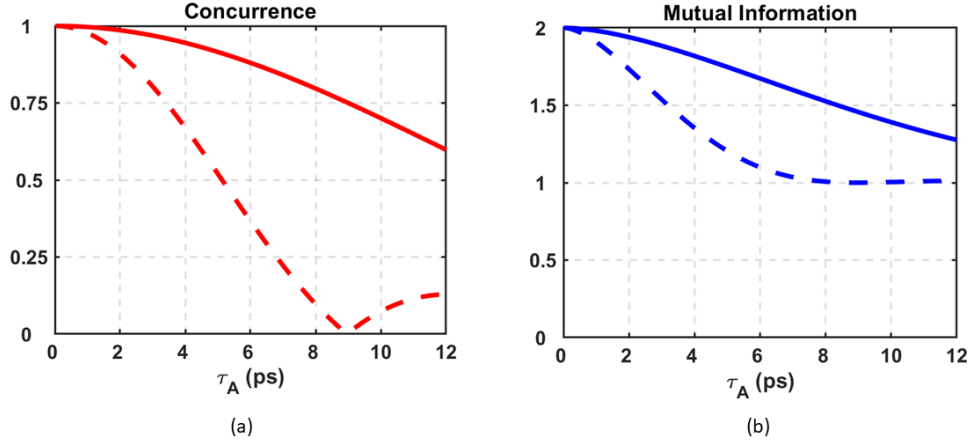
Figure 3.3: Concurrence (a) and quantum mutual information (b) as functions of the amount of PMD in channel A. The dashed lines refer to the case in which PMD is only present in channel A: both concurrence and mutual information are independent of the orientation of $\vec{\tau}_A$ (see also [39]). Solid lines show the nonlocal compensation of PMD: Bob introduces a second controlled PMD element of the same magnitude and orientation of $\vec{\tau}_A$ to recover concurrence and mutual information.

3.4   Nonlocal compensation of PMD

If Bob has an additional tunable PMD element, he can employ the nonlocal nature of entanglement to perform nonlocal compensation of PMD. This situation is schematically presented in Fig. 3.4: Bob uses the first PMD element PMDB1 to compensate for the PMD on his side, and then tunes the second PMD element PMDB2 to compensate for the PMD on Alice's side. The resulting scenario is equivalent to the one depicted in Fig. 3.1, with the difference lying in the fact that this time the PMD element on Bob's side is a controlled one; the state will thus again be described by the density matrix in Eq. (3.19), in which τ_A represents the (potentially unknown) DGD of the fiber in channel A, while τ_B represents the DGD introduced by Bob's second PMD element, as schematically depicted in Fig. 3.3.

Clearly, a careful choice of both the orientation and magnitude of the PMD element PMDB2 that he controls is essential for this compensation scheme to work effectively. First, Bob needs to make sure that his PMD element is aligned with the PMD vector that characterizes the fiber on Alice's side. This situation is equivalent to setting $|\eta_1| = 1$ in the density matrix in Eq. (3.19) so that it is reduced to a form whose only nonzero elements are the four corners,

namely

$$\rho = \frac{1}{2} \begin{pmatrix} 1 & 0 & 0 & R^{\dagger}(\tau_A, \tau_B) \\ 0 & 0 & 0 & 0 \\ 0 & 0 & 0 & 0 \\ R(\tau_A, \tau_B) & 0 & 0 & 1 \end{pmatrix}. \tag{3.39}$$

Note that this is equivalent to the one in Eq. (3.36) (which described the case of PMD affecting only one photon) where $R(\tau_A, 0)$ is to be replaced by $R(\tau_A, \tau_B)$. The concurrence of this state is then given by $C = |R(\tau_B, \tau_B)|$, and to obtain its maximum value we need to choose a specific value of τ_B that, in general, will be a function of both τ_A and the bandwidth of the pump and filters used in the channels.

Maximizing the concurrence function is not a task that can be performed analytically when the spectra of pump and filters have a generic shape. In [35] it was shown that for gaussian pump and filters Bob would need to set his DGD to $\tau_B^{\text{opt}} = \tau_A/(1 + B_P^2/B_A^2)$ as the optimum compensation value, where B_P and B_A are the bandwidths of the pump and filter in Alice's channel, respectively. We note that the maximum concurrence usually occurs for a similar value also in the case in which the pump and bandwidths have the shape of a third-order supergaussian.

In Fig. 3.3 we show the compensated case for concurrence (a) and mutual information (b) as solid lines, in comparison to the uncompensated case (dashed lines). To obtain this figures, we assume that Bob has made sure that his PMD element is aligned with $\vec{\tau}_A$ (so that $|\eta_1| = 1$) and has fixed its magnitude to match that of Alice's fiber, i.e. $\tau_B = \tau_A$. In this way, he can recover both concurrence and mutual information, at least partially. It is in fact worth noticing that, as evident from inspection of Fig. 3.3, compensation is not perfect, and the restoration of concurrence and mutual information becomes less and less effective as the amount of PMD in channel A increases. This is a consequence of the fact that a pulsed pump is assumed to generate the entangled photons. Full compensation, on the other hand, is achievable only if a CW pump is used, and both concurrence and quantum mutual information can be restored to their initial values. As noted in [35] in fact, a pump with a finite bandwidth creates an absolute time reference, which in principle would allow one to tell if the photons' polarization was aligned with the slow or fast axis based on their time of arrival relative to the pump's time reference, even when the two photons are detected at the same time (that is, after compensation). This would clearly not be the case when a CW pump is employed in the generation of the photon pair; in this scenario, no absolute time reference would be introduced by the pump, and it would be impossible to guess the received photons' polarization simply based on their time of arrival.
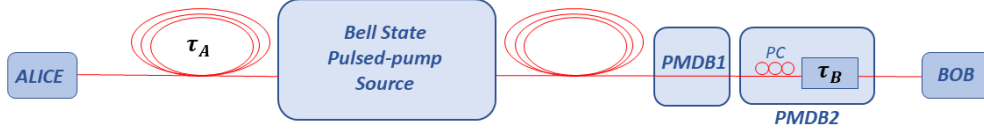
Figure 3.4: Schematic representation of the nonlocal PMD compensation scheme. Bob can operate two tunable (in magnitude and orientation) PMD elements. He uses the first one (PMDB1) to compensate for the PMD in his fiber, and the second one (PMDB2, with a DGD given by τ_B) to try to achieve nonlocal compensation of the PMD in Alice's fiber, which is characterized by a DGD τ_A.

3.5   A Quantum Information Theory perspective

In Chapter 1 we introduced a simple visual aid to represent how the information content of a state is shared among different parts of the state itself, namely the entropic Venn diagrams. The aim of this section is to build these kinds of diagrams for the case that we have been describing up until now. We have shown in fact how the presence of PMD in the channel of one or both photons causes a coupling between their polarization and their times of arrival. This can be seen as a coupling with the environment, which causes a leakage of information from the polarization degree of freedom towards the time-dependent part of the state, which we will generally refer to as the "environment" in what follows. The Venn diagrams will then clarify how a part of information is lost when our two-particle system becomes entangled with the environment.

We know that the received two-photon state $|\Psi\rangle$ when PMD is present in the path of both photons can be described by Eq. (3.18). In order to build a Venn diagram that has von Neumann entropies as its entries, it is necesary to know the density matrix of the complete state (as well as several reduced density matrices of the subsystems). The issue with this state is that, in general, the time-dependent kets do not form an orthogonal basis, and thus a density matrix with a finite number of entries cannot be obtained from a state in the form of Eq. (3.18). We thus start by describing the special case in which the time kets form an orthonormal basis. From now on we will use a slightly different notation to label the time-dependent kets, namely

$$|f(t_A \pm \frac{\tau_A}{2}, t_B \pm \frac{\tau_B}{2})\rangle = |f_{\pm\pm}\rangle, \tag{3.40}$$

so that the complete state can be written in a slightly less cumbersome fashion.

3.5.1 Time kets form an orthonormal basis

It is instructive to start with an simpler scenario, in which the time-dependent kets form an orthonormal basis; this happens if we deal with large enough DGD's, so that the anticipated and delayed replicas don't overlap with the original pulse. In this case the density operator $|\Psi\rangle\langle\Psi|$ is a 16×16 matrix, from which all of the reduced density matrices can be easily evaluated; for example, for the polarization dependent part of the state, obtained after tracing over the time modes, one has:

$$\rho^{AB} = \frac{1}{2} \begin{pmatrix} |\eta_1|^2 & 0 & 0 & 0 \\ 0 & |\eta_2|^2 & 0 & 0 \\ 0 & 0 & |\eta_2|^2 & 0 \\ 0 & 0 & 0 & |\eta_1|^2 \end{pmatrix}, \tag{3.41}$$

which is consistent with the density matrix in Eq. (3.19), where the $R(\tau_A, \tau_B)$ functions vanish because of the very large DGD's in the channels. The von Neumann entropy of this matrix reads:

$$S(\rho^{AB}) = 1 - \log_2\left(1 - |\eta_1|^2\right) + |\eta_1|^2 \log_2\left(\frac{1 - |\eta_1|^2}{|\eta_1|^2}\right) = S,$$

and it is a function of $|\eta_1|^2$ only; we will refer to this quantity as S. The concurrence of this state, on the other hand, is clearly always zero, meaning that for very high DGD's the received two-photon state is separable.

In a similar fashion, one can evaluate the other reduced density matrices needed to build the Venn diagrams, and obtains the following relations for the von Neumann entropies:

$$S(\rho^E) = S,$$
$$S(\rho^A) = S(\rho^B) = 1,$$
$$S(\rho^{AE}) = S(\rho^{BE}) = 1,$$
$$S(\rho^{ABE}) = 0.$$

We can now represent the entropies in the form of a Venn diagram; all of the entries of this diagram can be evaluated using the relations (1.38 − 1.40), that we report here for convenience:

$$S(A:B:E) = S(A) + S(B) + S(E) - S(AE) - S(AB) - S(BE) + S(ABE),$$

$$S(A|BE) = S(ABE) - S(BE), \tag{3.42}$$

$$S(A:B|E) = S(AE) + S(BE) - S(E) - S(ABE).$$

The Venn diagram is shown in Fig. 3.5. Clearly, all the quantities can be expressed as a function of $S = S(\rho^{AB}) = S(AB)$, the von Neumann entropy of the polarization part of the state. This has the practical advantage that this quantity can be easily extracted from the density matrix of the polarization part of the state, which can be experimentally obtained by means of regular tomography.

The quantity S ranges between 1 and 2. For $|\eta_1|^2 = 0, 1$, one has $S = 1$ and the Venn diagram becomes that of a GHZ state

$$|\Psi_{\mathrm{GHZ}}\rangle = \frac{1}{\sqrt{2}}(|000\rangle + 111), \tag{3.43}$$

which shows perfect entanglement between the three parts of the state, as expected: the photons are now fully distinguishable based on their time of arrival. When $|\eta_1|^2 = 1/2$, $S = 2$, and this case is not as intuitive as the former, due to the fact that one of the three sets (the "environment" one) has dimensionality four, and thus the entropies take on values that are not usual. The quantum mutual information shared between the polarization of photon A and B is represented by the quantity inside the intersection between the sets A and B. As expected, since the reduced density matrices ρ^A and ρ^B are proportional to the identity matrix, one simply has $I(\rho^{AB}) = 2 - S$.

In Fig. 3.5(b) we also show a two-party Venn Diagram, in which the polarization parts are taken as a whole, and the second set is again represented by the environment part. This kind of diagram shows more clearly how as the two-photon state gets decohered by PMD, the mutual information with the environment increases, the quantity in the intersection between the two sets being equal to $2S$.

3.5.2   General case

The general case in which the time kets are not orthonormal can be treated formally by the creation of a new orthonormal basis. This can be achieved via a Gram-Schmidt procedure,
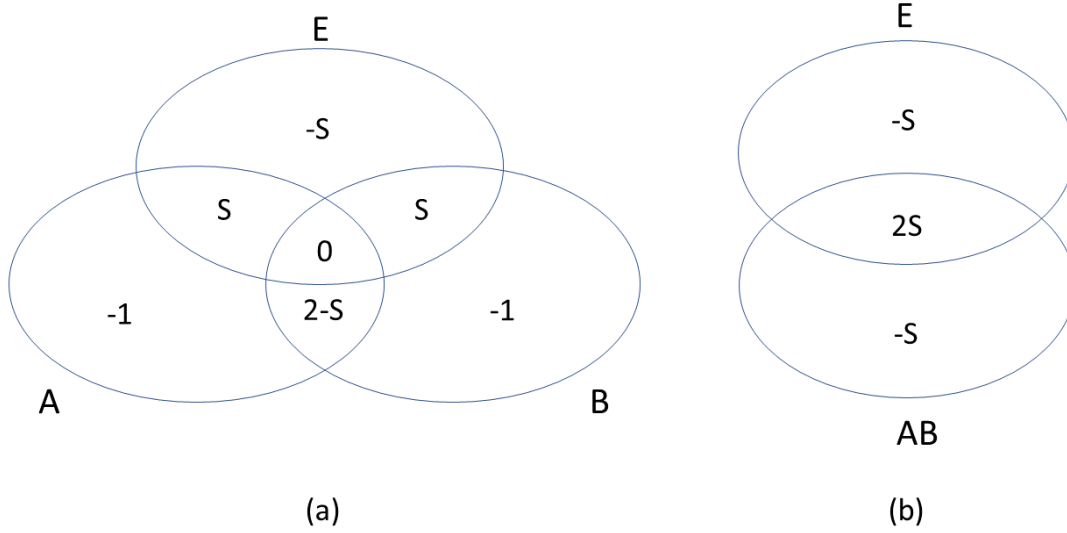
Figure 3.5: Venn diagram of the state undergoing PMD; on the left, we show the three degrees of freedom, on the right the polarizations are grouped into one set.

defining the vectors of the new basis as follows:

$$|f_1\rangle = |f_{--}\rangle \,,$$

$$|f_2\rangle = \frac{|f_2'\rangle}{N_2} = \frac{|f_{++}\rangle - \langle f_{--}|f_{++}\rangle |f_{--}\rangle}{N_2} \,,$$

$$|f_3\rangle = \frac{|f_3'\rangle}{N_3} = \frac{1}{N_3}|f_{+-}\rangle - \frac{1}{N_3}\langle f_{--}|f_{+-}\rangle |f_{--}\rangle +$$

$$- \frac{1}{N_3}\left(\frac{\langle f_{++}| - \langle f_{++}|f_{--}\rangle\langle f_{--}|}{N_2} |f_{+-}\rangle \frac{|f_{++}\rangle - \langle f_{--}|f_{++}\rangle |f_{--}\rangle}{N_2} \right) \,,$$

$$|f_4\rangle = \frac{|f_4'\rangle}{N_4} = \frac{|f_{-+}\rangle - \langle f_1|f_{-+}\rangle |f_1\rangle - \langle f_2|f_{-+}\rangle |f_2\rangle - \langle f_3|f_{-+}\rangle |f_3\rangle}{N_4} \,,$$

where N_2, N_3, N_4 are the normalization coefficient defined as

$$N_i = \sqrt{\langle f_i'|f_i'\rangle} \,,$$

with $i = \{2, 3, 4\}$.

After noticing that the inner products can be related to the overlapping function $R(\tau_A, \tau_B)$

introduced earlier according to

$$\langle f_{jk}|f_{j'k'}\rangle = R\left(-j\frac{\tau_A}{2} + j'\frac{\tau_A}{2}, -k\frac{\tau_B}{2} + k'\frac{\tau_B}{2}\right),$$

with $\{j, j', k, k'\}$ that can take on the values $\{+, -\}$ (so that, for example, $\langle f_{--}|f_{++}\rangle = R(\tau_A, \tau_B)$). We remind the reader that the R functions are normalized such that $R(0,0) = 1$.

Expressing the vectors of the new basis as a combination of the vectors of the old basis results in

$$\begin{pmatrix} |f_1\rangle \\ |f_2\rangle \\ |f_3\rangle \\ |f_4\rangle \end{pmatrix} = \begin{pmatrix} 1 & 0 & 0 & 0 \\ \frac{a_{21}}{N_2} & \frac{1}{N_2} & 0 & 0 \\ \frac{a_{31}}{N_3} & \frac{a_{32}}{N_3} & \frac{1}{N_3} & 0 \\ \frac{a_{41}}{N_4} & \frac{a_{42}}{N_4} & \frac{a_{43}}{N_4} & \frac{1}{N_4} \end{pmatrix} \begin{pmatrix} |f_{--}\rangle \\ |f_{++}\rangle \\ |f_{+-}\rangle \\ |f_{-+}\rangle \end{pmatrix}, \tag{3.44}$$

where the entries of the matrix are obtained as follows:

$$a_{21} = -R(\tau_A, \tau_B),$$

$$a_{31} = \frac{R(\tau_A, 0) - R(\tau_A, \tau_B)R(0, \tau_B)}{N_2^2},$$

$$a_{32} = \frac{R^\dagger(0, \tau_B) - R^\dagger(\tau_A, \tau_B)R(\tau_A, 0)}{N_2^2},$$

$$a_{41} = -R(0, \tau_B) + \frac{R^\dagger(\tau_A, 0) - R(\tau_A, \tau_B)R(0, \tau_B)}{N_2^2}R(\tau_A, \tau_B)+$$

$$\quad - a_{31}\frac{R^\dagger(\tau_A, -\tau_B) + a_{31}R(0, \tau_B) - a_{32}R^\dagger(\tau_A, 0)}{N_3^2},$$

$$a_{42} = -\frac{R^\dagger(\tau_A, 0) - R(\tau_A, \tau_B)R(0, \tau_B)}{N_2^2} + a_{32}\frac{R^\dagger(\tau_A, -\tau_B) + a_{31}R(0, \tau_B) - a_{32}R^\dagger(\tau_A, 0)}{N_3^2},$$

$$a_{43} = -\frac{R^\dagger(\tau_A, -\tau_B) + a_{31}R(0, \tau_B) - a_{32}R^\dagger(\tau_A, 0)}{N_3^2},$$

and the normalization coefficients introduced above can now be explicitly written as

$$N_2 = \sqrt{1 - |R(\tau_A, \tau_B)|^2},$$

$$N_3 = \sqrt{1 + |a_{31}|^2 + |a_{32}|^2 + 2Re\{a_{31}R^\dagger(\tau_a, 0) + a_{32}R(0, \tau_B) + a_{31}^\dagger a_{32}R(\tau_A, \tau_B)\}},$$

$$N_4 = \left(1 + |a_{41}|^2 + |a_{42}|^2 + |a_{43}|^2 + 2Re\{a_{41}^\dagger a_{42}R^\dagger(\tau_a, \tau_B) + a_{41}^\dagger a_{43}R(\tau_A, 0) \right.$$

$$\left. + a_{41}^\dagger R(0, \tau_B) + a_{42}a_{43}^\dagger R(0, \tau_B) + a_{42}R(\tau_A, 0)a_{43}R(\tau_A, -\tau_B)\} \right)^{1/2}.$$

In order to express the state in Eq. (3.18) in terms of the new basis, we need to invert the

transformation matrix. Since the latter is a triangular matrix, its inverse is also triangular, with the diagonal terms that are the inverse of the diagonal entries of the first matrix; it thus takes the form:

$$
\begin{pmatrix} |f_{--}\rangle \\ |f_{++}\rangle \\ |f_{+-}\rangle \\ |f_{-+}\rangle \end{pmatrix} = \begin{pmatrix} 1 & 0 & 0 & 0 \\ m_{21} & N_2 & 0 & 0 \\ m_{31} & m_{32} & N_3 & 0 \\ m_{41} & m_{42} & m_{43} & N_4 \end{pmatrix} \begin{pmatrix} |f_1\rangle \\ |f_2\rangle \\ |f_3\rangle \\ |f_4\rangle \end{pmatrix},
\tag{3.45}
$$

or, expressing every entry in terms of the elements of the change of basis matrix:

$$
\begin{pmatrix} |f_{--}\rangle \\ |f_{++}\rangle \\ |f_{+-}\rangle \\ |f_{-+}\rangle \end{pmatrix} = \begin{pmatrix} 1 & 0 & 0 & 0 \\ -a_{21} & N_2 & 0 & 0 \\ a_{21}a_{32} - a_{31} & -N_2 a_{32} & N_3 & 0 \\ a_{21}(a_{42} - a_{32}a_{43}) - a_{41} + a_{31}a_{43} & -N_2(a_{42} - a_{32}a_{43}) & -N_3 a_{43} & N_4 \end{pmatrix} \begin{pmatrix} |f_1\rangle \\ |f_2\rangle \\ |f_3\rangle \\ |f_4\rangle \end{pmatrix}.
\tag{3.46}
$$

After some algebra, the latter becomes:

$$
\begin{pmatrix} |f_{--}\rangle \\ |f_{++}\rangle \\ |f_{+-}\rangle \\ |f_{-+}\rangle \end{pmatrix} = \begin{pmatrix} 1 & 0 & 0 & 0 \\ R(\tau_A, \tau_B) & N_2 & 0 & 0 \\ R(\tau_A, 0) & \frac{R^\dagger(0,\tau_B) - R(\tau_A,0)R^\dagger(\tau_A,\tau_B)}{\sqrt{1-|R(\tau_A,\tau_B)|^2}} & N_3 & 0 \\ R(0, \tau_B) & \frac{R^\dagger(\tau_A,0) - R(0,\tau_B)R(\tau_A,\tau_B)}{\sqrt{1-|R(\tau_A,\tau_B)|^2}} & \frac{R(\tau_A,-\tau_B) + a_{31}R(0,\tau_B) - a_{32}R^\dagger(\tau_A,0)}{N_3} & N_4 \end{pmatrix} \begin{pmatrix} |f_1\rangle \\ |f_2\rangle \\ |f_3\rangle \\ |f_4\rangle \end{pmatrix}
\tag{3.47}
$$

We are now in the position to express the state in Eq. (3.18) in terms of the new orthonormal basis:

$$
\begin{aligned}
|\Psi\rangle = &\frac{1}{\sqrt{2}}\eta_1[|f_1\rangle|p_A\rangle|p_B\rangle + m_{21}|f_1\rangle|p'_A\rangle|p'_B\rangle + m_{22}|f_2\rangle|p'_A\rangle|p'_B\rangle] + \\
&- \frac{1}{\sqrt{2}}\eta_2[m_{31}|f_1\rangle + m_{32}|f_2\rangle + m_{33}|f_3\rangle]|p'_A\rangle|p_B\rangle + \\
&+ \frac{1}{\sqrt{2}}\eta_2[m_{41}|f_1\rangle + m_{42}|f_2\rangle + m_{43}|f_3\rangle + m_{44}|f_4\rangle]|p_A\rangle|p'_B\rangle
\end{aligned}
\tag{3.48}
$$

Once we have the state in this form, evaluating the 16×16 complete density matrix, as well as the reduced density matrices, is straightforward. Note that the reduced density matrix ρ^{AB} that we obtain in this fashion is exactly the same as that of Eq. (3.19).

Consistently with our previous notation, we can denote by S the entropy of the reduced density matrix that accounts for the polarization of the photons ρ^{AB}, and express all the
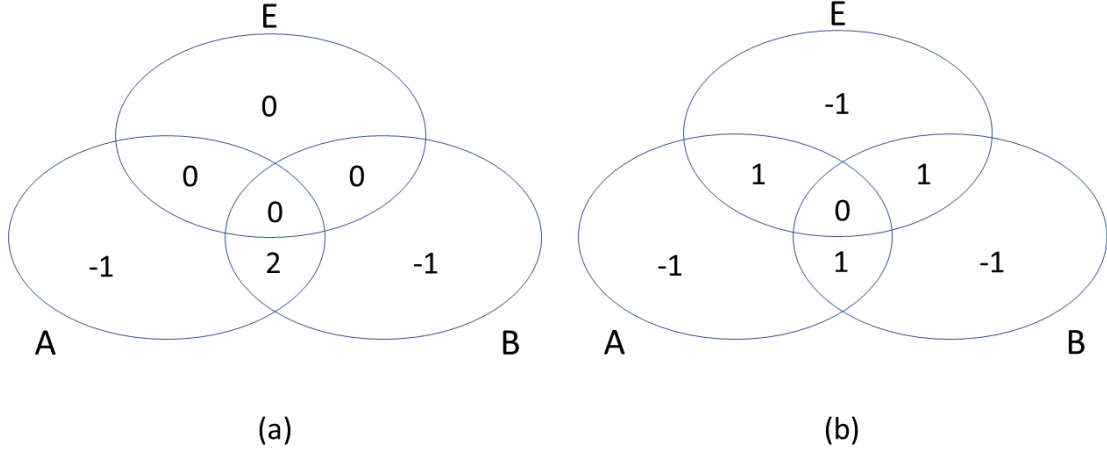
Figure 3.6: Venn diagram of the state undergoing PMD in the case of perfect alignment, in the two limit cases: on the left, $S = 0$, the two pulses perfectly overlap, and there is no coupling with the environment; on the right, $S = 1$, the two pulses can be distinguished as they don't overlap, and the total system becomes a GHZ state, showing maximal entanglement between the photons' polarizations and the environment.

other entropies in terms of this quantity. Again, algebra leads to the relations:

$$S(\rho^{AB}) = S,$$
$$S(\rho^{E}) = S,$$
$$S(\rho^{A}) = S(\rho^{B}) = 1,$$
$$S(\rho^{AE}) = S(\rho^{BE}) = 1,$$
$$S(\rho^{ABE}) = 0,$$

which allow us to obtain a Venn diagram that is exactly the same as the one in Fig. 3.5. The only difference is that S, which still represents the von Neumann entropy of ρ^{AB}, now has a different value, since it will not be a function of $|\eta_1|^2$ only, and in general will not have a simple analytical expression.

It is of interest to consider the case of perfect alignment, i.e. $\eta_1 = 1$; in this case ρ^{AB} becomes

the one described by Eq. (3.39) and its von Neumann entropy can be easily expressed as:

$$S(\rho^{AB}) = S = 1 - \frac{|R(\tau_A, \tau_B)|}{2} \log_2 \left(\frac{1 + |R(\tau_A, \tau_B)|}{1 - |R(\tau_A, \tau_B)|} \right) - \frac{1}{2} \log_2 \left(1 - |R(\tau_A, \tau_B)|^2 \right). \quad (3.49)$$

In this case, S is a function of $|R(\tau_A, \tau_B)|$ only, and it ranges from 0 to 1, the limiting cases occurring for $|R(\tau_A, \tau_B)| = 1$ and $|R(\tau_A, \tau_B)| = 0$, respectively (that is, the two pulses overlap perfectly or do not overlap at all).

The Venn diagram is again the one shown in Fig. 3.5, with the difference that S is now given by Eq. (3.49) and varies from 0 to 1. The two limiting cases are presented in Fig. 3.6: on the left, the case corresponding to $S = 0$ ($|R(\tau_A, \tau_B)| = 1$), and on the right the one corresponding to $S = 1$ ($|R(\tau_A, \tau_B)| = 0$). In the former, the fact that the two pulses are perfectly overlapping ensures that no coupling with the environment takes place (there's no way of discriminating one polarization from the other based on the times of the arrival of the photons); in the latter, the two pulses do not overlap at all, meaning that one can tell them apart by simply looking at the times of arrival: polarization entanglement is lost to the environment, and a GHZ state is obtained.

3.5.3 Conditional Entropy $S(A|B)$

A quantity that might be of interest is the entropy of photon A conditional to the knowledge of the polarization of photon B, i.e. $S(A|B) = S(AB) - S(B)$. In order to evaluate this quantity, we first need to trace out the time-dependent part of the state, thus obtaining a 4×4 reduced density matrix ρ^{AB}. Once we do this, it is really easy to see directly from the Venn diagram that this reduced entropy equals $S - 1$ (by definition, it is the quantity that is in the set A and outside of the intersection with the set B). If we now fix the main parameters of the system, we can observe how $S(A|B)$ varies with the relative orientation of the PMD axes. In Fig. 3.7, one can see the behavior of $S(A|B)$ as a function of $|\eta_1|^2$, along with the concurrence C of the two photon state, for three different values of pump bandwidth (while the DGD are fixed, $\tau_A = \tau_B = 6.6$ ps). Notice that the conditional entropy can become negative, which indicates the presence of nonclassical correlations that cause the marginal states to have a higher entropy than the complete state. Negative conditional entropy clearly only occurs for nonzero concurrence, but it is not a necessary condition for the state to be entangled (one can easily see large portions of the curves that have non-vanishing concurrence – i.e., the state is entangled – but positive $S(A|B)$).

3.5.4 Concurrence and mutual information

We conclude this section by briefly discussing the relation between the concurrence and the quantum mutual information in the scenario that we're studying. It is well known that while
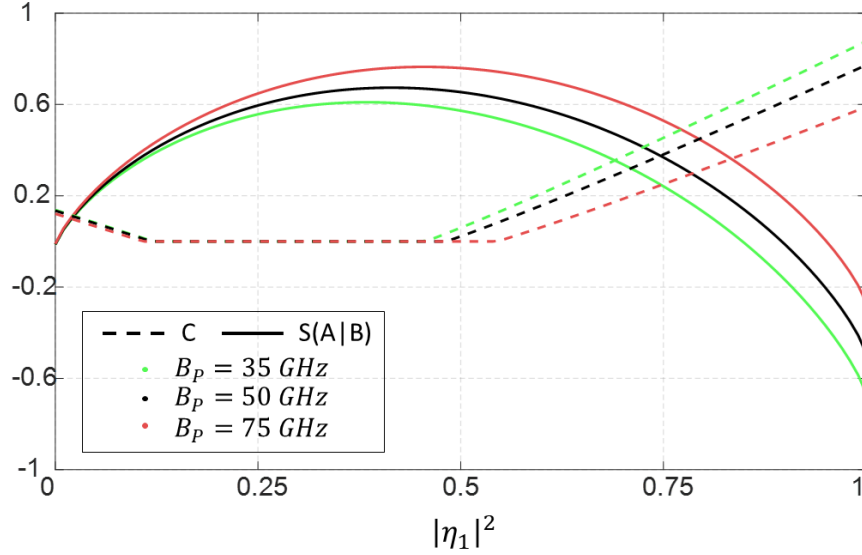
Figure 3.7: Conditional entropy $S(A|B)$ and concurrence C as function of the parameter $|\eta_1|^2$ that quantifies the relative orientation of the PMD vectors, for three pump bandwidths B_P. The pump is assumed to be a third order supergaussian, and the DGD's are set to $\tau_A = \tau_B = 6.6$ ps.
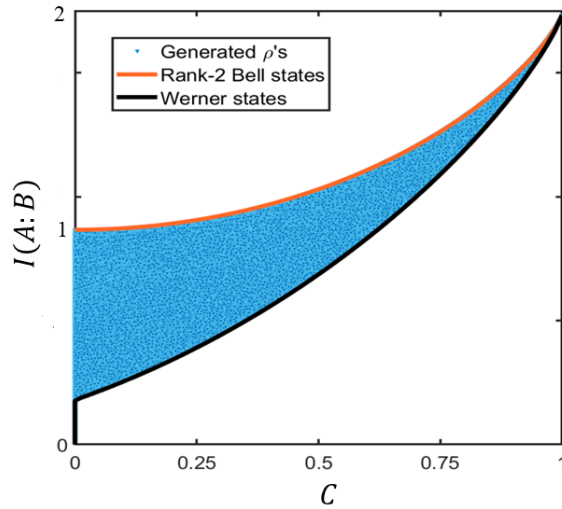
Figure 3.8: Mutual Information $I(A:B)$ versus Concurrence C for about 200,000 generated density matrices in the form of Eq. (3.19), when both photons of the input Bell state go through channels with PMD; the points are obtained by varying the system parameters (pump and filters bandwidth, DGDs, relative orientation of PMD vectors). The black and orange borders correspond to received Werner states and rank-2 Bell states, respectively.

concurrence is an entanglement monotone, and is thus a proper quantity to determine the degree of entanglement of a state, mutual information is not, and no one-to-one relation is expected to exist between the two. Nonetheless, in the previous sections we have shown that under specific circumstances (for example, PMD affecting the propagation of only one photon) an explicit relation between the two can exist (like the one in Eq. (3.38)).

The general case for the scenario in which PMD affects the propagation of both photons is presented in Fig. 3.8. In a plane where on the x-axis we have concurrence, and on the y-axis we have mutual information, we represent all their possible combinations in the case in which the received two-photon state is described by the density matrix in Eq. (3.19). The matrices have been numerically generated by varying the main system parameters (pump and filters bandwidth, DGD's, relative orientation of the PMD vectors), and for each matrix concurrence and mutual information have been extracted, and used as the coordinates for the blue points in the figure. Two features are apparent: the first is that mutual information can be nonzero even for vanishing concurrence; the second is that, even if in the general case no one-to-one relation between concurrence and mutual information exists, all data points fall in a region bounded by two curves corresponding to well-defined classes of received states. The upper bound is obtained for aligned PSP ($|\eta_1| = 1$), in which case the density matrix is described by Eq. (3.39). With no loss of generality we can assume that R is real-valued, in which case the matrix in Eq. (3.39) is in the form of a rank-2 Bell diagonal state and can be expressed as

$$\rho_{\mathrm{UB}} = \frac{1+C}{2} \, |\phi^+\rangle \, \langle\phi^+| + \frac{1-C}{2} \, |\phi^-\rangle \, \langle\phi^-| . \tag{3.50}$$

On the other hand, we show numerically how the points of the lower bound correspond to Werner states, which are known to be defined as a mixture of a maximally entangled pure state and a fully mixed state (that is, a pure entangled state decohered by white noise). The corresponding density matrix reads

$$\rho_{\mathrm{W}} = p \, |\phi^+\rangle \, \langle\phi^+| + \frac{(1-p)}{4} I , \tag{3.51}$$

with $0 \le p \le 1$. They are entangled for $p > 1/3$.

In Fig. 3.9 we present a study of the dependence of C and $I(A:B)$ on the main system parameters. In Fig. 3.9(a) and 3.9(b) we plot concurrence and mutual information, respectively, as a function of the relative orientation between the two PMD vectors $|\eta_1|^2$ and the product of τ_A and pump bandwidth B_p, for $\tau_B = \tau_A$, while keeping the filter bandwidth constant. The dark green area in Fig. 3.9(a) shows combinations of $|\eta_1|^2$ and τ_A for which concurrence drops to zero, and therefore the state is separable. The same points correspond to the dark red area in 3.9(b): for these points, only classical correlations are possible, since $C = 0$. The
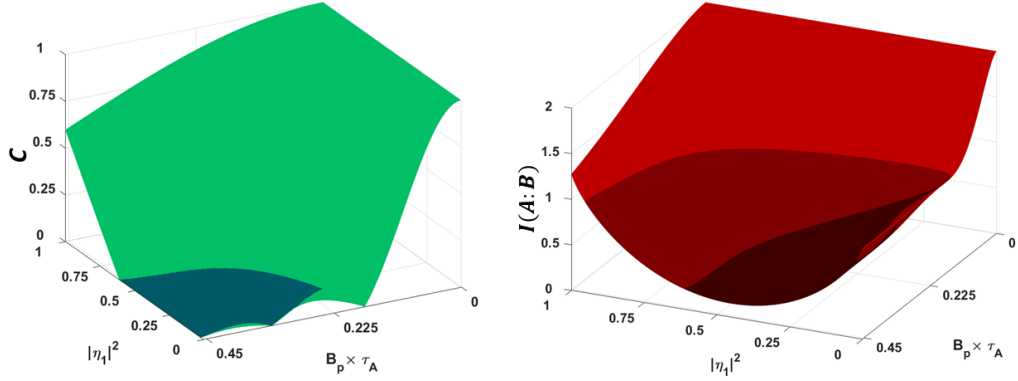
Figure 3.9: Theoretical plots of C (a) and $I(A : B)$ (b) as functions of the relative orientation between the PMD vectors $|\eta_1|^2$ and the product of the DGD in arm A τ_A and the pump bandwidth B_p. The DGDs in the two arms are identical ($\tau_A = \tau_B$) and vary between 0 and 12 ps, while the bandwidth of the pump is kept fixed at 38GHz. The dark green area in (a) shows all those combinations of $|\eta_1|^2$ and τ_A for which the concurrence drops to zero. The same points are presented in (b) in the darker shade of red. The bright red area in (b) represents all the points for which $I(A : B) > 1$.

bright red area in 3.9(b) represents all the points for which $I(A : B) > 1$, for which the presence of quantum correlations is also guaranteed by $C > 0$. In the intermediate region the non-vanishing concurrence implies that the state is entangled, but $I(A : B) < 1$ does not allow one to draw a definite conclusion about the presence of quantum correlations. It is worth to notice that, as expected, the maximum for both C and $I(A : B)$ occurs for $|\eta_1|^2 = 1$, that is, perfect alignment between the two PMD vectors is required to achieve optimal compensation. Figure 3.9 shows also that PMD compensation can only be perfect in the case of continuous-wave pump (or equivalently for $\tau_A = 0$), consistent with previous findings [35, 40], whereas as the product of B_p and τ_A increases, the quality of the compensation deteriorates, even in the case of perfect alignment ($|\eta_1|^2 = 1$). It is worth pointing out that typical PMD values in deployed fiber plants [41] are such that almost complete recovery of concurrence and quantum mutual information can be achieved in practice.

CHAPTER 4

Joint effect of PMD and PDL on polarization-entangled photons

In this chapter we present a study of the effect of the joint presence of PMD and PDL in quantum channel, which represent the main sources of decoherence and modal filtering in fiber-based quantum communications, respectively. As we explained in Chapter 2, the joint presence of PMD and PDL in a channel – whether it's classical or quantum – makes the description very complex. This is why we develop a simple but representative two-element model, and use it to describe the case in which PMD and PDL affect the propagation of one photon in a Bell state, while the second photon is kept in the proximity of the source. We also explore the possibility of performing nonlocal PDL compensation by inserting a controlled PDL element in the path of the second photon, and discuss how the ordering of PMD and PDL in the channel of the first photon yields asymmetrical benefits.

All the sections in this chapter, with the exception of few small parts in Section 4.1, present original work, whose main results are the subject of papers 2 and 3.

4.1   PMD and PDL in the path of photon A

We start by considering the simple case of two lumped elements affecting the propagation of photon A. Even though PMD and PDL are usually distributed along the optical link, in fact, this simple two-element model can be easily reproduced in the channel, and allows one to study the main features of a channel comprising both PMD and PDL in a controlled fashion. Moreover, we will discuss later in the chapter how the model relates to a general polarization quantum channel in which the two effects are distributed.

The generated two-photon state can again be expressed as Eq. (3.10), which we write here again for the case of $\alpha = 0$:

$$|\Psi\rangle = |\tilde{f}(\omega_A, \omega_B)\rangle \otimes \frac{|h_A, h_B\rangle + |v_A, v_B\rangle}{\sqrt{2}}, \tag{4.1}$$

According to the notation introduced in Chapter 2, we denote by $\vec{\gamma}$ the Stokes vector associated with the mode-filtering element, whose effect is described by the operator $\mathbf{T}_0 = \exp(\vec{\gamma} \cdot \vec{\sigma}/2)$, where $\vec{\sigma}$ is again a vector whose elements are the three Pauli matrices, so that $\vec{\gamma} \cdot \vec{\sigma} = \gamma_1 \sigma_1 + \gamma_2 \sigma_2 + \gamma_3 \sigma_3$. With no loss of generality, we assume that the z axis in Stokes space corresponds to the polarization state $|h_A\rangle$ and that $\vec{\gamma}$ is aligned with it, in which case the mode-filtering operator simplifies to the following diagonal form:

$$\mathbf{T}_0 = \begin{pmatrix} e^{\gamma/2} & 0 \\ 0 & e^{-\gamma/2} \end{pmatrix} \tag{4.2}$$

in the $(|h_A\rangle, |h'_A\rangle)$ basis, where $\gamma = |\vec{\gamma}|$. On the other hand, the effect of the PMD element characterized by the Stokes vector $\vec{\tau}$ is described by the operator $\mathbf{U}(\omega) = \exp(-i\omega\vec{\tau} \cdot \vec{\sigma}/2)$ [17], where $|s_A\rangle$ and $|s'_A\rangle$ denote its orthogonal eigenstates, and ω is the offset from the carrier frequency. Note that while the unit of vector $\vec{\tau}$ is that of time, vector $\vec{\gamma}$ is unitless. As we did in Chapter 3, it is useful to express the state in a different basis to make the physical meaning of the problem more apparent and the calculation more straightforward. Again, we pick the polarization basis $(|p_A\rangle, |p'_A\rangle)$, which can be used to re-express the input state as

$$|\psi_{\text{in}}\rangle = |f(t_A, t_B)\rangle \otimes \frac{|p_A p_B\rangle + |p'_A p'_B\rangle}{\sqrt{2}}, \tag{4.3}$$

where by $(|p_B\rangle, |p'_B\rangle)$ we denote an auxiliary orthogonal basis for the polarization of photon B given by $|p_B\rangle = \langle s_A|h_A\rangle |h_B\rangle + \langle p_A|h'_A\rangle |h'_B\rangle$ and $|p'_B\rangle = \langle p'_A|h_A\rangle |h_B\rangle + \langle p'_A|h'_A\rangle |h'_B\rangle$ [39]. We remind the reader that the convenience of this choice arises from the fact that in the basis $(|p_A\rangle, |p'_A\rangle)$, the effect of decoherence simplifies to a relative delay $\tau = |\vec{\tau}|$ between the polarization states $|p_A\rangle$ and $|p'_A\rangle$.

The first channel configuration that we consider is the one in which the PDL element precedes the PMD element (in what follows we refer to this configuration as *PDL-first*). In this case, the output state is obtained by first applying the filtering operator to Eq. (4.1) and then expressing the resulting state in the $(|p_A\rangle, |p'_A\rangle)$ basis prior to applying the PMD operator. This results in the output state

$$\begin{aligned} |\psi_{\text{out}}\rangle = \quad & \frac{\eta}{\sqrt{2}} |f(t_A - \tau/2, t_B)\rangle \otimes (e^{\frac{\gamma}{2}} \langle p_A|h_A\rangle |p_A h_B\rangle + e^{-\frac{\gamma}{2}} \langle p_A|h'_A\rangle |p_A h'_B\rangle) \\ & + \frac{\eta}{\sqrt{2}} |f(t_A + \tau/2, t_B)\rangle \otimes (e^{\frac{\gamma}{2}} \langle p'_A|h_A\rangle |p'_A h_B\rangle + e^{-\frac{\gamma}{2}} \langle p'_A|h'_A\rangle |p'_A h'_B\rangle), \end{aligned}$$

where the normalization coefficient η accounts for the fact that the state is post-selected by coincidence measurement.

In the second channel configuration that we consider, decoherence precedes mode-filtering (in what follows we refer to this configuration as *PMD-first*). In this case, the output state is obtained by first applying the decohering operator to Eq. (4.3) and then expressing the resulting state in the $(|h_A\rangle, |h'_A\rangle)$ basis prior to applying the filtering operator. This results in the state

$$
\begin{aligned}
|\psi_{\text{out}}\rangle = \quad & \frac{\eta}{\sqrt{2}}|f(t_A - \tau/2, t_B)\rangle \otimes (e^{\frac{\gamma}{2}}\langle h_A|p_A\rangle|h_A p_B\rangle + e^{-\frac{\gamma}{2}}\langle h'_A|p_A\rangle|h'_A p_B\rangle) \\
& + \frac{\eta}{\sqrt{2}}|f(t_A + \tau/2, t_B)\rangle \otimes (e^{\frac{\gamma}{2}}\langle h_A|p'_A\rangle|h_A p'_B\rangle + e^{-\frac{\gamma}{2}}\langle h'_A|p'_A\rangle|h'_A p'_B\rangle).
\end{aligned}
$$

The density matrix ρ characterizing the polarization properties of the received state is then obtained in both cases by tracing the full density matrix $|\psi_{\text{out}}\rangle\langle\psi_{\text{out}}|$ over the time modes. To this end, it is convenient to introduce once again the function $R(\tau)$, whose physical meaning was explained in Chapter 3 and whose definition we report here for convenience:

$$
R(\tau) = \int\int d\omega_A d\omega_B |\tilde{f}(\omega_A, \omega_B)|^2 e^{i\omega_A\tau}. \tag{4.4}
$$

Assuming that $\tilde{f}$ is normalized so that $R(0) = 1$, the elements of the resulting density matrix for the *PDL-first* case are

$$
\begin{aligned}
\rho_{11} &= e^{\gamma}|\langle p_A|h_A\rangle|^2\eta^2/2, \ \rho_{22} = e^{-\gamma}|\langle p_A|h'_A\rangle|^2\eta^2/2 \\
\rho_{33} &= e^{\gamma}|\langle p'_A|h_A\rangle|^2\eta^2/2, \ \rho_{44} = e^{-\gamma}|\langle p'_A|h'_A\rangle|^2\eta^2/2 \\
\rho_{12} &= \langle p_A|h_A\rangle\langle p_A|h'_A\rangle^*\eta^2/2 \\
\rho_{13} &= e^{\gamma}R^*(\tau)\langle p_A|h_A\rangle\langle p'_A|h_A\rangle^*\eta^2/2 \\
\rho_{14} &= R^*(\tau)\langle p_A|h_A\rangle\langle p'_A|h'_A\rangle^*\eta^2/2 \\
\rho_{23} &= R^*(\tau)\langle p_A|h'_A\rangle\langle p'_A|h_A\rangle^*\eta^2/2 \\
\rho_{24} &= e^{-\gamma}R^*(\tau)\langle p_A|h'_A\rangle\langle p'_A|h'_A\rangle^*\eta^2/2 \\
\rho_{34} &= \langle p'_A|h_A\rangle\langle p'_A|h'_A\rangle^*\eta^2/2. \tag{4.5}
\end{aligned}
$$

Similarly, for the *PMD-first* case one can show that they become

$$
\begin{aligned}
\rho_{11} &= e^{\gamma}|\langle h_A|p_A\rangle|^2\eta^2/2, \ \ \rho_{22} = e^{\gamma}|\langle h_A|p_A'\rangle|^2\eta^2/2 \\
\rho_{33} &= e^{-\gamma}|\langle h_A'|p_A\rangle|^2\eta^2/2, \ \ \rho_{44} = e^{-\gamma}|\langle h_A'|p_A'\rangle|^2\eta^2/2 \\
\rho_{12} &= e^{\gamma}R^*(\tau)\langle h_A|p_A\rangle\langle h_A|p_A'\rangle^*\eta^2/2 \\
\rho_{13} &= \langle h_A|p_A\rangle\langle h_A'|p_A\rangle^*\eta^2/2 \\
\rho_{14} &= R^*(\tau)\langle h_A|p_A\rangle\langle h_A'|p_A'\rangle^*\eta^2/2 \\
\rho_{23} &= R(\tau)\langle h_A|p_A'\rangle\langle h_A'|p_A\rangle^*\eta^2/2 \\
\rho_{24} &= \langle h_A|p_A'\rangle\langle h_A'|p_A'\rangle^*\eta^2/2 \\
\rho_{34} &= e^{-\gamma}R^*(\tau)\langle h_A'|p_A\rangle\langle h_A'|p_A'\rangle^*\eta^2/2.
\end{aligned}
\tag{4.6}
$$

Note that in the first case, the density matrix is represented in the basis $|p_A h_B\rangle$, $|p_A h_B'\rangle$, $|p_A' h_B\rangle$, $|p_A' h_B'\rangle$, while in the second case it is expressed in the basis $|h_A p_B\rangle$, $|h_A p_B'\rangle$, $|h_A' p_B\rangle$, $|h_A' p_B'\rangle$. Imposing $\mathrm{Tr}(\rho) = 1$ yields in both cases $\eta^2 = 1/\cosh(\gamma)$. As is evident from Eqs. (4.5) and (4.6), the final state exhibits strong dependence on the order of the two elements and orientation of the corresponding eigenstates. Clearly, the only scenario in which the order has no influence on the final state is when the PDL and PMD vectors are aligned. In this specific case, as expected, the received density matrix is the same for both the *PDL-first* and the *PMD-first* configuration, and is given by

$$
\rho = \frac{1}{2\cosh(\gamma)}
\begin{pmatrix}
e^{\gamma} & 0 & 0 & R^{\dagger}(\tau) \\
0 & 0 & 0 & 0 \\
0 & 0 & 0 & 0 \\
R(\tau) & 0 & 0 & e^{-\gamma}.
\end{pmatrix}
\tag{4.7}
$$

To quantify the degree of entanglement of the received state, we use again concurrence, which can be extracted from the corresponding density matrices in the *PDL-first* and *PMD-first* configurations. For the aligned case, described by the density matrix in Eq. (4.7), an analytical expression for concurrence can be obtained pretty easily, and one has

$$
C = \frac{|R(\tau)|}{\cosh(\gamma)}.
\tag{4.8}
$$

For the general case, described by Eqs. (4.5) – (4.6), some cumbersome algebra shows that the concurrence of the received state is again given by the expression in Eq. (4.8). This, quite remarkably, implies that unlike the shape of the state itself, the residual concurrence

is not affected by any channel detail such as the relative orientation of the eigenstates of the two operators, or the order in which the two elements are concatenated. Instead it only depends on the channel's amount of filtering and magnitude of the birefringence vector. Our general result encompasses several previous findings. When decoherence acts alone ($\gamma = 0$), concurrence reduces to $C = |R(\tau)|$, which is the expression demonstrated in [39] and derived again in Chapter III o this work. On the other hand, when decoherence is absent ($\tau = 0$), concurrence is given by $C = 1/\cosh(\gamma)$, as found in [42]. Finally, our result is consistent with the expression for concurrence found in [43], where the effect of mode-filtering on a Bell-diagonal state was studied. In what follows, we will provide a physical interpretation for the independence of concurrence on the order and relative orientation of the decoherence and filtering elements.

PDL preceding PMD. The way in which PDL in the A-optical path affects entanglement is through the probabilities of detecting specific two-photon polarization states (in the post-selected ensemble). If, prior to detection, the analyzer for photon A splits $|h_A\rangle$ and $|h'_A\rangle$, simultaneous clicks will be produced by the two states $|h_A h_B\rangle$ and $|h'_A h'_B\rangle$ only. However, if the analyzer splits a different pair of polarization states, say $|p_A\rangle$ and $|p'_A\rangle$, simultaneous clicks will be produced by the four states, $|p_A h_B\rangle$, $|p'_A h_B\rangle$, $|p_A h'_B\rangle$, and $|p'_A h'_B\rangle$, which emerge when expressing photon A in the basis $(|p_A\rangle, |p'_A\rangle)$. If $|p_A\rangle$ and $|p'_A\rangle$ happen to be aligned with the vector $\boldsymbol{\tau}$ defining a PMD element concatenated to the mode-filtering element, then the temporal waveform associated with each of these four states does not suffer any distortion from decoherence (which simply introduces some delay in each of them); therefore, the corresponding probabilities of simultaneous clicks are not affected. This simple argument shows that the orientation of $\vec{\tau}$ does not interfere with the mechanism through which the preceding PDL element affects the two-photon polarization entanglement.

PMD preceding PDL. As thoroughly discussed in Chapter III, the way in which PMD in the A-optical path reduces entanglement is by correlating photon's A time of arrival with its polarization, so that in principle, one would be able to trace back the two photons' polarization based on their relative times of arrival. This ability is not affected by the presence of a PDL element after PMD in the path of photon A, as filtering does not distort the delayed replicas of the two-photon state waveform, but only the corresponding polarization contents, therefore leaving the arrival times of the two photons unchanged. This clarifies why the orientation of a decoherence element $\vec{\tau}$ preceding a PDL element has no impact on concurrence.

The two arguments illustrated above also imply that the order in which the PMD and PDL elements are concatenated cannot affect the two-photon polarization entanglement. In fact, as all possible relative orientations yield the same concurrence, all cases are equivalent to the one in which the vectors $\vec{\tau}$ and $\vec{\gamma}$ are aligned, and in this special case, the two effects
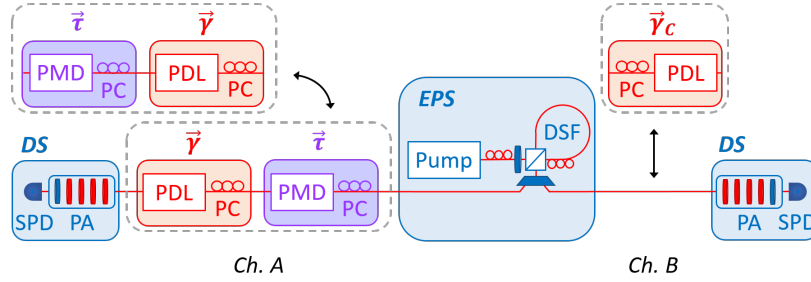
Figure 4.1: Schematic of the experimental apparatus. $\vec{\tau}$: PMD element. $\vec{\gamma}$: PDL element. $\vec{\gamma}_C$: compensating filtering element. EPS: entangled photon source. DSF: dispersion-shifted fiber. PDL: PDL emulator. PMD: PMD emulator which applies a differential group delay $\tau = 6.6$ ps. PC: polarization controller. DS: detector station. PA: polarization analyzer consisting of several waveplates (red) and a polarizer (blue). SPD: single photon detector. The order of the decohering and filtering elements in channel A can be changed to investigate the *PMD-first* and *PDL-first* cases.

commute with each other. Note that while concurrence is insensitive to the details of the two-element channel, the density matrices of the propagated state are not. The consequences of this on the design of a quantum network, such as choosing a direction in which the channel is to be used, will be discussed later in this Chapter.

4.1.1 Experiment

In order to provide experimental evidence of the findings discussed in the previous section, we consider two different settings for both the *PDL-first* and *PMD-first* configurations; one in which $\vec{\tau}$ and $\vec{\gamma}$ are aligned, and another in which they are orthogonal to each other in Stokes space (or equivalently they form an angle of 45 degrees in Jones space). Our experimental setup consists of an entangled–photon source (EPS), telecom optical fibers, and two separate detector stations [44] that include polarization analyzers (PA) and InGaAs single photon detectors, which are used to perform state tomography [45]. In order to introduce controllable PMD and PDL in the channel, we use PMD and PDL emulators, respectively. Both devices are produced by OZ Optics (refer to [46] for the complete data sheet of the product). The PDL emulators, which are fully configurable both in magnitude (within the 0 dB - 7 dB range) and orientation, can be inserted in the paths of the two photons. All of the PDL emulators are PMD-free, except for one that has a fixed differential group delay; we use the latter to reproduce the effect of lumped PMD.

The entangled photons are generated inside the EPS by pumping a dispersion-shifted fiber (DSF) with a 50 MHz pulsed fiber laser that operates at 193.1 THz and creates signal and idler photons via four-wave mixing [47]. The average number of generated photon pairs per

pulse can be tuned in the $0.001 - 0.1$ range [48, 49]. The generated photons are spectrally separated and routed to channels on the 100 GHz-spaced ITU grid [50]. For this specific experiment, we use channels 28 (192.8 THz) and 34 (193.4 THz). The resulting photon temporal wavefunctions are of a sinc-like shape with temporal FWHM of about 15 ps.

The detector stations (DS) each include one gated single photon detector (SPD) with a detection efficiency of $\eta \sim 20\%$ and a dark count probability of $\sim 4 \times 10^{-5}$ per gate, as well as a polarization analyzer (PA) which allows for measurements at any angle on the Bloch sphere. FPGA-based controller software automatically controls the detectors and analyzers in order to perform full polarization state tomography by performing 36 different measurements [1]. Each of the 36 measurements is performed over 50 million detector gates, resulting in several thousands of detected coincidences per measurement depending on the experimental parameters. The density matrix is then reconstructed using a maximum likelihood estimation algorithm [45].

A relevant value of the fixed DGD of 6.6 ps was chosen to introduce a non-negligible entanglement reduction, corresponding to a concurrence of $C = 0.66$ in the absence of PDL. A schematic of the experimental setup is shown in Fig. 4.1. The order of decoherence and modal filtering, as well as the relative orientation of $\vec{\tau}$ and $\vec{\gamma}$, can be varied to cover all of the possible configurations by adjusting the PMD and PDL emulators.

First, we experimentally confirm Eqs. (4.5, 4.6) in four specific cases. We introduce both a PDL and a PMD emulator in the channel of photon A and vary the emulators' order and orientation. That is, by using polarization controllers, we can either align vectors $\vec{\tau}$ and $\vec{\gamma}$ or make them orthogonal. The left column of Fig. 4.2 shows the matrices expressed by Eqs. (4.5, 4.6). The right column presents experimentally measured matrices in the same four scenarios. The two columns show striking similarities, thus verifying our theoretical calculations. Minor variations due to experimental noise are slightly noticeable in the zero-valued elements of the experimental matrices. The matrices in the top two rows, expressed in the basis $|p_A h_B\rangle$, $|p_A h'_B\rangle$, $|p'_A h_B\rangle$, $|p'_A h'_B\rangle$, correspond to the *filtering-first* scenario. Similarly, the bottom two rows of matrices refer to the *decoherence-first* configuration and are expressed in the basis $|h_A p_B\rangle$, $|h_A p'_B\rangle$, $|h'_A p_B\rangle$, $|h'_A p'_B\rangle$. The vectors $\boldsymbol{\tau}$ and $\boldsymbol{\gamma}$ are aligned for (a,c,e,g) and are orthogonal for (b,d,f,h). The four specific cases are color-coded in Fig. 2, and the same color coding is adopted throughout the rest of the Section. The figure clearly shows that the orientation and ordering of the decohering and filtering elements affect the final quantum state as seen in the different density matrices.

─────────────────────────────

[1]Full state tomography of two qubits is achievable from the statistics of only 9 measurement settings if two detectors are used per photon [45]. However, for convenience we use a single detector per photon and take 36 total measurements, corresponding to all pairwise combinations of both eigenstates of each Pauli operator.
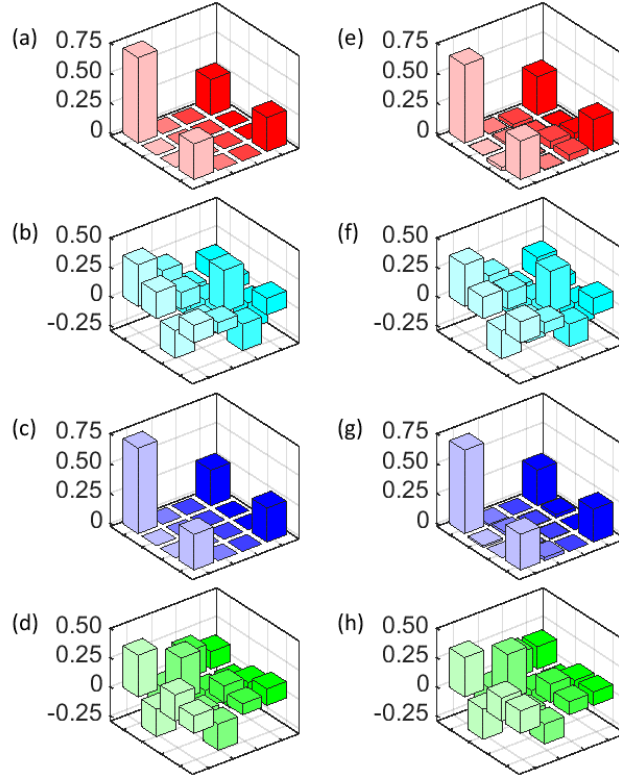
Figure 4.2: Theoretical (left) and experimental (right) representation of Eqs.(4.5)-(4.6), for the case where the eigenvectors of the PDL and PMD elements are aligned ((a)-(e) and (c)-(g)) and orthogonal ((b)-(f) and (d)-(h)) in Stokes space. The matrices in the top two rows ((a)-(b)-(e)-(f)) refer to the *PDL-first* scenario and are expressed in the basis $|p_A h_B\rangle$, $|p_A h'_B\rangle$, $|p'_A h_B\rangle$, $|p'_A h'_B\rangle$. The matrices in the bottom two rows ((c)-(g)-(d)-(h)) refer to the *PMD-first* scenario and are expressed in the basis $|h_A p_B\rangle$, $|h_A p'_B\rangle$, $|h'_A p_B\rangle$, $|h'_A p'_B\rangle$. The magnitude fo the PDL vector is $\gamma = 0.46$ for all matrices.

Next, we validate the theoretical expression Eq. (4.8), that is plotted in Fig. 4.3 with a dashed line. The symbols show the experimental concurrence as a function of the amount of PDL γ in the channel. The squares refer to the *PDL-first* configuration, and the circles refer to the *PMD-first* scenario; empty and filled markers are used for the aligned and orthogonal configuration, respectively. All the data points are in excellent agreement with the theoretical curve. The plot confirms that the amount of entanglement is determined only by the magnitude of PMD and PDL and, contrary to the states themselves, is independent of either order or relative orientation.

Now we turn our attention to the ordering of the decohering and filtering elements, which is important in fiber channels for various reasons. A particularly illustrative case is the one with the decohering and filtering elements $\vec{\tau}$ and $\vec{\gamma}$ being orthogonal in Stokes space.
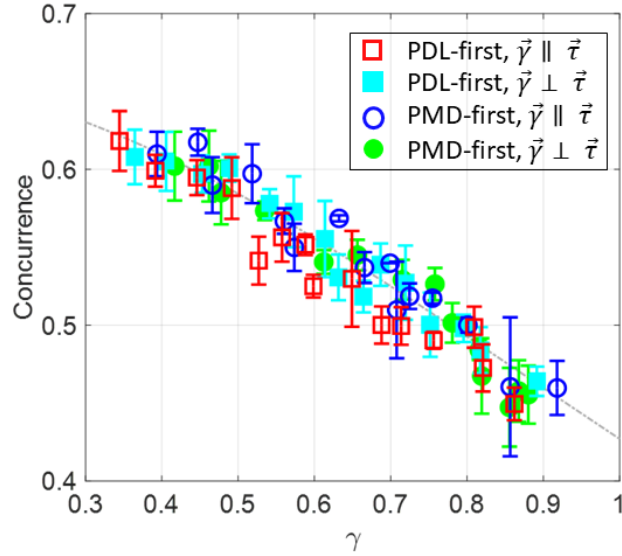
Figure 4.3: Concurrence as a function of the amount of PDL γ in the channel. The dashed line represents the theoretical result Eq. (4.8). All of the markers are experimental points: squares refer to the *PDL-first* scenario, while circles refer to the *PMD-first* scenario. In both cases, the empty markers correspond to the case in which the $\vec{\gamma}$ is aligned with $\vec{\tau}$, and the filled ones to the case in which they are orthogonal.

Indeed in this case, if photon A is expressed in the basis (h_A, h_A'), and photon B in the basis (h_B, h_B'), the density matrix simplifies to

$$\rho_i = \frac{1}{4\cosh(\gamma)} \begin{pmatrix} e^{\gamma}(1+R(\tau)) & 0 & 0 & 1+R(\tau) \\ 0 & e^{\xi_i \gamma}(1-R(\tau)) & 1-R(\tau) & 0 \\ 0 & 1-R^*(\tau) & e^{-\xi_i \gamma}(1-R(\tau)) & 0 \\ 1+R^*(\tau) & 0 & 0 & e^{-\gamma}(1+R(\tau)) \end{pmatrix}, \quad (4.9)$$

where $i = 1$ and $i = 2$ correspond to the *PMD-first* and *PDL-first* scenarios, respectively, and $\xi_1 = -\xi_2 = 1$. In this particularly illustrative situation, the two expressions can be obtained from each other by simply permutating the elements ρ_{22} and ρ_{33}. An experimental verification of this formula is presented in Fig. 4.4. The left panel shows experimental density matrices related to the two scenarios for $\gamma = 0.41, 0.66, 0.77$; the right panel shows a plot of the experimentally obtained coincidence probabilities given by the diagonal elements of ρ_i versus γ, with the four curves showing the corresponding theoretical expressions from Eq. (4.9). Consistent with the theory, one can see that as PDL in the channel is increased, $\rho_{i,11}$
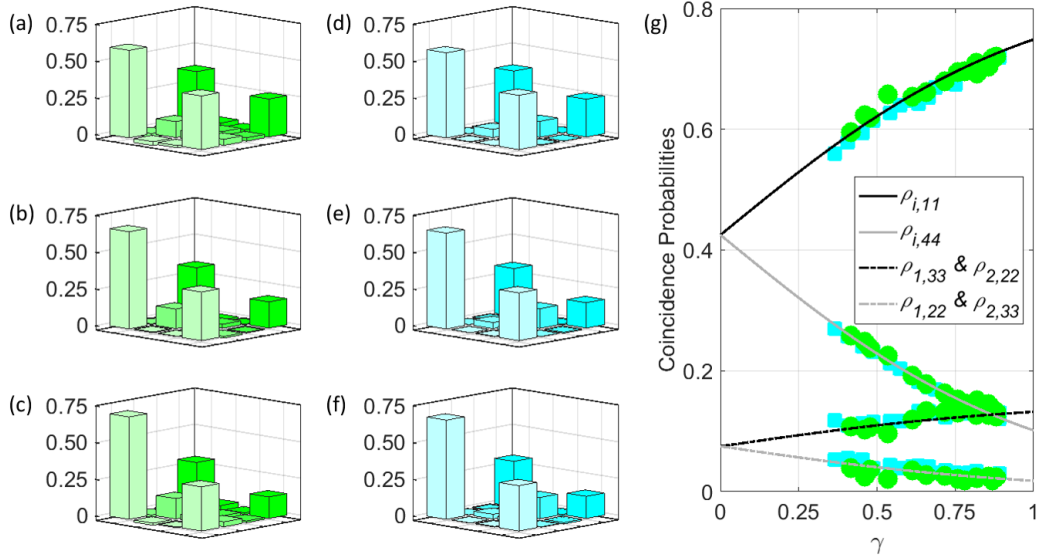
Figure 4.4: Experimental results of the setup reproducing Eq. (4.9) for the *PMD-first* (green) and *PDL-first* (cyan) cases when τ and γ are orthogonal in Stokes space. Left panel: experimental density matrices expressed in the basis $|h_A h_B\rangle$, $|h_A h'_B\rangle$, $|h'_A h_B\rangle$, $|h'_A h'_B\rangle$, for $\gamma = 0.41$ (a, d), 0.66 (b, e), and 0.77 (c, f). Right panel: coincidence probabilities, measured via the diagonal elements of the density matrix, as a function of γ. Comparison of $\rho_{i,11}$, $\rho_{i,22}$, $\rho_{i,33}$, and $\rho_{i,44}$, where $i = 1, 2$ for the *filtering-first* and *decoherence-first* cases, respectively. $\rho_{i,11}$ and $\rho_{i,44}$ are independent of the ordering of the two effects; however, $\rho_{1,22}$ is equivalent to $\rho_{2,33}$, and vice-versa.

increases and $\rho_{i,44}$ decreases, both in the *PDL-first* case (cyan markers), and in the *PMD-first* scenario (green markers). On the other hand, in the *PDL-first* case, $\rho_{i,22}$ decreases with γ, and $\rho_{i,33}$ increases with it, whereas the opposite behaviour is observed in the *PMD-first* scenario.

Our analysis shows that this simple difference between the two cases provides a powerful tool to gain information about the channel in which the photon is propagating when vector $\vec{\tau}$ and $\vec{\gamma}$ are orthogonal in Stokes space. By simply measuring ρ_{22} and ρ_{33}, that is by recording only coincidence counts along (h_A, h'_B) and (h'_A, h_B) instead of reconstructing the whole density matrix, one can in fact tell whether modal loss or decoherence comes first. Note that ρ_{22} and ρ_{33} are indicative of the quantum bit error ratio (QBER), and nearly all quantum protocols monitor QBER on a regular basis.

4.2   Relation to a general fiber-optic channel

In this section, we expand our treatment of a bi-photon quantum state, one photon of which is distributed over an optical fiber, to include a more general channel model. In the previous Section, the channel was represented by two lumped elements, the order and relative orientation of which we have carefully examined. As thoroughly discussed in Chapter 2, installed fibers are naturally more complex because the optical path is long and perturbations that cause decoherence and mode filtering in the form of PMD and PDL, respectively, are local in nature, numerous, and occur throughout the length of the route (see also [51–56]).

Since PMD and PDL originate from spatially distributed sources, their effect is not simply that of two lumped sources; instead, they add in a rather complex fashion. However, their joint effect on a sufficiently narrow-band signal can be described by the following frequency-dependent transfer matrix [34]:

$$\mathbf{T}(\omega) = \exp\left(-\frac{i}{2}\omega\tilde{\tau}\cdot\vec{\sigma}\right)\mathbf{T}_0, \tag{4.10}$$

where $\mathbf{T}_0$ is the transfer matrix at $\omega = 0$ and can be assumed to be in the diagonal form of Eq. (4.2) with no loss of generality. The symbol $\tilde{\tau}$ denotes a three-dimensional vector. When $\tilde{\tau}$ is real-valued, the operator $\mathbf{T}(\omega)$ is simply the product of a PMD operator and a PDL operator, whose effect on the photon pair we studied in depth. On the other hand, by letting the components of $\tilde{\tau}$ be complex-valued, Eq. (4.10) describes the most general polarization channel instantiation. In this case, the imaginary component of $\tilde{\tau}$ is responsible for the presence of frequency-dependent PDL, which has non-trivial implications in terms of waveform distortion [34].

If photon A of the polarization-entangled state in Eq. (4.1) propagates in a fiber link described by Eq. (4.10), and photon B does not suffer any propagation effects, the received two-photon state can be expressed as

$$|\psi_{\text{out}}\rangle = \eta \int \int d\omega_A d\omega_B \tilde{f}(\omega_A, \omega_B)|\omega_A, \omega_B\rangle \otimes \frac{|\mathbf{T}(\omega_A)h_A, h_B\rangle + |\mathbf{T}(\omega_A)h'_A, h'_B\rangle}{\sqrt{2}},$$

where the coefficient η ensures that the output state is correctly normalized after post-selection. The density matrix ρ characterizing the polarization properties of the received state is then obtained by tracing the full density matrix $|\psi_{\text{out}}\rangle\langle\psi_{\text{out}}|$ over the frequency modes:

$$\rho_{ij} = \frac{\eta^2}{2} \int \int d\omega_A d\omega_B |f(\omega_A, \omega_B)|^2 T_{n_i,m_i}(\omega_A) T^*_{n_j,m_j}(\omega_A), \tag{4.11}$$

where T_{n_i,m_j} denotes the element (n_i, m_j) of $\mathbf{T}$, with $n_1 = n_2 = 1$, $n_3 = n_4 = 2$, $m_1 = m_3 = 1$,

and $m_2 = m_4 = 2$, whose computation is more convenient using the following expansion:

$$\exp\left(\frac{i}{2}\omega\tilde{\tau}\cdot\vec{\sigma}\right) = \cos\left(\frac{\omega\sqrt{\tilde{\tau}\cdot\tilde{\tau}}}{2}\right)\mathbb{I} - i\frac{\tilde{\tau}\cdot\vec{\sigma}}{\tilde{\tau}}\sin\left(\frac{\omega\sqrt{\tilde{\tau}\cdot\tilde{\tau}}}{2}\right). \tag{4.12}$$

Since the simple analytical two-element model of Eqs. (4.5, 4.6) must be a particular case of the general channel description of Eq. (4.11), we begin by finding the constraints that reduce the latter to the former. Clearly, a real-valued vector $\tilde{\tau}$, such that $\tilde{\tau} = \tau$, reduces the general channel to the *PDL-first* configuration. On the other hand, the constraints for the *PMD-first* configuration are a bit more involved. This configuration is characterized by the transfer matrix

$$\mathbf{T}(\omega) = \mathbf{T}_0\exp\left(-\frac{i}{2}\omega\vec{\tau}\cdot\vec{\sigma}\right) = \exp\left(-\frac{i}{2}\omega\tilde{\tau}\cdot\vec{\sigma}\right)\mathbf{T}_0, {}^2 \tag{4.13}$$

where the second equality implies the identity $\tilde{\tau}\cdot\vec{\sigma} = \mathbf{T}_0\vec{\tau}\cdot\vec{\sigma}\mathbf{T}_0^{-1}$, which yields

$$\tilde{\tau}_1 = \tau_1 \tag{4.14}$$
$$\tilde{\tau}_2 = \cosh(\gamma)\tau_2 - i\sinh(\gamma)\tau_3 \tag{4.15}$$
$$\tilde{\tau}_3 = \cosh(\gamma)\tau_3 + i\sinh(\gamma)\tau_2. \tag{4.16}$$

Inspection of Eqs. (4.14–4.16) shows that the real and imaginary components of the complex vector $\tilde{\tau}$, which we denote by $\tilde{\tau}_R$ and $\tilde{\tau}_I$, respectively (so that $\tilde{\tau} = \tilde{\tau}_R + i\tilde{\tau}_I$), are orthogonal to each other. This constitutes the most relevant feature of the manifold of complex vectors $\tilde{\tau}$ spanned by the *PMD-first* configuration.

Another, less restrictive, implication of Eqs. (4.14–4.16) is that the square length of the real component of $\tilde{\tau}$ exceeds that of its imaginary component by the square length of $\vec{\tau}$, namely by the square differential group delay of the corresponding PDL-free link ($|\tilde{\tau}_R|^2 - |\tilde{\tau}_I|^2 = \tau^2$). Both of these relations emerge *on average* in all fiber-optic links [34], including space-division multiplexed transmission links based on multi-core and multi-mode fibers [57], where the complex vector $\tilde{\tau}$ is a random quantity. In particular, denoting by $\mathbb{E}$ ensemble averaging, the analogue of the first relation is $\mathbb{E}[\tilde{\tau}_R \cdot \tilde{\tau}_I] = 0$, while the analogue of the second is $\mathbb{E}[|\tilde{\tau}_R|^2] - \mathbb{E}[|\tilde{\tau}_I|^2] = \mathbb{E}[\tau^2]$, where $\mathbb{E}[\tau^2]$ is intended to be the mean-square DGD that would accumulate in the link if PDL were absent. The latter relation does not ensure that the inequality $|\tilde{\tau}_R| \geq |\tilde{\tau}_I|$ is always fulfilled, but it does imply that its violation occurs with low

---

[2]Notice that the T_0 operator in the central and right-most hand side of the equation have to be the same to ensure that the the equation is still valid for $\omega = 0$.
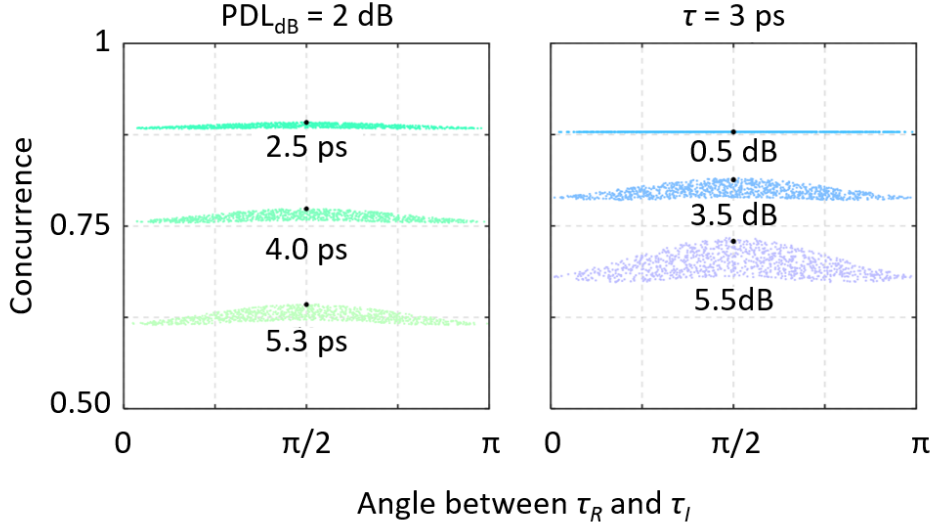
Figure 4.5: Concurrence as a function of the angle formed by the real and imaginary parts of the complex-valued vector $\tilde{\tau} = \tilde{\tau}_R + i\tilde{\tau}_I$. The larger black dots refer to the *PMD-first* configuration, where the vector $\tilde{\tau}$ is given by Eqs. (4.14–4.16), while the smaller dots were obtained by randomly varying the orientation of the real and imaginary parts of the same vector.

probability. This primarily occurs for unrealistically large PDL values [34], which makes it of little relevance. Finally, it is worth noting that even if $|\tilde{\tau}_R| \geq |\tau_I|$, Eqs. (4.14–4.16) do not ensure that any arbitrary value of $|\tilde{\tau}_R|$ and $|\tilde{\tau}_I|$ can be matched. Indeed, for a given instance of $|\tilde{\tau}_R|$ and $|\tilde{\tau}_I|$, the values of τ_1, τ_2, and τ_3 must satisfy the relation

$$\frac{\tau_2^2 + \tau_3^2}{\tau_1^2 + \tau_2^2 + \tau_3^2} = \frac{1}{(|\tilde{\tau}_R|^2/|\tilde{\tau}_I|^2 - 1)\sinh^2(\gamma)} \leq 1, \tag{4.17}$$

where $\tau_1^2 + \tau_2^2 + \tau_3^2 = \tau^2 = |\tilde{\tau}_R|^2 - |\tilde{\tau}_I|^2$, and where γ is dictated by $\mathbf{T}_0$. Clearly, specific combinations of values of $|\tilde{\tau}_R|$, $|\tilde{\tau}_I|$, and γ can violate the inequality in Eq. (4.17).

As an aside, this limitation disappears in a lumped element channel with an additional PDL element, so that the three-element channel is $\mathbf{T}_1 \exp(i\omega\vec{\tau} \cdot \vec{\sigma}/2)\mathbf{T}_2 = \exp(i\omega\tilde{\tau} \cdot \vec{\sigma}/2)\mathbf{T}_1\mathbf{T}_2$, with $\mathbf{T}_1\mathbf{T}_2 = \mathbf{T}_0$. Here, the coefficient γ_1 of $\mathbf{T}_1$ provides an additional degree of freedom in Eq. (4.17), which decouples the problem of matching $|\tilde{\tau}_R|$ and $|\tilde{\tau}_I|$ from that of matching $\mathbf{T}_0$.

In what follows, we compare the simple two-element channel model we proposed in Sec. 4.1 to the most general polarization channel. We argue that while the latter precisely reproduces the real channel, the former captures its main characteristics and accurately

describes the way in which a general polarization channel affects the degree of entanglement of a photon-pair over a pertinent range of the channel parameters. To this end, we investigate the effect of the relative orientation of $\tilde{\tau}_R$ and $\tilde{\tau}_I$ on the degree of entanglement of the received two-photon state. For a meaningful comparison, we start from the *decoherence-first* configuration of Eq. (4.13), with some fixed value of γ and τ (as discussed in Sect. 4.1, the orientation of the PMD vector $\vec{\tau}$ is immaterial in this context, since it doesn't affect the residual concurrence of the received two-photon state). We then evaluate the corresponding complex vector $\tilde{\tau}$ according to Eqs. (4.14–4.16) and randomly vary the orientation of its real and imaginary components while keeping their lengths fixed. For each combination of $\tilde{\tau}_R$ and $\tilde{\tau}_I$ we evaluate the reduced density matrix ρ of the propagated two-photon state and extract the corresponding concurrence C.

The results are shown in Fig. 4.5, where concurrence is plotted as a function of the angle formed by the real and imaginary components of $\tilde{\tau}$. The data points in the left panel were obtained for the displayed values of the DGD τ and for $\gamma = 0.23$, which corresponds to a PDL value in decibel [3] of $\mathrm{PDL_{dB}} = 2$ dB. The data points in the right panel were obtained for values of γ corresponding to the displayed values of $\mathrm{PDL_{dB}}$ and for a DGD of 3 ps. In this example, we assume a super-Gaussian profile of third order for both the pump power spectrum $|\tilde{E}_p(\omega)|^2$ and the filters' transmittivities $|H_{A,B}(\omega)|^2$. For the former, we use a 3-dB bandwidth of 50 GHz, while for the latter, we use a 3-dB bandwidth of 100 GHz. The figure shows that varying the orientation of $\tilde{\tau}_R$ and $\tilde{\tau}_I$ produces some scattering of the measured concurrence below the *PMD-first* configuration value, which is shown with the bigger dot. Extensive simulations show that this scattering is mostly affected by the magnitude of PDL, but it remains almost negligible for PDL and DGD values of practical relevance. Therefore, the *PMD-first* case serves as a reliable tool for assessing entanglement degradation over a general channel.

As a final remark, we note the symmetry between the *PMD-first* and *PDL-first* scenarios. Indeed, Eq. (4.10) could be easily rearranged in the following form:

$$\mathbf{T}(\omega) = \exp\left(-\frac{i}{2}\omega\tilde{\tau}\cdot\vec{\sigma}\right)\mathbf{T}_0 = \mathbf{T}_0\exp\left(-\frac{i}{2}\omega\tilde{\tau}'\cdot\vec{\sigma}\right), \qquad (4.18)$$

where the complex-valued vector $\tilde{\tau}'$ is defined through the relation $\tilde{\tau}'\cdot\vec{\sigma} = \boldsymbol{T}_0^{-1}(\tilde{\tau}'\cdot\vec{\sigma})\boldsymbol{T}_0$. For the general channel, the constraints on the complex-valued vector $\tilde{\tau}$ will reverse between the *PDL-first* and *PMD-first* configurations. Correspondingly, our modelling results then reflect the *PDL-first* scenario. Hence, the two configurations are equally capable of emulating a

---

[3]We remind the reader that, as discussed in Chapter II, the quantity $\mathrm{PDL_{dB}}$ is defined as the power ratio, in decibel, between the least and most attenuated polarization states, which yields $\mathrm{PDL_{dB}} = 20\log_{10}(\mathrm{e})\,\gamma$.

general fiber-optic channel.

4.3 Infer the relative orientation of PMD and PDL

In this section we describe a procedure that can be of great relevance in an experimental setup to study the effect of PMD and PDL on entangled photons. We have shown in the last few sections how an important parameter in certain configurations is the relative orientation of the PMD and PDL vectors. Here we suggest a way to keep track of this figure from quantities that are basis-independent and that can be easily extracted from the polarization density matrix of the received two-photon state.

Consider once again one photon of a polarization-entagled pair propagating through a channel with PMD and PDL. We focus on the *PDL-first* case for the moment. Keeping in mind that the mutual information $S(A : B)$ is related to the von Neumann entropies of the complete and reduced density matrices as follows

$$S(A : B) = S(A) + S(B) - S(AB), \tag{4.19}$$

we start off by obtaining some analytical expressions for the extreme cases – i.e. PDL ad PMD vectors aligned and orthogonal on the Bloch sphere – that are useful in what follows.

4.3.1 PDL and PMD are aligned

If the two elements are aligned, the output state is described by the density matrix in Eq. (4.46), whose eigenvalues are equal to

$$\lambda_{1,2} = \frac{1 \pm \sqrt{1 - \frac{1 - R^2(\tau)}{\cosh^2(\gamma)}}}{2}. \tag{4.20}$$

The reduced density matrices for photon A and B are both equal to

$$\rho_A = \rho_B = \frac{1}{2\cosh(\gamma)} \begin{pmatrix} e^\gamma & 0 \\ 0 & e^{-\gamma} \end{pmatrix}, \tag{4.21}$$

which doesn't depend on the amount of PMD in the channel. The quantum mutual information in Eq. (4.19) can then be analytically expressed as

$$S(A : B) = 2 + 2\log_2[\cosh(\gamma)] - 2\gamma \log_2(e)\tanh(\gamma) - \sum_{i=1}^{2} \lambda_i \log_2(\lambda_i). \tag{4.22}$$

4.3.2 PDL and PMD are orthogonal

If the two elements are orthogonal on the Bloch sphere, then the output state is described by the density matrix in Eq. (4.9), with $i = 1$. The eigenvalues are given by

$$\kappa_{1,2} = \frac{1 \pm |R(\tau)|}{2},$$

which do not depend on the amount of PDL in the channel and are the same as in the case of PMD only. The reduced density matrices become

$$\rho_A = \frac{1}{2} \begin{pmatrix} 1 + R(\tau) \tanh(\gamma) & 0 \\ 0 & 1 - R(\tau) \tanh(\gamma) \end{pmatrix}$$

and

$$\rho_B = \frac{1}{2 \cosh(\gamma)} \begin{pmatrix} e^\gamma & 0 \\ 0 & e^{-\gamma} \end{pmatrix}, \tag{4.23}$$

respectively. The partial density matrix ρ_B is thus the same as in the case in which PMD and PDL are aligned; this result is actually more general, and does not apply to these two cases only: regardless of the relative alignment of the PMD and PDL vectors, ρ_B will always be given by Eq. (4.23). The reduced density matrix corresponding to subsystem A, on the other hand, is orientation-dependent.

The von Neumann entropy of the reduced density matrices can thus be written as

$$S(\rho_A) = 1 + \frac{1}{2} R(\tau) \tanh(\gamma) \log_2 \left(\frac{1 - R(\tau) \tanh(\gamma)}{1 + R(\tau) \tanh(\gamma)} \right) - \frac{1}{2} \log_2 \left(1 - R^2(\tau) \tanh^2(\gamma) \right), \tag{4.24}$$

and

$$S(\rho_B) = 1 + \log_2 [\cosh(\gamma)] - \gamma \log_2(e) \tanh(\gamma). \tag{4.25}$$

The von Neumann entropy of the two-photon state is given by

$$S(\rho) = -\kappa_B \log_2(\kappa_B) - \kappa_B \log_2(\kappa_B) \tag{4.26}$$

which does not depend on PDL.

4.3.3 General case

The relations obtained in the previous sections allow one to gain resourceful information about the relative orientation of the PDL and PMD vectors, based on quantities that can
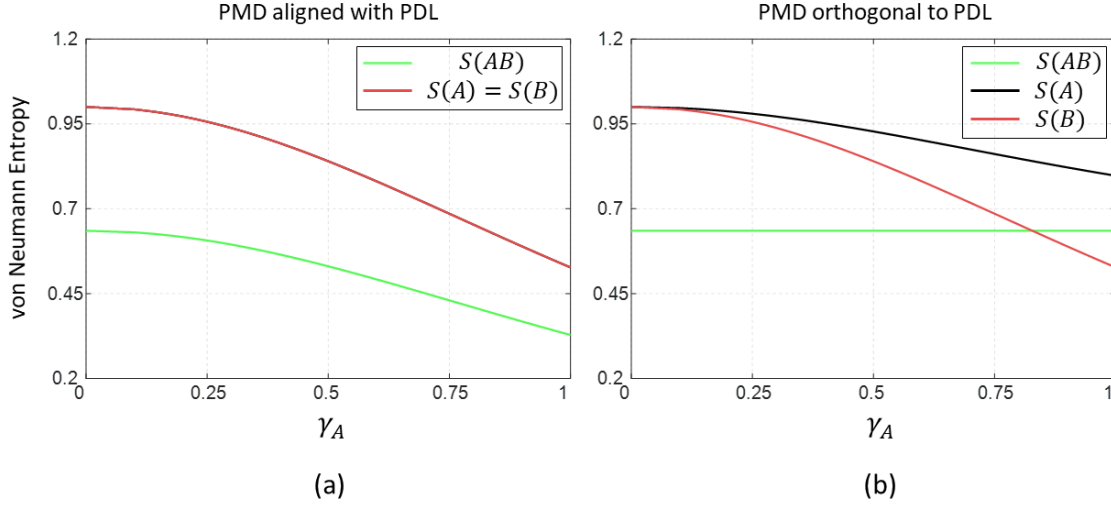
Figure 4.6: Theoretical plots for the von Neumann entropy of the complete density matrix ρ_{AB} and the reduced density matrices ρ_A and ρ_B as functions of the amount of PDL in the channel γ. In (a) we show the case in which the PMD and PDL vectors are aligned on the Bloch sphere, while in (b) the case in which they are orthogonal is presented.

be evaluated starting from the density matrix describing the polarization of the photons. The idea is to make use of quantities that depend on the relative orientation of the PMD and PDL vectors - and, ideally, on nothing else. Concurrence is not a good candidate, since it only depends on the amount of PMD and PDL in the channel, and not on their relative orientation. The von Neumann entropies of the reduced density matrices ρ_A and ρ_B, on the other hand, seem to serve well our purpose. By inspecting Fig. 4.6 in which the extreme cases of PMD and PDL vectors being aligned (a) and orthogonal (b) are presented, one can notice how in the case of perfect alignment they have the same value, regardless of the amount of PDL in the channel. The difference between the two quantities, on the other hand, increases with γ when the PDL and PMD vectors are orthogonal on the Bloch sphere, as evident from Fig. 4.6(b). In all the other situations, the difference between $S(\rho_A)$ and $S(\rho_B)$ will fall between the two cases we have just shown, and the quantity $S(\rho_A) - S(\rho_B)$ can thus be used to infer the relative angle between the PDL and PMD vectors, as we show later in this section. Also notice that the von Neumann entropy of ρ_B does not depend on the PMD in the channel, while that of ρ_A does. Since the divergence of the latter curve from the former obviously arises from the presence of PMD in the channel, the bigger the DGD,

the easier the discrimination between the curves.

A great advantage of this approach arises from the fact that all the quantities that one needs to measure do not depend on the basis in which the measurement takes place (von Neumann entropy doesn't vary under local rotations). Another intriguing feature of this technique is that if we are only interested in checking whether the PDL and PMD vectors are aligned or not, it will suffice to measure the von Neumann entropies of the reduced density matrices ρ_A and ρ_B and make sure that these two quantities are equal, since this only occurs in the case of perfect alignment. This can be done even if one does not know the exact amount of PDL in the channel, which makes it particularly useful in practical situations. Moreover, if the user does not know the amount of PDL in the channel, he can actually obtain it by measuring the von Neumann entropy of ρ_B and using Eq.(4.25), by exploiting the fact that $S(\rho_B)$ only depends on the PDL in the channel, and not on its relative orientation with the PMD vector. Actually, one only needs to evaluate either one of the two eigenvalues of ρ_B, since from (4.23) it follows

$$\gamma = \pm\frac{1}{2}\ln\left(\frac{1}{\mu_i}-1\right), \tag{4.27}$$

where $\mu_{1,2}$ are the eignevalues of ρ_B sorted in ascending order.

If one is interested in learning the angle between the PDL and PMD vectors, they can act as follows. Starting from the complete density matrix of the PDL-firt scenario (Eq. (4.5)) and tracing out the polarization of photon B we get:

$$\rho_A = \frac{1}{2\cosh(\gamma)}\begin{pmatrix} e^{\gamma}|\alpha|^2 + e^{-\gamma}|\beta|^2 & -2R^*(\tau)\alpha^*\beta^* \\ -2R(\tau)\alpha\beta & e^{\gamma}|\beta|^2 + e^{-\gamma}|\alpha|^2 \end{pmatrix} \tag{4.28}$$

where $|h_A\rangle = (1 \quad 0)^T$, $|h'_A\rangle = (0 \quad 1)^T$, $|p_A\rangle = (\alpha \quad \beta)^T$, $|p'_A\rangle = (-\beta^* \quad \alpha^*)^T$, so that $\langle p_A|h_A\rangle = \alpha^*$, $\langle p_A|h'_A\rangle = \beta^*$, $\langle p'_A|h_A\rangle = -\beta$, $\langle p'_A|h'_A\rangle = \alpha$. The absolute values of α and β are obviously related through $|\alpha|^2 + |\beta|^2 = 1$. The eigenvalues of ρ_A read

$$\mu_{1,2} = \frac{1}{2} \pm \frac{1}{2}\sqrt{1 - \frac{1}{\cosh^2\gamma} - (1-|R(\tau)|^2)|\alpha|^2(1-|\alpha|^2)\tanh^2\gamma}, \tag{4.29}$$

or

$$\mu_{1,2} = \frac{1}{2} \pm \frac{1}{2}\sqrt{1 - \frac{1}{\cosh^2\gamma} - (1-|R(\tau)|^2)\sin^2(2\theta)\tanh^2\gamma}, \tag{4.30}$$

where we have introduced the angle θ between the PMD and PDL vectors such that

$|\langle h_A|p_A\rangle|^2 = |\alpha|^2 = \cos^2(\theta)$. This leads to an expression for the relative angle in terms of either one of the eigenvalues of ρ_A:

$$\theta = \frac{1}{2}\arcsin\left(\sqrt{\frac{1 - \frac{1}{\cosh^2\gamma} - 4\left(\mu - \frac{1}{2}\right)^2}{(1 - |R(\tau)|^2)\tanh^2\gamma}}\right). \tag{4.31}$$

To summarize our results, we suggest the following algorithm to evaluate the relative angle between the PDL and PMD vectors starting from the density matrix of the two-photon state:

1. Measure the density matrix of the two-photon state;

2. Trace over photon A to evaluate ρ_B and its eigenvalues/von Neumann entropy;

3. Evaluate γ using Eq.(4.27);

4. Trace over photon B to evaluate ρ_A and its eigenvalues/von Neumann entropy;

5. If one is only interested in knowing if the PMD and PDL vectors are aligned, they just need to check if $S(\rho_A) = S(\rho_B)$, and if this is not the case, adjust the polarization controller accordingly;

6. If one is interested in evaluating the exact angle between the PDL and PMD vectors, they can use Eq.(4.31).

4.4   PDL in both arms

We now expand our our model to include a second PDL element, which affects the propagation of photon B. In this scenario, the mathematical description becomes quite more involved, and leads to some interesting features. In particular, the order of the PMD and PDL elements in the path of photon A becomes crucial, since it has tangible consequences that are discussed in the following.

4.4.1   *PDL-first* in the path of photon A

We start by describing the case in which the PDL element precedes the PMD element in the path of photon A. Since we now have a second PDL element (which this time affects the propagation of photon B) we need to slightly change the notation for the PDL vectors, which are now denoted as $\vec{\gamma}_A$ and $\vec{\gamma}_B$.

In this scenario, it is useful to express the state in Eq. (3.10) in the basis of the PDL eigenstates $\{|u_i\rangle, |u_i'\rangle\}$, where $i = A, B$, similarly to what we did in Chapter III expanding

the state in terms of the PSP's to describe the effect of PMD in the channel. This leads to

$$|\psi\rangle = |\tilde{f}(\omega_A, \omega_B)\rangle \otimes \left[\frac{\eta_1}{\sqrt{2}} (|u_A, u_B\rangle + e^{i\alpha_1} |u'_A, u'_B\rangle) + \frac{\eta_2}{\sqrt{2}} (|u_A, u'_B\rangle - e^{i\alpha_2} |u'_A, u_B\rangle) \right],$$
(4.32)

where

$$\eta_1 = \langle u_A|h_A\rangle \langle u_B|h_B\rangle + e^{i\alpha} \langle u_A|v_A\rangle \langle u_B|v_B\rangle$$

$$\eta_2 = \langle u_A|h_A\rangle \langle u'_B|h_B\rangle + e^{i\alpha} \langle u_A|v_A\rangle \langle u'_B|v_B\rangle$$

and α_i is again defined through the relation $\eta_i = |\eta_i| e^{i(\alpha-\alpha_i)/2}$.

In this basis, the effect of PDL is that of pure gain (or attenuation, depending on the polarization state), so that after experiencing PDL in both arms, the polarization-dependent part of the state can be written as:

$$|\psi_{\text{PDL}}\rangle = \frac{\eta_1}{\sqrt{2}} e^{\frac{\gamma_A+\gamma_B}{2}} |u_A, u_B\rangle + \frac{\eta_2}{\sqrt{2}} e^{\frac{\gamma_A-\gamma_B}{2}} |u_A, u'_B\rangle +$$
$$- \frac{\eta_2 e^{i\alpha_2}}{\sqrt{2}} e^{-\frac{\gamma_A-\gamma_B}{2}} |u'_A, u_B\rangle + \frac{\eta_1 e^{i\alpha_1}}{\sqrt{2}} e^{-\frac{\gamma_A+\gamma_B}{2}} |u'_A, u'_B\rangle.$$
(4.33)

We now need to account for the effect of PMD in arm A. To this end, it is useful to express the polarization of photon A in the PSP basis $\{|s_A\rangle, |s'_B\rangle\}$. For ease of notation we introduce the parameters $\xi_1 = \langle s_A|u_A\rangle$ and $\xi_2 = \langle s'_A|u_A\rangle$ so that the state becomes:

$$|\psi_{\text{PDL}}\rangle = \frac{e^{\frac{\gamma_A+\gamma_B}{2}}}{\sqrt{2}} e^{i\frac{\alpha}{2}} \left(|\eta_1|\xi_1 e^{-i\frac{\alpha_1}{2}} + |\eta_2|\xi_2^* e^{-\gamma_A} e^{i\frac{\alpha_2}{2}} \right) |s_A, u_B\rangle +$$
$$+ \frac{e^{\frac{\gamma_A-\gamma_B}{2}}}{\sqrt{2}} e^{i\frac{\alpha}{2}} \left(|\eta_2|\xi_1 e^{-i\frac{\alpha_2}{2}} - |\eta_1|\xi_2^* e^{-\gamma_A} e^{i\frac{\alpha_1}{2}} \right) |s_A, u'_B\rangle +$$
$$+ \frac{e^{-\frac{\gamma_A-\gamma_B}{2}}}{\sqrt{2}} e^{i\frac{\alpha}{2}} \left(|\eta_1|\xi_2 e^{\gamma_A} e^{-i\frac{\alpha_1}{2}} - |\eta_2|\xi_1^* e^{i\frac{\alpha_2}{2}} \right) |s'_A, u_B\rangle +$$
$$+ \frac{e^{-\frac{\gamma_A+\gamma_B}{2}}}{\sqrt{2}} e^{i\frac{\alpha}{2}} \left(|\eta_2|\xi_2 e^{\gamma_A} e^{-i\frac{\alpha_2}{2}} + |\eta_1|\xi_1^* e^{i\frac{\alpha_1}{2}} \right) |s'_A, u'_B\rangle.$$
(4.34)

Notice that $\xi_1^* = \langle s'_A|u'_A\rangle$ and $\xi_2^* = -\langle s_A|u'_A\rangle$, and that $|\xi_1|^2 + |\xi_2|^2 = 1$. To further simplify the notation, we just express the state as

$$|\psi_{\text{PDL}}\rangle = c_1 |s_A, u_B\rangle + c_2 |s_A, u'_B\rangle + c_3 |s'_A, u_B\rangle + c_4 |s'_A, u'_B\rangle,$$
(4.35)

with

$$c_1 = \frac{e^{\frac{\gamma_A+\gamma_B}{2}}}{\sqrt{2}} e^{i\frac{\alpha}{2}} \left(|\eta_1|\xi_1 e^{-i\frac{\alpha_1}{2}} + |\eta_2|\xi_2^* e^{-\gamma_A} e^{i\frac{\alpha_2}{2}} \right),$$

$$c_2 = \frac{e^{\frac{\gamma_A - \gamma_B}{2}}}{\sqrt{2}} e^{i\frac{\alpha}{2}} \left(|\eta_2|\xi_1 e^{-i\frac{\alpha_2}{2}} - |\eta_1|\xi_2^* e^{-\gamma_A} e^{i\frac{\alpha_1}{2}} \right),$$

$$c_3 = \frac{e^{-\frac{\gamma_A - \gamma_B}{2}}}{\sqrt{2}} e^{i\frac{\alpha}{2}} \left(|\eta_1|\xi_2 e^{\gamma_A} e^{-i\frac{\alpha_1}{2}} - |\eta_2|\xi_1^* e^{i\frac{\alpha_2}{2}} \right),$$

$$c_4 = \frac{e^{-\frac{\gamma_A + \gamma_B}{2}}}{\sqrt{2}} e^{i\frac{\alpha}{2}} \left(|\eta_2|\xi_2 e^{\gamma_A} e^{-i\frac{\alpha_2}{2}} + |\eta_1|\xi_1^* e^{i\frac{\alpha_1}{2}} \right).$$

In this basis, the effect of PMD in arm A can be easily included, which yields the output state:

$$
\begin{aligned}
|\psi_{\text{OUT}}\rangle = &c_1 \left| f(t_A - \frac{\tau_A}{2}, t_B) \right\rangle \otimes |s_A, u_B\rangle + c_2 \left| f(t_A - \frac{\tau_A}{2}, t_B) \right\rangle \otimes |s_A, u_B'\rangle + \\
&+ c_3 \left| f(t_A + \frac{\tau_A}{2}, t_B) \right\rangle \otimes |s_A', u_B\rangle + c_4 \left| f(t_A + \frac{\tau_A}{2}, t_B) \right\rangle \otimes |s_A', u_B'\rangle.
\end{aligned}
\tag{4.36}
$$

To account for the integration time of the photon detectors, the time modes need to be traced out of the full density matrix $|\psi_{OUT}\rangle\langle\psi_{OUT}|$, that is

$$
\begin{aligned}
\rho &= \int\int dt_A' dt_B' \langle t_A', t_B' | \psi_{OUT} \rangle \langle \psi_{OUT} | t_A', t_B' \rangle \\
&= \int\int d\omega_A' d\omega_B' \langle \omega_A', \omega_B' | \psi_{OUT} \rangle \langle \psi_{OUT} | \omega_A', \omega_B' \rangle.
\end{aligned}
$$

This calculation leads to the following density matrix (after normalization):

$$
\rho = \frac{\rho'}{Tr(\rho')} = \frac{1}{Tr(\rho')}
\begin{bmatrix}
|c_1|^2 & c_1 c_2^* & c_1 c_3^* R^\dagger(\tau) & c_1 c_4^* R^\dagger(\tau) \\
c_1^* c_2 & |c_2|^2 & c_2 c_3^* R^\dagger(\tau) & c_2 c_4^* R^\dagger(\tau) \\
c_1^* c_3 R(\tau) & c_2^* c_3 R(\tau) & |c_3|^2 & c_3 c_4^* \\
c_1^* c_4 R(\tau) & c_2^* c_4 R(\tau) & c_3^* c_4 & |c_4|^2
\end{bmatrix}
\tag{4.37}
$$

where

$$\text{Tr}(\rho') = |c_1|^2 + |c_2|^2 + |c_3|^2 + |c_4|^2 = |\eta_1|^2 \cosh(\gamma_A + \gamma_B) + |\eta_2|^2 \cosh(\gamma_A - \gamma_B), \tag{4.38}$$

and the overlap integral $R(\tau)$ was defined in Eq. (4.4).

Setting the parameters in the density matrix in Eq. (4.37) to certain values allows one to analyze specific configurations. First, we notice that when there is no PDL in the path of photon B and in channel A the PMD vector is aligned with the PDL vector (namely $|\eta_2| = 0, |\xi_2| = 0$ and $\gamma_B = 0$, so that $c_1 = \exp(\gamma_A/2)/\sqrt{2}$, $c_2 = c_3 = 0$, $c_4 = \exp(-\gamma_A/2)/\sqrt{2}$), as expected we obtain the same density matrix as the one in Eq. (4.7).

4.4.2 *PMD-first* in the path of photon A

In this second configuration, the PMD element precedes the PDL element in the channel of photon A. We start by expressing both photons of the input state in the basis of the PSP's $\{s_A, s'_A\}$, so that it becomes:

$$|\psi\rangle = |\tilde{f}(\omega_A, \omega_B)\rangle \otimes \left[\frac{\eta_1}{\sqrt{2}} (|s_A, s_A\rangle + e^{i\alpha_1} |s'_A, s'_A\rangle) + \frac{\eta_2}{\sqrt{2}} (|s_A, s'_A\rangle - e^{i\alpha_2} |s'_A, s_A\rangle) \right], \quad (4.39)$$

with $\eta_{1,2}$ defined in an analogous way as the *PDL-first* scenario. After photon A experiences PMD, the state becomes:

$$
\begin{aligned}
|\psi_{\text{PMD}}\rangle = &\frac{\eta_1}{\sqrt{2}} |f(t_A - \frac{\tau_A}{2}, t_B)\rangle \otimes |s_A, s_A\rangle + \frac{\eta_2}{\sqrt{2}} |f(t_A - \frac{\tau_A}{2}, t_B)\rangle \otimes |s_A, s'_A\rangle + \\
&- \frac{\eta_2 e^{i\alpha_2}}{\sqrt{2}} |f(t_A + \frac{\tau_A}{2}, t_B)\rangle \otimes |s'_A, s_A\rangle + \frac{\eta_1 e^{i\alpha_1}}{\sqrt{2}} |f(t_A + \frac{\tau_A}{2}, t_B)\rangle \otimes |s'_A, s'_A\rangle.
\end{aligned}
\quad (4.40)
$$

To account for the effect of the two PDL elements (one per photon), it is useful to express the state in the PDL eigenstates basis $\{u_A, u'_A\}$, $\{u_B, u'_B\}$, which leads to

$$
\begin{aligned}
|\psi_{\text{PMD}}\rangle = &\\
= &\left[\frac{\varepsilon_1}{\sqrt{2}} (\eta_1\mu_1 - \eta_2\mu_2^*) |f(t_A - \frac{\tau_A}{2}, t_B)\rangle + \frac{\varepsilon_2^*}{\sqrt{2}} e^{i\alpha} (\eta_2^*\mu_1 + \eta_1^*\mu_2^*) |f(t_A + \frac{\tau_A}{2}, t_B)\rangle \right] \otimes |u_A, u_B\rangle \\
+ &\left[\frac{\varepsilon_1}{\sqrt{2}} (\eta_1\mu_2 + \eta_2\mu_1^*) |f(t_A - \frac{\tau_A}{2}, t_B)\rangle + \frac{\varepsilon_2^*}{\sqrt{2}} e^{i\alpha} (\eta_2^*\mu_2 - \eta_1^*\mu_1^*) |f(t_A + \frac{\tau_A}{2}, t_B)\rangle \right] \otimes |u_A, u'_B\rangle \\
+ &\left[\frac{\varepsilon_2}{\sqrt{2}} (\eta_1\mu_1 - \eta_2\mu_2^*) |f(t_A - \frac{\tau_A}{2}, t_B)\rangle - \frac{\varepsilon_1^*}{\sqrt{2}} e^{i\alpha} (\eta_2^*\mu_1 + \eta_1^*\mu_2^*) |f(t_A + \frac{\tau_A}{2}, t_B)\rangle \right] \otimes |u'_A, u_B\rangle \\
+ &\left[\frac{\varepsilon_2}{\sqrt{2}} (\eta_1\mu_2 + \eta_2\mu_1^*) |f(t_A - \frac{\tau_A}{2}, t_B)\rangle - \frac{\varepsilon_1^*}{\sqrt{2}} e^{i\alpha} (\eta_2^*\mu_2 - \eta_1^*\mu_1^*) |f(t_A + \frac{\tau_A}{2}, t_B)\rangle \right] \otimes |u'_A, u'_B\rangle,
\end{aligned}
$$
$$(4.41)$$

where, in order to keep track of the relative orientations of the PDL and PMD vectors, we have introduced the parameters $\varepsilon_{1,2}$ and $\mu_{1,2}$, defined as follows:

$$\varepsilon_1 = \langle u_A | s_A \rangle, \qquad \varepsilon_2 = \langle u'_A | s_A \rangle$$

$$\mu_1 = \langle u_B | s_A \rangle, \qquad \mu_2 = \langle u'_B | s_A \rangle. \quad (4.42)$$

To write down the latter expression in a more concise fashion, we can introduce the quantities $k_1 = (\eta_1\mu_1 - \eta_2\mu_2^*)$ and $k_2 = (\eta_2^*\mu_1 + \eta_1^*\mu_2^*)$, so that after passing through the PDL elements,

the state becomes:

$$|\psi_{\text{OUT}}\rangle =$$

$$= e^{\frac{\gamma_A+\gamma_B}{2}} \left[\frac{\varepsilon_1}{\sqrt{2}} k_1 |f(t_A - \frac{\tau_A}{2}, t_B)\rangle + \frac{\varepsilon_2^*}{\sqrt{2}} e^{i\alpha} k_2 |f(t_A + \frac{\tau_A}{2}, t_B)\rangle\right] \otimes |u_A, u_B\rangle$$

$$+ e^{\frac{\gamma_A-\gamma_B}{2}} \left[\frac{\varepsilon_1}{\sqrt{2}} k_2^* |f(t_A - \frac{\tau_A}{2}, t_B)\rangle - \frac{\varepsilon_2^*}{\sqrt{2}} e^{i\alpha} k_1^* |f(t_A + \frac{\tau_A}{2}, t_B)\rangle\right] \otimes |u_A, u_B'\rangle$$

$$+ e^{-\frac{\gamma_A-\gamma_B}{2}} \left[\frac{\varepsilon_2}{\sqrt{2}} k_1 |f(t_A - \frac{\tau_A}{2}, t_B)\rangle - \frac{\varepsilon_1^*}{\sqrt{2}} e^{i\alpha} k_2 |f(t_A + \frac{\tau_A}{2}, t_B)\rangle\right] \otimes |u_A', u_B\rangle$$

$$+ e^{-\frac{\gamma_A+\gamma_B}{2}} \left[\frac{\varepsilon_2}{\sqrt{2}} k_2^* |f(t_A - \frac{\tau_A}{2}, t_B)\rangle + \frac{\varepsilon_1^*}{\sqrt{2}} e^{i\alpha} k_1^* |f(t_A + \frac{\tau_A}{2}, t_B)\rangle\right] \otimes |u_A', u_B'\rangle.$$

$$(4.43)$$

Tracing out the time/frequency dependent part of the state, we obtain the reduced density matrix:

$$\rho_{1,1} = \frac{e^{\gamma_A+\gamma_B}}{2Tr(\rho)}\{|\varepsilon_1|^2|k_1|^2 + |\varepsilon_2|^2|k_2|^2 + 2\text{Re}[\varepsilon_1 k_1 \varepsilon_2 k_2^* e^{-i\alpha} R^\dagger(\tau_A)]\},$$

$$\rho_{2,2} = \frac{e^{(\gamma_A-\gamma_B)}}{2Tr(\rho)}(|\varepsilon_1|^2|k_2|^2 + |\varepsilon_2|^2|k_1|^2 - 2\text{Re}[\varepsilon_1 k_1 \varepsilon_2 k_2^* e^{-i\alpha} R^\dagger(\tau_A)]),$$

$$\rho_{3,3} = \frac{e^{-(\gamma_A-\gamma_B)}}{2Tr(\rho)}(|\varepsilon_2|^2|k_1|^2 + |\varepsilon_1|^2|k_2|^2 - 2\text{Re}[\varepsilon_1 k_1 \varepsilon_2 k_2^* e^{-i\alpha} R^\dagger(\tau_A)])$$

$$\rho_{4,4} = \frac{e^{-(\gamma_A+\gamma_B)}}{2Tr(\rho)}(|\varepsilon_2|^2|k_2|^2 + |\varepsilon_1|^2|k_1|^2 + 2\text{Re}[\varepsilon_1 k_1 \varepsilon_2 k_2^* e^{-i\alpha} R^\dagger(\tau_A)]),$$

$$\rho_{1,2} = \rho_{2,1}^\dagger = \frac{e^{\gamma_A}}{2Tr(\rho)}(|\varepsilon_1|^2 k_1 k_2 + \varepsilon_1^* \varepsilon_2^* k_2^2 e^{i\alpha} R(\tau_A) - \varepsilon_1 \varepsilon_2 k_1^2 e^{-i\alpha} R^\dagger(\tau_A) - |\varepsilon_2|^2 k_1 k_2),$$

$$\rho_{1,3} = \rho_{3,1}^\dagger = \frac{e^{\gamma_B}}{2Tr(\rho)}(\varepsilon_1 \varepsilon_2^* |k_1|^2 + (\varepsilon_2^*)^2 k_1^* k_2 e^{i\alpha} R(\tau_A) - \varepsilon_1^2 k_1 k_2^* e^{-i\alpha} R^\dagger(\tau_A) - \varepsilon_1 \varepsilon_2^* |k_2|^2),$$

$$\rho_{1,4} = \rho_{4,1}^\dagger = \frac{1}{2Tr(\rho)}(2\varepsilon_1 \varepsilon_2^* k_1 k_2 + (\varepsilon_2^*)^2 k_2^2 e^{i\alpha} R(\tau_A) + \varepsilon_1^2 k_1^2 e^{-i\alpha} R^\dagger(\tau_A)),$$

$$\rho_{3,2} = \rho_{2,3}^\dagger = \frac{1}{2Tr(\rho)}(2\varepsilon_1^* \varepsilon_2 k_1 k_2 - (\varepsilon_1^*)^2 k_2^2 e^{i\alpha} R(\tau_A) - \varepsilon_2^2 k_1^2 e^{-i\alpha} R^\dagger(\tau_A)),$$

$$\rho_{2,4} = \rho_{4,2}^\dagger = \frac{e^{-\gamma_B}}{2Tr(\rho)}(\varepsilon_1 \varepsilon_2^* |k_2|^2 - (\varepsilon_2^*)^2 k_1^* k_2 e^{i\alpha} R(\tau_A) + \varepsilon_1^2 k_1 k_2^* e^{-i\alpha} R^\dagger(\tau_A) - \varepsilon_1 \varepsilon_2^* |k_1|^2),$$

$$\rho_{3,4} = \rho_{4,3}^\dagger = \frac{e^{-\gamma_A}}{2Tr(\rho)}(|\varepsilon_2|^2 k_1 k_2 - \varepsilon_1^* \varepsilon_2^* k_2^2 e^{i\alpha} R(\tau_A) + \varepsilon_1 \varepsilon_2 k_1^2 e^{-i\alpha} R^\dagger(\tau_A) - |\varepsilon_1|^2 k_1 k_2),$$

$$(4.44)$$

with

$$\text{Tr}(\rho) = \left[|\varepsilon_1|^2|k_1|^2 + |\varepsilon_2|^2|k_2|^2 + 2Re(\varepsilon_1 \varepsilon_2 k_1 k_2^* e^{-i\alpha} R^\dagger(\tau_A))\right] \cosh(\gamma_A + \gamma_B)$$

$$+ \left[|\varepsilon_1|^2|k_2|^2 + |\varepsilon_2|^2|k_1|^2 - 2Re(\varepsilon_1 \varepsilon_2 k_1 k_2^* e^{-i\alpha} R^\dagger(\tau_A))\right] \cosh(\gamma_A - \gamma_B).$$

$$(4.45)$$

Again, setting $\gamma_B = 0$ allows one to recover Eq. (4.7).

4.5 Nonlocal compensation and channel asymmetry

Equations (4.37) and (4.44) describe the received two-photon state in the *PDL-first* and *PMD-first* scenarios, for arbitrary amounts of PMD and PDL, and for every possible relative orientation between the vectors characterizing the two effects. Setting the parameters to specific values allows one to recover particular configurations that might be more insightful than the one described by the general density matrices.

An interesting feature is the possibility of performing nonlocal PDL compensation. First, suppose that Alice's PDL and PMD vectors are aligned, which implies $|\eta_2| = 0$ in Eq. (4.37) and $|\varepsilon_2| = 0$ in Eq. (4.44). If Bob is able to control the PDL element on his side, such that he can make sure that the corresponding PDL vector is opposite with Alice's and is equal in magnitude, such that $\gamma_B = -\gamma_A$ (and also, $|\xi_2| = 0$, so that $c_1 = c_4 = 1/\sqrt{2}$, $c_2 = c_3 = 0$ in Eq. (4.37), and $|\mu_2| = 0$ in Eq. (4.44)) the density matrices in Eq. (4.37) and (4.44) both reduce to

$$\rho = \begin{pmatrix} \frac{1}{2} & 0 & 0 & \frac{R^\dagger(\tau)}{2} \\ 0 & 0 & 0 & 0 \\ 0 & 0 & 0 & 0 \\ \frac{R(\tau)}{2} & 0 & 0 & \frac{1}{2} \end{pmatrix}. \tag{4.46}$$

This is the density matrix describing the received state in the case in which only PMD is present in the path of photon A (as was shown in Eq. (3.36)), meaning that the PDL on Bob's side has perfectly compensated for the PDL on Alice's side, and the overall effect reduces to that of only PMD being in the channel.

When the PDL and PMD vectors on Alice's side are not aligned, the effectiveness of this nonlocal compensation scheme is different for the *PDL-first* and *PMD-first* configurations. Starting from the former case the received two-photon state is described by the density matrix

$$\rho = \begin{pmatrix} \frac{|\xi_1|^2}{2} & -\frac{\xi_1\xi_2}{2} & \frac{\xi_1\xi_2}{2}R^\dagger(\tau) & \frac{\xi_1^2}{2}R^\dagger(\tau) \\ -\frac{\xi_1\xi_2}{2} & \frac{|\xi_2|^2}{2} & -\frac{\xi_2^2}{2}R^\dagger(\tau) & -\frac{\xi_1\xi_2}{2}R^\dagger(\tau) \\ \frac{\xi_1\xi_2}{2}R(\tau) & -\frac{\xi_2^2}{2}R(\tau) & \frac{|\xi_2|^2}{2} & \frac{\xi_1\xi_2}{2} \\ \frac{\xi_1^2}{2}R(\tau) & -\frac{\xi_1\xi_2}{2}R(\tau) & \frac{\xi_1\xi_2}{2} & \frac{|\xi_1|^2}{2} \end{pmatrix}. \tag{4.47}$$

We remind the reader that $|\xi_1|$ quantifies the relative alignment between the PDL and PMD

vectors on Alice's side. The density matrix was obtained assuming that Bob could perform the nonlocal compesation scheme by controlling the PDL element on his side; specifically, once again he needs to make sure that his element is counter-aligned with respect to Alice's PDL element and has the same magnitude, which is equivalent to setting $\gamma_B = -\gamma_A$ and $|\eta_1| = 1$ in Eq. (4.37).

The density matrix in this form is not particularly meaningful, but if we now apply a suitable rotation to photon B in the form

$$V = \frac{1}{\sqrt{2}} \begin{pmatrix} 1 & 0 \\ 0 & 1 \end{pmatrix} \otimes \begin{pmatrix} \xi_1 & -\xi_2 \\ \xi_2 & \xi_1 \end{pmatrix} = \frac{1}{\sqrt{2}} \begin{pmatrix} \xi_1 & -\xi_2 & 0 & 0 \\ \xi_2 & \xi_1 & 0 & 0 \\ 0 & 0 & \xi_1 & -\xi_2 \\ 0 & 0 & \xi_2 & \xi_1 \end{pmatrix}, \tag{4.48}$$

it is very easy to see that the the new density matrix

$$\rho_{\text{new}} = V^\dagger \rho V \tag{4.49}$$

coincides with the one in Eq. (4.46), meaning that regardless of the orientation of the PMD and PDL elements on arm A, perfect nonlocal compensation of PDL is always achievable.

To experimentally test this result, we reproduced in the laboratory two configurations: in the first one the PMD and PDL vectors in channel A are aligned, while in the second one they are orthogonal on the Block sphere. In both cases, Bob is able to apply an amount of PDL on photon B equal to the one on Alice's side. The experimental results, obtained using the setup schematically depicted in Fig. 4.1, are presented in Fig. 4.7. A fixed PMD element follows the PDL one in channel A and is responsible for the decreased concurrence of $C = 0.66$ for $\gamma_A = 0$. Color-coded filled and empty symbols correspond to aligned and orthogonal $\vec{\tau}$ and $\vec{\gamma}_A$, respectively. The dashed curve is a plot of Eq. (4.8). The upper set of data points demonstrates entanglement restoration when an extra filter is added to channel B. The solid curve shows the restored concurrence value, also given by the same equation with $\gamma_A = 0$, that is, the value that would be observed if only the decohering element were present in the optical path of photon A [39]. The data points show that full compensation can be achieved for all filtering levels regardless of the relative orientation of $\boldsymbol{\tau}$ and $\boldsymbol{\gamma}_A$.

The situation changes drastically when the in the *PMD-first* configuration in channel A. Clearly, when τ and γ_A are aligned, full compensation is always possible, as shown in Fig. 4.8.a: both the theoretical curve and the experimental markers show that the concurrence of the state can be restored to the level that it has when only PMD is present in channel A.
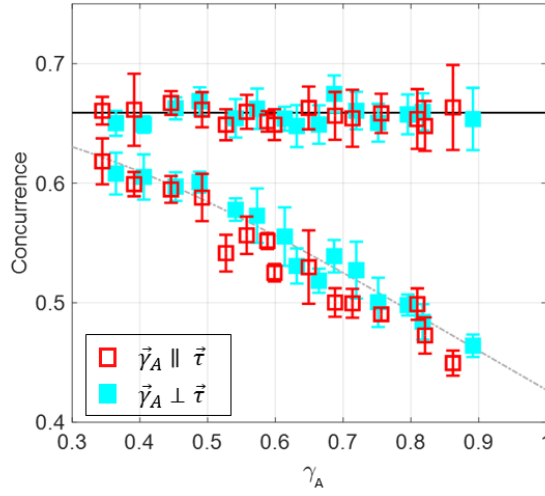
Figure 4.7: Concurrence versus the filtering magnitude γ_A in the *PDL-first* scenario. Empty
and filled markers correspond to the cases in which the vectors $\vec{\gamma}_A$ and $\vec{\tau}$ are aligned and
orthogonal, respectively. The upper set of data points refer to the case in which nonlocal
compensation of modal filtering is implemented by passing photon B through and additional
filtering element. The dashed curve is the analytical result Eq. (4.8) and the solid curve
shows the restored concurrence level, also given by the same equation with $\gamma = 0$.

When $\vec{\tau}$ and $\vec{\gamma}_A$ are not aligned, on the other hand, full compensation is never achievable,
because it's impossible to recover the density matrix in Eq. (4.46). For example, if we consider
the scenario in which $\vec{\tau}$ and $\vec{\gamma}_A$ are orthogonal on the Bloch sphere (which represents the
worst-case scenario) the density matrix of the received state when nonlocal PDL compensation
is performed with $|\vec{\gamma}_B| = |\vec{\gamma}_A|$ is given by

$$\rho = \frac{1}{2Tr(\rho')} \begin{pmatrix} (1+R(\tau)) & 0 & 0 & (1+R(\tau)) \\ 0 & e^{2\gamma_A}(1-R(\tau)) & (1-R(\tau)) & 0 \\ 0 & (1-R(\tau_A)) & e^{-2\gamma_A}(1-R(\tau)) & 0 \\ (1+R(\tau)) & 0 & 0 & (1+R(\tau)) \end{pmatrix}, \qquad (4.50)$$

with

$$Tr(\rho') = 1 + R(\tau_A) + (1 - R(\tau_A))\cosh(2\gamma_A).$$

The concurrence of this state is lower than the one that one would have with only PMD in
the channel.

As discussed in [58], it turns out that setting $|\vec{\gamma}_B| = |\vec{\gamma}_A|$ is not the best one can do to
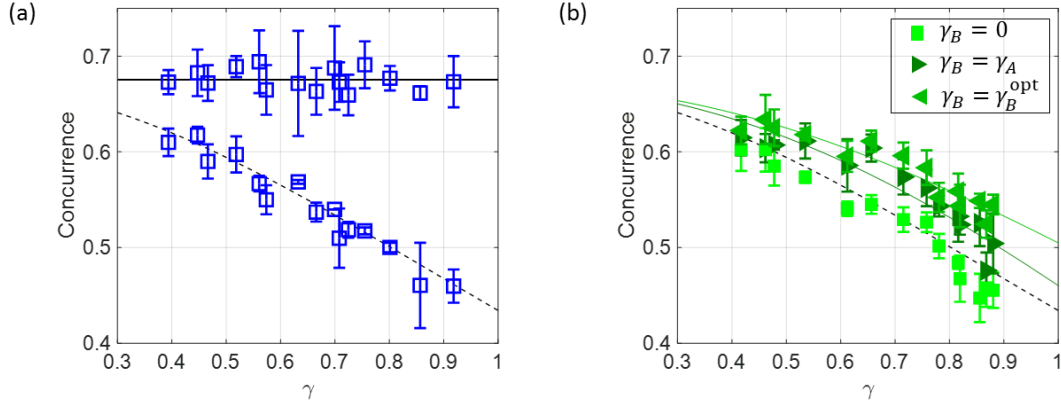
Figure 4.8: Concurrence versus the filtering magnitude γ in the *PMD-first* scenario. Panel (a) corresponds to the case in which the vectors $\vec{\gamma}_A$ and $\vec{\tau}$ are aligned, while (b) refers to the orthogonal case. The upper sets of data points refer to the case in which nonlocal compensation of modal filtering is implemented by passing photon B through and additional filtering element. The dashed curve is the analytical result Eq. (4.8); the solid curve in (a) shows the fully restored concurrence level, while in (b) the symbols denote the values of γ_B used to compensate: dark green $\triangleright$ refers to $|\gamma_B| = |\gamma_A|$, bright green $\triangleleft$ refers to $\gamma_B = \gamma_B^{\mathrm{opt}}$.

optimize the recovery of concurrence. In fact an optimum compensation value γ_B^{opt} exists, which allows one to obtain a higher final concurrence. This optimum value depends on the PMD in the channel and on γ_A, and is given by [58]

$$\gamma_B^{\mathrm{opt}} = \tanh^{-1}\left(|R(\tau)| \tanh\left(\gamma_A\right)\right). \tag{4.51}$$

Nonlocal compensation in the *PMD-first* orthogonal case is presented in Fig. 3.3, for the case in which compensation is performed by introducing an amount of PDL $|\vec{\gamma}_B| = |\vec{\gamma}_A|$ (dark green $\triangleright$ markers) and for the case in which $\gamma_B = \gamma_B^{\mathrm{opt}}$ (bright green $\triangleleft$ markers).

The knowledge of whether filtering is concentrated toward the beginning or the end of a long optical route is thus very important for what is called Procrustean entanglement distillation [59–61], as we have just illustrated above with our two-element model. The greater effectiveness of nonlocal compensation in the *PDL-first* configuration relative to the *PMD-first* configuration demonstrated above introduces an asymmetry in the quantum channel and has important implications in the design of optical networks for polarization-entanglement distribution. Indeed, the same channel could in general be used for photon distribution in two opposite directions, as could be the case for a specific graph edge of a quantum network, or when two parties take turns in exchanging messages using a point-to-point connection.

Either way, the resulting channel will cause different impairments depending on the photon's propagation direction [62].

As a final remark, it is worth stressing out that in both the *PMD-first* case and the *PDL-first* case the restoration of concurrence by means of nonlocal PDL compesation comes at a cost. As discussed in [42] in fact, introducing a PDL element in the path of photon B has the effect of increasing the losses, so that the overall transmission rate will be lower.

CHAPTER 5

Unfaithful Entanglement

Determining if a state is entangled or not can be very demanding in terms of computational times. In fact, even with knowledge of the full density matrix (obtained via a process like quantum state tomography), determining whether a given state is separable is NP-hard [63]. One prominent approach to verifying entanglement without full state characterization is to use an entanglement witness. An entanglement witness is a Hermitian operator W that has a positive expectation value for any separable state, but a negative expectation value for an entangled state of interest [4, 64]. Therefore, given a target output state for a system, it is possible to construct an entanglement witness that will verify the entanglement of that state by measuring only a single expectation value.

In this last chapter we focus on a specific class of entanglement witnesses, namely fidelity-based ones. We introduce the concept of faithfulness, and show how simple application of decoherence and modal filtering (which, as should be clear to the reader by now, in fiber-optic communications are represented by PMD and PDL, respectively) on a pair of entangled qubits can lead to the development of unfaithful entanglement. We reproduce this scenario experimentally, and we show how certain unfaithful states can be made detectable at the cost of further reducing their entanglement.

All the sections that compose this chapter present original work, with the exception of Section 5.1 where an introduction to the concept of *unfaithful entanglement* is provided. The scenario we describe in this chapter is also the central subject of paper 1.

5.1   Fidelity-based entanglement witnesses

An entanglement witness is a Hermitian operator W constructed such that

$$\mathrm{Tr}\left(W\rho_s\right) \geq 0, \quad \mathrm{Tr}\left(W\rho_e\right) < 0 \tag{5.1}$$

where ρ_s is any separable state and ρ_e is at least one entangled state [5, 65, 66].

It has been proven that for every entangled state ρ_e, it is possible to construct an entanglement witness [66]. Despite the guaranteed existence of an entanglement witness and the myriad of construction methods, it is often challenging to realize a witness experimentally. Due to their relative simplicity, witnesses based on the fidelity of a state to a pure entangled state $|\psi\rangle$ [67] are often the approach of choice in experimental scenarios.

Fidelity $F_\psi(\rho) = \langle\psi|\rho|\psi\rangle$ is usually employed to measure the distance of a general state ρ from the state $|\psi\rangle$. Starting from this, one can then build the related entanglement witness as [68]

$$W_\psi = \alpha\mathbb{I} - |\psi\rangle\langle\psi|, \tag{5.2}$$

where α is a suitably chosen real number. Measuring the observable W leads to the quantity $\text{Tr}(\rho W) = \alpha - F_\psi(\rho)$; if F_ψ is above the threshold α, the witness operator has detected the presence of entanglement. Clearly, one wants α to be as small as possible, so the witness can detect a larger amount of entangled states. Still, this method for entanglement detection is limited by the minimum value that α can have, and will thus have the drawback (common to every entanglement witness approach) of not being able to detect all entangled states. The term *unfaithful* has been applied to the set of states that cannot be detected by any construction of a fidelity witness [67, 69, 70].

From a geometrical point of view, an entanglement witness is a hyperplane that is guaranteed to have all separable states on one side and at least one entangled state on the other [5]. With this picture in mind, we can see that a given entanglement witness will generally detect only a small subset of entangled states, namely those that fall on the same side of the hyperplane as the entangled state targeted in the construction of the witness. Fidelity-based witnesses W_ψ also have a clear geometrical interpretation, as shown in Fig. 5.1. From this, it is also not surprising that not all entangled states can be detected by this specific class of witnesses.

5.1.1 Faithfulness of two-qubit states

Recently, an analytical method for determining the faithfulness of any two-qubit state was provided [69]. In order to be more explicit, we first express an arbitrary two qubit state ρ_{AB} as

$$\rho_{AB} = \frac{1}{4}\Big(\sigma_0\otimes\sigma_0 + \vec{r}\cdot\vec{\sigma}\otimes\sigma_0 + \sigma_0\otimes\vec{s}\cdot\vec{\sigma} + \sum_{m,n=1}^{3} t_{nm}\sigma_n\otimes\sigma_m\Big), \tag{5.3}$$

with the σ_i representing the Pauli operators along with $\sigma_0 = \mathbb{I}$. The coefficients of $t_{mn} = \text{Tr}(\rho\sigma_n\otimes\sigma_m)$ define a real 3×3 matrix defined as T and contain all of the joint correlations
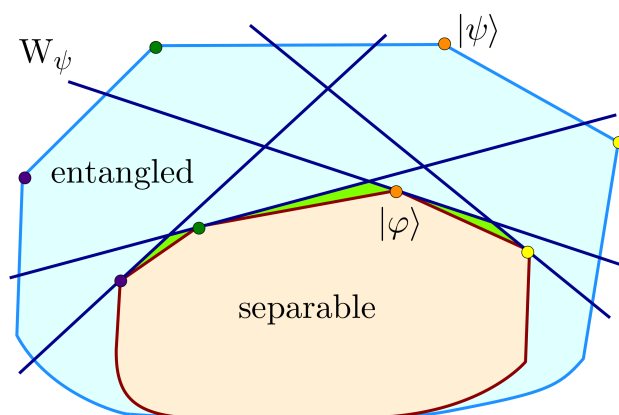
Figure 5.1: Schematic explanation of faithful and unfaithful entanglement. The set of all states is a convex set with the separable states as a convex subset; the extreme points of both sets correspond to pure states. For constructing a fidelity-based witness, one starts with an entangled pure state $|\psi\rangle$ and computes the closest separable state $|\varphi\rangle$, where the distance is measured by the squared overlap. Then, the fidelity-based witness W_ψ is constructed by the condition that it should detect all states which have a smaller distance to $|\psi\rangle$ than the state $|\varphi\rangle$ has. The witness is depicted by the line in state space where $\mathrm{Tr}\,(\rho W_\psi) = 0$, and the states above this line are detected as entangled. The figure shows this procedure for four exemplary pure states. States that can be detected by a fidelity-based witness are called faithful, but some entangled states (depicted in green) do not fall in this category and are hence unfaithful.

of ρ. The local density matrices are defined as

$$\rho_A = \text{Tr}_B[\rho_{AB}] = \frac{1}{2}\left(\sigma_0 + \vec{r}\cdot\vec{\sigma}\right), \quad \rho_B = \text{Tr}_A[\rho_{AB}] = \frac{1}{2}\left(\sigma_0 + \vec{s}\cdot\vec{\sigma}\right), \tag{5.4}$$

The condition $\vec{r} = \vec{s} = 0$ (which defines Bell-diagonal states) physically corresponds to $\rho_A = \rho_B = \sigma_0/2$, meaning the state has totally mixed marginals. Note that the correlation matrix T can always be diagonalized through local rotations [37], and hence any state with totally mixed marginals is Bell diagonal in some basis.

The faithfulness of ρ_{AB} can then be determined using the operator

$$X_2(\rho_{AB}) = \rho_{AB} - \frac{1}{2}\left(\rho_A \otimes \sigma_0 + \sigma_0 \otimes \rho_B\right) + \frac{1}{2}\sigma_0 \otimes \sigma_0, \tag{5.5}$$

where $\rho_{A,B}$ are the local density matrices. Notice that this operator removes the local correlations of a given density matrix while preserving the joint correlations in the T matrix. A two-qubit state ρ_{AB} is faithful if and only if the largest eigenvalue of $X_2(\rho_{AB})$ is greater than $1/2$ [69]. States with completely mixed marginals, meaning they are Bell-diagonal in some basis, are only entangled when the largest eigenvalue of the state is greater than $1/2$ [71]. Hence, for Bell-diagonal states in any basis, faithfulness and entanglement are in a one-to-one relation, implying that only states wit local correlations can potentially be entangled but unfaithful.

Our aim is to find states, accessible via conventional noise mechanisms, for which the largest eigenvalue of $X_2(\rho)$ is $1/2$ or less but has a concurrence greater than 0, which gives rise to the presence of unfaithful entanglement.

5.1.2 Fully entangled fraction and faithfulness

Beyond separability, the quality and type of entanglement present in a state determines how useful it is for various applications. To this end, we introduce another useful quantity, namely the *fully entangled fraction* (FEF), sometimes also referred to as the maximal singlet fraction. The FEF is given by

$$F(\rho) = \max_{|\psi\rangle \in \text{ME}} \langle\psi|\rho|\psi\rangle, \tag{5.6}$$

where the maximization is over all maximally entangled (ME) states. The FEF is directly related to how useful a state is for teleportation. In the two-qubit case, only states having $F(\rho) > \frac{1}{2}$ can teleport a state with a higher fidelity than a classical channel [72, 73]. Despite the clear physical meaning of FEF, it is not an entanglement monotone and can show surprising behavior when compared with the concurrence [74], a concept we will demonstrate

experimentally later in this chapter. Further, the FEF establishes upper and lower bounds on the concurrence and negativity [75, 76]. We note that while FEF is in general difficult to evaluate as it requires a maximization, analytical results do exist for two qubits [37, 75, 77], and estimates exist for higher-dimensional systems [69, 78, 79].

The fully entangled fraction and the faithfulness of a state are related; one can in fact show that the maximum eigenvalue of the $X_2(\rho)$ operator from Eq. (5.5) coincides with the FEF. This result is central to our further discussion and, therefore, is worth stressing:

Observation. *For two-qubit states, the maximum eigenvalue of the $X_2(\rho_{AB})$ operator coincides with the FEF of the state. This implies that an entangled state is unfaithful when $F(\rho_{AB}) \leq 1/2$.*

The formal proof for this observation can be found in Refs. [37, 69], and for completeness, we also present it here. We start with the generic two-qubit state of Eq. (5.3), where the correlation matrix, defined as the matrix made up of the coefficients $t_{i,j} = \text{Tr}\,(\rho_{AB}\sigma_i \otimes \sigma_j)$ for nonzero i, j, can always be diagonalized via local rotations, resulting in

$$\rho'_{AB} = \frac{1}{4}\left(\sigma_0 \otimes \sigma_0 + \vec{r}' \cdot \vec{\sigma} \otimes \sigma_0 + \sigma_0 \otimes \vec{s}' \cdot \vec{\sigma} + \sum_{m=1}^{3} t'_m \sigma_m \otimes \sigma_m\right). \tag{5.7}$$

Using this form, the FEF, as in Eq. (5.6), can be evaluated as [37]

$$F(\rho_{AB}) = \begin{cases} \frac{1}{4}(1 + \sum_i |t'_i|) & \text{if} \quad \det\,(T') \leq 0 \\ \frac{1}{4}[1 + \max_{i \neq j \neq k}\,(|t'_i| + |t'_j| - |t'_k|)] & \text{if} \quad \det\,(T') > 0 \end{cases} \tag{5.8}$$

where T' is a diagonal matrix with entries t'_i. The operator $X_2(\rho_{AB})$, on the other hand, can be expressed as

$$X_2(\rho_{AB}) = \frac{1}{4}\left(\sigma_0 \otimes \sigma_0 + \sum_{m,n=1}^{3} t_{nm} \sigma_n \otimes \sigma_m\right), \tag{5.9}$$

whose correlation matrix can again be diagonalized in the same way. One can thus explicitly determine the relationship between the eigenvalues of $X_2(\rho_{AB})$ and the parameters t'_i

according to [71]

$$\begin{aligned}
\lambda_1 &= \frac{1}{4}\left(1 + t_1' - t_2' + t_3'\right), \\
\lambda_2 &= \frac{1}{4}\left(1 + t_1' + t_2' - t_3'\right), \\
\lambda_3 &= \frac{1}{4}\left(1 - t_1' + t_2' + t_3'\right), \\
\lambda_4 &= \frac{1}{4}\left(1 - t_1' - t_2' - t_3'\right).
\end{aligned}$$

(5.10)

Now, if $\det\left(T'\right) \leq 0$, then one or three of the t_i' coefficients are less than zero, or some of them are zero. In all cases, the maximum eigenvalue of $X_2(\rho_{AB})$ can be written as $\lambda_{\max} = \frac{1}{4}(1 + \sum_i |t_i'|)$. When $\det\left(T'\right) > 0$, two out of the three coefficients will be negative (or all of them will be positive) making the maximum eigenvalue the one that maximizes the combination $|t_i'| + |t_j'| - |t_k'|$, thus concluding the demonstration.

This simple relation we just proved is actually very powerful. On the one hand, it allows one to analytically evaluate the maximum eigenvalue of $X_2(\rho_{AB})$ in situations in which this might be a difficult task. On the other hand, it allows for a physical interpretation of unfaithful two-qubit states as exactly those entangled states that are not useful for teleportation.

5.2 Correlated faithfulness and concurrence

In this section, we show how two-qubit unfaithful states can result from relatively simple applications of decoherence and filtering to Bell states. To begin, we consider a Bell state that has undergone a decoherence process that reduces the off-diagonal terms in the computational basis. This simple scenario is of practical interest since it can often be encountered in real-life situations. For example, it describes the case in which the initial Bell state is represented by a pair of polarization-entangled photons, and one or both photons propagate in a channel with first-order polarization-mode dispersion (PMD), as we have shown earlier in this work. The resulting state can then be represented as a Bell-diagonal state, which, up to local rotations, can be expressed in terms of the Pauli matrices as

$$\rho_0 = \frac{1}{4}\left(\sigma_0 \otimes \sigma_0 + \sum_{j=1}^{3} t_j(\sigma_j \otimes \sigma_j)\right).$$

(5.11)

The values of the t_j coefficients are constrained by the positivity conditions on the eigenvalues of ρ_0. Moreover, the Bell-diagonal state is separable if it obeys the stronger condition $\sum_j |t_j| \leq 1$.

We now consider the application of a filter to this state. Such local filters can be written in

terms of Pauli matrices as

$$f = \mu \left(\sigma_0 + \nu \hat{n} \cdot \vec{\sigma} \right), \tag{5.12}$$

where μ and ν are real numbers and $\hat{n}$ is a unit vector that defines the direction of the filter in Stokes space. Note that the filter f is Hermitian, but this is no restriction since non-Hermitian filters can be represented by Hermitian filters followed by a local unitary transformation.

We refer to the local filter operator acting on qubit A, B of the pair as f_A, f_B. Application of this operator to qubit A results in the unnormalized density matrix

$$\rho' = (f_A \otimes \sigma_0)\rho_0(f_A \otimes \sigma_0)^\dagger = f_A^2 \otimes \sigma_0 + \sum_{j=1}^{3} t_j (f_A \sigma_j f_A \otimes \sigma_j), \tag{5.13}$$

where we have used the fact that f is Hermitian and that the adjoint is distributive over the Kronecker product.

Cumbersome algebra and the use of the relations

$$
\begin{aligned}
(\vec{a} \cdot \vec{\sigma})(\vec{b} \cdot \vec{\sigma}) &= (\vec{a} \cdot \vec{b})\sigma_0 + i(\vec{a} \times \vec{b}) \cdot \vec{\sigma} \\
(\hat{j} \cdot \vec{\sigma})(\vec{b} \cdot \vec{\sigma}) &= \sigma_j(\vec{b} \cdot \vec{\sigma}) = (\hat{j} \cdot \vec{b})\sigma_0 + i(\hat{j} \times \vec{b}) \cdot \vec{\sigma} \\
(\vec{a} \cdot \vec{\sigma})(\hat{j} \cdot \vec{\sigma}) &= (\vec{a} \cdot \vec{\sigma})\sigma_j = (\vec{a} \cdot \hat{j})\sigma_0 + i(\vec{a} \times \hat{j}) \cdot \vec{\sigma}
\end{aligned} \tag{5.14}
$$

can be employed to evaluate the main terms:

$$
\begin{aligned}
f_A^2 &= \mu^2 \left((1+\nu^2)\sigma_0 + 2\nu\hat{n} \cdot \vec{\sigma} \right) \\
f_A^2 \otimes \sigma_0 &= \mu^2(1+\nu^2)\sigma_0 \otimes \sigma_0 + 2\nu\mu^2 \left[(\hat{n} \cdot \vec{\sigma}) \otimes \sigma_0 \right] \\
f_A \sigma_j f_A &= \mu^2 \left((1-\nu^2)\sigma_j + 2\nu(\hat{j} \cdot \hat{n})\sigma_0 + 2\nu^2(\hat{j} \cdot \hat{n})(\hat{n} \cdot \vec{\sigma}) \right).
\end{aligned} \tag{5.15}
$$

After algebra and normalization, the state becomes

$$
\begin{aligned}
\rho_F = \rho'/\mathrm{Tr}(\rho') = &\frac{1}{4}(\sigma_0 \otimes \sigma_0) + \frac{\nu}{2(1+\nu^2)}\left[(\hat{n} \cdot \vec{\sigma}) \otimes \sigma_0 \right] + \frac{\nu}{2(1+\nu^2)}\left[\sigma_0 \otimes ((T\hat{n}) \cdot \vec{\sigma}) \right] \\
&+ \frac{1}{4(1+\nu^2)}\sum_{j=1}^{3} t_j \left((1-\nu^2)\sigma_j + 2\nu^2 n_j(\hat{n} \cdot \vec{\sigma}) \right) \otimes \sigma_j,
\end{aligned} \tag{5.16}
$$

Notice that the normalization coefficient was calculated using the following trace identities

$$
\begin{aligned}
\mathrm{Tr}\,(A \otimes B) &= \mathrm{Tr}(A)\mathrm{Tr}(B) \\
\mathrm{Tr}(A + B) &= \mathrm{Tr}(A) + \mathrm{Tr}(B) \\
\mathrm{Tr}(cA) &= c\mathrm{Tr}(A)
\end{aligned} \tag{5.17}
$$

along with the fact that all of the Pauli matrices are traceless with the exception of $\text{Tr}(\sigma_0) = 2$. We then find

$$
\begin{aligned}
\text{Tr}(\rho') =& \mu^2(1 + \nu^2)\text{Tr}(\sigma_0)\text{Tr}(\sigma_0) + 2\nu\mu^2\left[\text{Tr}((\hat{n} \cdot \vec{\sigma}))\text{Tr}(\sigma_0)\right] \\
& + \sum_{j=1}^3 t_j\mu^2\left((1 - \nu^2)\text{Tr}(\sigma_j)\text{Tr}(\sigma_j) + 2(\hat{j} \cdot \hat{n})\left[\nu\text{Tr}(\sigma_0)\text{Tr}(\sigma_j) + \nu^2(\text{Tr}(\hat{n} \cdot \vec{\sigma}))\text{Tr}(\sigma_j)\right]\right) \\
=& 4\mu^2(1 + \nu^2)
\end{aligned}
$$

$$(5.18)$$

As we showed earlier in this work, the concurrence of ρ_F is independent of $\hat{n}$ and depends only on the magnitude of ν, according to:

$$
C(\rho_F) = C(\rho_0)\frac{|\det(f)|}{\text{Tr}\left[(f^\dagger f \otimes \sigma_0)\rho\right]}.
$$

$$(5.19)$$

To determine when this state becomes unfaithful we need to find the eigenvalues of $X_2(\rho_2)$, which is given by

$$
X_2(\rho_2) = \frac{1}{4}(\sigma_0 \otimes \sigma_0) + \frac{1}{4(1 + \nu^2)}\sum_{j=1}^3 t_j\left((1 - \nu^2)\sigma_j \otimes \sigma_j + 2\nu^2(\hat{j} \cdot \hat{n})\left[(\hat{n} \cdot \vec{\sigma}) \otimes \sigma_j\right]\right) \quad (5.20)
$$

and can always be diagonalized via local rotations to be expressed as

$$
X_2(\rho_F) = \frac{1}{4}(\sigma_0 \otimes \sigma_0) + \sum_{i=1}^3 t_i'(\sigma_i \otimes \sigma_i).
$$

$$(5.21)$$

The eigenvalues λ_i are functions of the coefficients of its correlation matrix T', according to Eq. (5.10). If the maximum eigenvalue of $X_2(\rho_F)$ is no greater than $1/2$, then the state is unfaithful. Equivalently, earlier in this chapter we explained that we can consider the FEF since it coincides with the maximum eigenvalue of $X_2(\rho_F)$. To study how the faithfulness of a Bell-diagonal state is affected by modal filtering, we consider several orientations of the filter in the following sections.

5.2.1 Creating unfaithful entanglement with a single local filter

First, we focus on a simple but representative case, that is, the filter being aligned along the x-axis, such that $\hat{n} = \{1, 0, 0\}$. In this situation, the expressions for the two-photon state ρ_F

and the $X_2(\rho_F)$ operator become, respectively,

$$
\begin{aligned}
\rho_F =& \frac{1}{4} \left(\sigma_0 \otimes \sigma_0 \right) + \frac{\nu}{2(1+\nu^2)} \left[\sigma_1 \otimes \sigma_0 \right] + \frac{t_1 \nu}{2(1+\nu^2)} \left[\sigma_0 \otimes \sigma_1 \right] \\
&+ \frac{t_1 \nu^2}{2(1+\nu^2)} (\sigma_1 \otimes \sigma_1) + \frac{(1-\nu^2)}{4(1+\nu^2)} \sum_{j=1}^{3} t_j \left(\sigma_j \otimes \sigma_j \right),
\end{aligned}
\tag{5.22}
$$

and

$$
\begin{aligned}
X_2(\rho_2^x) =& \frac{1}{4} \left((\sigma_0 \otimes \sigma_0) + \frac{2t_1 \nu^2}{(1+\nu^2)} (\sigma_1 \otimes \sigma_1) + \frac{(1-\nu^2)}{(1+\nu^2)} \sum_{j=1}^{3} t_j \left(\sigma_j \otimes \sigma_j \right) \right) \\
=& \frac{1}{4} \left((\sigma_0 \otimes \sigma_0) + \sum_{j=1}^{3} t_j' \left(\sigma_j \otimes \sigma_j \right) \right).
\end{aligned}
\tag{5.23}
$$

The coefficients t_i' of the diagonal correlation matrix T' are thus given by

$$
\begin{aligned}
t_1' =& \frac{2t_1 \nu^2 + t_1(1-\nu^2)}{1+\nu^2} = t_1, \\
t_2' =& \frac{t_2(1-\nu^2)}{1+\nu^2}, \\
t_3' =& \frac{t_3(1-\nu^2)}{1+\nu^2}.
\end{aligned}
\tag{5.24}
$$

To determine the faithfulness we must find the eigenvalues of $X_2(\rho_F)$. Since this happens to have a diagonal correlation matrix the eigenvalues can be found directly from Eq. (5.10):

$$
\begin{aligned}
\lambda_1 =& \frac{1}{4} \left(1 + t_1 + (t_3 - t_2) \left(\frac{1-\nu^2}{1+\nu^2} \right) \right) \\
\lambda_2 =& \frac{1}{4} \left(1 + t_1 + (t_2 - t_3) \left(\frac{1-\nu^2}{1+\nu^2} \right) \right) \\
\lambda_3 =& \frac{1}{4} \left(1 - t_1 + (t_2 + t_3) \left(\frac{1-\nu^2}{1+\nu^2} \right) \right) \\
\lambda_4 =& \frac{1}{4} \left(1 - t_1 - (t_2 + t_3) \left(\frac{1-\nu^2}{1+\nu^2} \right) \right)
\end{aligned}
\tag{5.25}
$$

which sum to unity.

If we then simplify the description by assuming that the initial Bell Diagonal state is rank two, so that it can be described by the one-parameter state

$$
\rho_0 = \sin^2(\theta) |\phi^+\rangle\langle\phi^+| + \cos^2(\theta) |\phi^-\rangle\langle\phi^-|
\tag{5.26}
$$

whose coefficients in the correlation matrix are $t_1 = -\cos(2\theta)$, $t_2 = \cos(2\theta)$, and $t_3 = 1$. The concurrence of a rank-2 Bell diagonal state is given by $C_0 = C(\rho_0) = |\cos(2\theta)|$ when we limit $0 \leq \theta \leq \pi/4$. For the rest of this chapter, and with no loss of generality, we will limit ourselves to the case in which θ is in the interval $0 \leq \theta < \pi/2$.

Using Eq. (5.19), we see that the concurrence of this state after a local filter $f_A = \mu(\sigma_0 + \nu\sigma_1)$ is applied is given by

$$C = C(\rho_1) = C(\rho)\frac{|\det(f)|}{\mathrm{Tr}\left[(f^\dagger f \otimes \sigma_0)\rho\right]} = |\cos(2\theta)|\frac{1-\nu^2}{1+\nu^2} \tag{5.27}$$

and the eigenvalues become

$$\begin{aligned}
\lambda_1 &= \frac{1}{4}\left(1 - \cos(2\theta) + (1 - \cos(2\theta))\left(\frac{1-\nu^2}{1+\nu^2}\right)\right) = \frac{\sin^2\theta}{1+\nu^2}\\
\lambda_2 &= \frac{1}{4}\left(1 - \cos(2\theta) + (\cos(2\theta) - 1)\left(\frac{1-\nu^2}{1+\nu^2}\right)\right) = \frac{\nu^2\sin^2\theta}{1+\nu^2}\\
\lambda_3 &= \frac{1}{4}\left(1 + \cos(2\theta) + (\cos(2\theta) + 1)\left(\frac{1-\nu^2}{1+\nu^2}\right)\right) = \frac{\cos^2\theta}{1+\nu^2}\\
\lambda_4 &= \frac{1}{4}\left(1 + \cos(2\theta) - (\cos(2\theta) + 1)\left(\frac{1-\nu^2}{1+\nu^2}\right)\right) = \frac{\nu^2\cos^2\theta}{1+\nu^2}
\end{aligned} \tag{5.28}$$

We can eliminate common variables with the relation

$$\frac{C}{C_0} = \frac{1-\nu^2}{1+\nu^2} \tag{5.29}$$

making the eigenvalues

$$\begin{aligned}
\lambda_1 &= \frac{1}{4}\left[1 - C_0 - (C_0 - 1)\frac{C}{C_0}\right]\\
\lambda_2 &= \frac{1}{4}\left[1 - C_0 + (C_0 - 1)\frac{C}{C_0}\right]\\
\lambda_3 &= \frac{1}{4}\left[1 + C_0 + (C_0 + 1)\frac{C}{C_0}\right]\\
\lambda_4 &= \frac{1}{4}\left[1 + C_0 - (C_0 + 1)\frac{C}{C_0}\right]
\end{aligned} \tag{5.30}$$

By inspection the largest eigenvalue is λ_3, and we have $F(\rho_F) \equiv \lambda_3$. Hence it is clear that the FEF is a monotonic function of the concurrence C in this scenario.

We now want to investigate if this simple configuration can lead to the presence of unfaithful entanglement. As mentioned earlier, the condition for an entangled but unfaithful state is $C > 0$ and $F(\rho_F) \leq 1/2$. Notice that if we start with a Bell state, meaning $C = 1$, then $F(\rho_F) = (1 + C)/2$, and as expected there are no situations where the state is unfaithful but
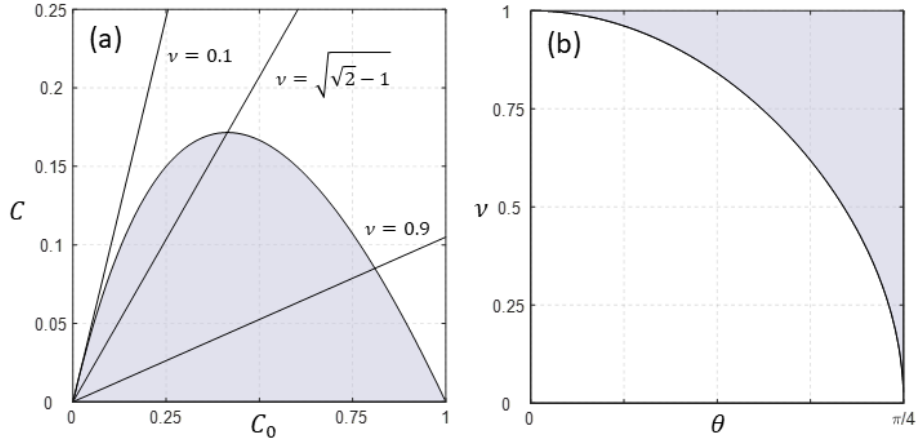
Figure 5.2: (a) Graphical representation of the inequality in Eq. (5.32), where C_0 is the initial concurrence and C is the concurrence obtained after application of a local filter on one of the two qubits. All combinations of C_0 and C that lead to unfaithful entanglement are represented in the shaded area. Straight lines represent the linear relation between concurrence of the initial rank-2 Bell diagonal state and the concurrence of the final state after local filtering has been performed in Eq. (5.29). (b) The same equality is expressed in terms of the amount of filtering ν needed for a state to become unfaithful when the initial Bell diagonal state is characterized by the coefficient θ.

also entangled. The region where unfaithful entanglement occurs fulfills the condition

$$C_0 + C + \frac{C}{C_0} \le 1, \tag{5.31}$$

which can be expressed as

$$C \le \frac{C_0(1 - C_0)}{1 + C_0}. \tag{5.32}$$

This region is represented in Fig. 5.2(a) as the light blue area in the C vs C_0 plane. Straight lines represent the linear relation between the concurrence of the initial rank-2 Bell diagonal state and the concurrence of the final state (after local filtering has been performed) in Eq. (5.29). The figure shows that the highest concurrence for an unfaithful state that we can obtain by application of local filtering on a rank-2 Bell diagonal state is $C = 3 - 2\sqrt{2}$, which can only be obtained by applying a local filter of magnitude $\nu = \sqrt{\sqrt{2} - 1}$ to an initial state with concurrence $C_0 = \sqrt{2} - 1$. Equation (5.32) can also be rewritten to find an explicit relation between the amount of filtering required for the state to become unfaithful and the parameter θ characterizing the initial rank-2 Bell diagonal state to give

$$\frac{1 - \nu^2}{1 + \nu^2} \le \frac{1 - \cos(\theta)}{1 + \cos(\theta)}, \tag{5.33}$$

which is represented in Fig. 5.2(b) (for θ in the range $0 \leq \theta < \pi/4$) by the shaded region. From this figure, it is clear that the larger the value of θ - i.e., the lower the initial concurrence of the rank-2 Bell diagonal state - the lower the amount of filtering needed to reach the region of unfaithful entanglement.

5.2.2 Not all local filter orientations result in unfaithful entanglement

Let's now consider a different filter orientation, which leads to very different results. If the filter is aligned such that $\hat{n} = \{0, 0, 1\}$, then the expression for ρ_F and $X_2(\rho_F)$ become

$$
\begin{aligned}
\rho_F = & \frac{1}{4}\left(\sigma_0 \otimes \sigma_0\right) + \frac{\nu}{2(1+\nu^2)}\left[\sigma_3 \otimes \sigma_0\right] + \frac{t_3\nu}{2(1+\nu^2)}\left[\sigma_0 \otimes \sigma_3\right] \\
& + \frac{t_3\nu^2}{2(1+\nu^2)}(\sigma_3 \otimes \sigma_3) + \frac{(1-\nu^2)}{4(1+\nu^2)}\sum_{j=1}^{3} t_j\left(\sigma_j \otimes \sigma_j\right),
\end{aligned}
\tag{5.34}
$$

and

$$
\begin{aligned}
X_2(\rho_F) = & \frac{1}{4}\left((\sigma_0 \otimes \sigma_0) + \frac{2t_3\nu^2}{(1+\nu^2)}(\sigma_3 \otimes \sigma_3) + \frac{(1-\nu^2)}{(1+\nu^2)}\sum_{j=1}^{3} t_j\left(\sigma_j \otimes \sigma_j\right)\right), \\
= & \frac{1}{4}\left((\sigma_0 \otimes \sigma_0) + \sum_{j=1}^{3} t_j'\left(\sigma_j \otimes \sigma_j\right)\right),
\end{aligned}
\tag{5.35}
$$

where (assuming again that we start with a rank-2 Bell diagonal state)

$$
\begin{aligned}
t_1' = & \frac{t_1(1-\nu^2)}{1+\nu^2} = -\frac{\cos(2\theta)(1-\nu^2)}{1+\nu^2} \\
t_2' = & \frac{t_2(1-\nu^2)}{1+\nu^2} = \frac{\cos(2\theta)(1-\nu^2)}{1+\nu^2} = -t_1^z \\
t_3' = & \frac{2t_3\nu^2 + t_3(1-\nu^2)}{1+\nu^2} = t_3 = 1.
\end{aligned}
\tag{5.36}
$$

The eigenvalues of $X_2(\rho_2^z)$ thus become:

$$
\begin{aligned}
\lambda_1 = & \frac{1}{4}\left(2 - \cos(2\theta)\frac{1-\nu^2}{1+\nu^2}\right), \\
\lambda_2 = & 0, \\
\lambda_3 = & \frac{1}{4}\left(2 + \cos(2\theta)\frac{1-\nu^2}{1+\nu^2}\right), \\
\lambda_4 = & 0.
\end{aligned}
\tag{5.37}
$$

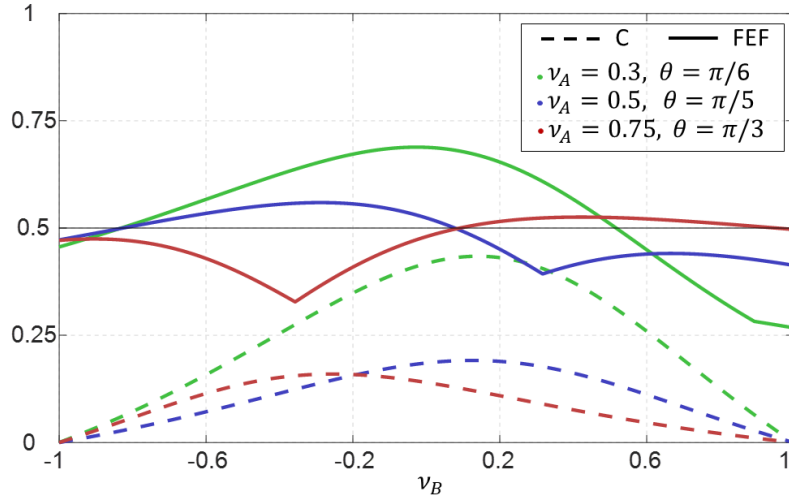Since there are only two non-zero eigenvalues, and they sum to unity, they will never be

Figure 5.3: Theoretical curves for concurrence (dashed lines) and FEF (solid lines) as functions of the amount of filtering ν_B in channel B for three combinations of ν_A and θ. A FEF above 0.5 (shown as a solid black line) means that the state is faithful. Filters in both channels are aligned along the x-axis, which leads to the presence of regions where concurrence and FEF are anti-correlated.

simultaneously less than $1/2$, and the state will never become unfaithful. In fact the fully entangled fraction $F(\rho_{AB})$ in this case becomes

$$F(\rho_{AB}) = \frac{1}{2}\left(1 + \frac{C}{2}\right). \tag{5.38}$$

Since this quantity is always greater than $1/2$, the state never becomes unfaithful.

This result shows how the faithfulness of a rank-2 Bell diagonal state on which a filter is applied is sensitive to the orientation of the filter itself. If the filter is aligned with the z-axis, one can never obtain an unfaithful state. This is in sharp contrast with the behavior of concurrence, which is orientation-independent.

5.3   Anti-correlated faithfulness and concurrence

We now move to the description of a different scenario. Let's start again from the rank-2 Bell-diagonal state in Eq. (5.26). If we now apply a filter aligned in the x-direction to each qubit, so that the resulting operators are

$$f_A = (\sigma_0 + \nu_A \sigma_1), \quad f_B = (\sigma_0 + \nu_B \sigma_1), \tag{5.39}$$

the final state ρ has a concurrence given by

$$C(\rho_F) = \frac{|(\nu_A^2 - 1)(\nu_B^2 - 1)\cos(2\theta)|}{(\nu_A^2 + 1)(\nu_B^2 + 1) - 4\nu_A\nu_B\cos(2\theta)}, \tag{5.40}$$

while, again limiting ourselves to the range $0 \leq \theta < \pi/2$, the FEF becomes

$$F(\rho_F) = \frac{\max\left[\sin^2(\theta)(\nu_A\nu_B + 1)^2, \cos^2(\theta)(\nu_A\nu_B - 1)^2\right]}{(\nu_A^2 + 1)(\nu_B^2 + 1) - 4\nu_A\nu_B\cos(2\theta)}. \tag{5.41}$$

If we assume that the amount of filtering ν_A in channel A and θ are fixed, we can obtain by means of a simple derivative the value of $\nu_B^{\max}$ for which the maximum FEF occurs. In fact, by setting $\frac{\mathrm{d}F(\rho_F)}{\mathrm{d}\nu_B} = 0$ and solving for ν_B, one has

$$F^{\max}(\rho_F) = \max\left[\frac{(1 + \nu_A^2)^2 + 4\nu_A^2\cos(2\theta)}{1 + \nu_A^4 - 2\nu_A\cos(4\theta)}\sin^2\theta,\right.$$
$$\left.\frac{(1 + \nu_A^2)^2 - 4\nu_A^2\cos(2\theta)}{1 + \nu_A^4 - 2\nu_A\cos(4\theta)}\cos^2\theta\right]. \tag{5.42}$$

When a filter is applied to channel B, the behavior of both concurrence and FEF strongly depends on the combination of the three parameters θ, ν_A and ν_B. In Fig. 5.3, we show theoretical plots for concurrence and FEF as functions of ν_B for the three different combinations of ν_A and θ specified in the legend. From the figure, one can clearly see that there are regions where concurrence and FEF behave oppositely. In particular, as the amount of filtering is increased in channel B, concurrence can decrease while, for a certain range of ν_B, the FEF increases, even turning an unfaithful state into a faithful one. This counter-intuitive behavior gives rise to a trade-off between concurrence and faithfulness and is experimentally verified in the next section.

5.4 Relation between γ and ν

In this chapter we make use of a definition of filters that is slightly different from the one we employed in the definition of PDL. The reason for this choice is that we want to stress how the behavior described in this Chapter is valid for any kind of modal filtering, of which PDL is a particular example. Here we relate the parameters that characterize the two definitions so that one can easily go from one to the other.

By comparing Eq. (5.12) with the PDL operator [30]

$$
\begin{aligned}
P &= \exp\left(-\gamma/2\right)\left[\sigma_0 \cosh\left(\gamma/2\right) + (\hat{n}\cdot\vec{\sigma})\sinh\left(\gamma/2\right)\right] \\
&= \exp\left(-\gamma/2\right)\cosh\left(\gamma/2\right)\left[\sigma_0 + (\hat{n}\cdot\vec{\sigma})\frac{\sinh\left(\gamma/2\right)}{\cosh\left(\gamma/2\right)}\right],
\end{aligned}
\tag{5.43}
$$

one can see that

$$
\nu = \frac{\sinh\left(\gamma/2\right)}{\cosh\left(\gamma/2\right)}, \qquad \mu = \exp\left(-\gamma/2\right)\cosh\left(\gamma/2\right).
\tag{5.44}
$$

The former can be inverted to give

$$
\gamma = \ln\left(\frac{1+\nu}{1-\nu}\right).
\tag{5.45}
$$

By confronting Eq.(5.27) with the well known case of a Rank-2 Bell diagonal state undergoing PDL, for which we have $C = \cos\left(2\theta\right)/\cosh\gamma$, we have

$$
\cosh\gamma = \frac{1+\nu^2}{1-\nu^2},
\tag{5.46}
$$

which leads to the same result; in fact plugging

$$
e^\gamma = \frac{1+\nu}{1-\nu}
$$

into the left-hand side of Eq. (5.46), we have

$$
\cosh\left(\gamma\right) = \frac{1}{2}\left(e^\gamma + e^{-\gamma}\right) = \frac{1}{2}\left(\frac{1+\nu}{1-\nu} + \frac{1-\nu}{1+\nu}\right) = \frac{1+\nu^2}{1-\nu^2}.
$$

Earlier in the text we noticed that the density matrix needed to be normalized, and we evaluated $\mathrm{Tr}\rho_1 = 4\mu^2(1+\nu^2)$. Using the PDL-operator notation we have

$$
4\mu^2(1+\nu^2) = e^{-\gamma}\cosh^2\left(\frac{\gamma}{2}\right)\left[1 + \frac{\sinh^2\left(\gamma/2\right)}{\cosh^2\left(\gamma/2\right)}\right] = e^{-\gamma}\cosh\left(\gamma\right),
\tag{5.47}
$$

which is consistent with the other definition of this operator.

5.5 Experiment

A schematic diagram of our experiment is shown in Fig. 5.4. Signal and idler photon pairs are generated via four-wave mixing [47] by pumping a dispersion shifted fiber (DSF) with a 50 MHz pulsed fiber laser which is filtered by a 100 GHz telecom add/drop filter centered at 1552.52 nm (ITU channel 31). The pump laser is tunable, resulting in an average number of pairs per pump pulse in the range of $0.001 - 0.1$. The signal and idler
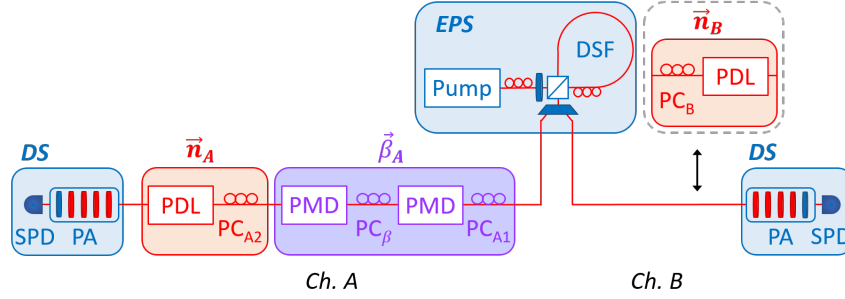
Figure 5.4: Schematic of the experimental apparatus. $\vec{\beta}_A$: birefringent element for the creation of a mixed Bell-diagonal state. $\vec{n}_A$: filtering element. $\vec{n}_B$: a second filtering element that can be introduced in the path of photon B. EPS: entangled photon source. DSF: dispersion-shifted fiber. PDL: PDL emulator. PMD: PMD emulator. PC: polarization controller. DS: detector station. PA: polarization analyzer consisting of several waveplates (red) and a polarizer (blue). SPD: single photon detector.

photons are entangled in polarization, creating a $|\phi^+\rangle$ Bell state, by arranging the DSF in a Sagnac loop with a polarizing beam splitter (PBS) [50]. The photons are then spectrally demultiplexed into 100 GHz-spaced ITU outputs after the Sagnac loop, and ITU channel 28 (1554.94nm) is sent to channel A, while ITU channel 34 (1550.12nm) is sent to channel B. These filters result in photons with a temporal duration of about 15 ps. The detector stations (DS) each include one gated single photon detector (SPD) with a detection efficiency of $\eta \sim 20\%$ and a dark count probability of $\sim 4 \times 10^{-5}$ per gate, as well as a polarization analyzer (PA) which allows for measurements at any angle on the Bloch sphere. FPGA-based controller software automatically controls the detectors and analyzers in order to perform full polarization state tomography by performing 36 different measurements [1]. Each of the 36 measurements is performed over 50 million detector gates, resulting in several thousands of detected coincidences per measurement depending on the experimental parameters. The density matrix is then reconstructed using a maximum likelihood estimation algorithm [45], and the FEF and concurrence are calculated. Due to the large amount of detected pairs per measurement, the resulting standard deviation of the FEF and concurrence (shown with the error bars in Figs. 5.5 and 5.6) is rather small.

In order to demonstrate the case of correlated faithfulness and entanglement described in Sec. 5.2, a decohering birefringent element $\vec{\beta}_A$ and a mode filter $\vec{n}_A$ are added to channel A. For polarization-entangled photons in optical fiber, polarization mode dispersion (PMD)

---

[1] Full state tomography of two qubits is achievable from the statistics of only 9 measurement settings if two detectors are used per photon [45]. However, for convenience we use a single detector per photon and take 36 total measurements, corresponding to all pairwise combinations of both eigenstates of each Pauli operator.
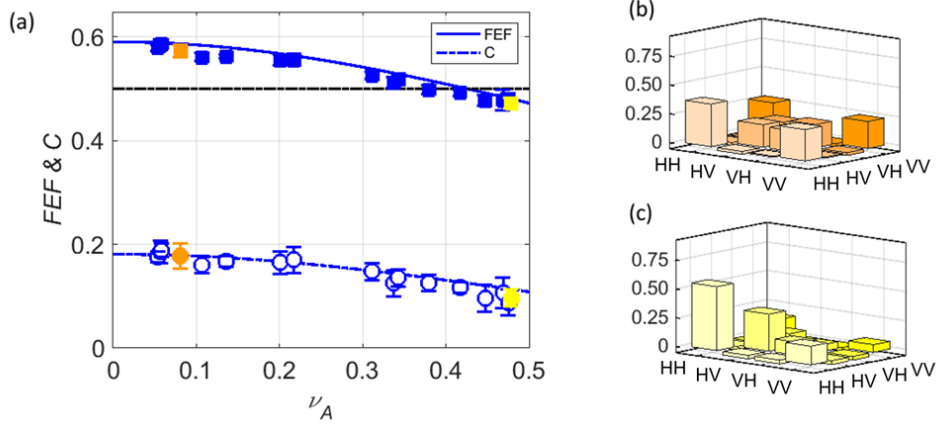
Figure 5.5: (a) Experimental data (markers) and theoretical curves for concurrence and FEF as the amount of filtering in channel A is increased with no filter present in channel B. The filter $\vec{n}_A$ is aligned along the direction $\hat{n} = \{1, 0, 0\}$ and is applied to photon A of a rank-2 Bell diagonal state. For $\nu_A \geq 0.426$, the state becomes unfaithful, but the nonzero concurrence shows that it is still entangled. Experimental density matrices corresponding to the orange and yellow markers at $\nu_A = 0.081$ and $\nu_A = 0.479$ are shown in (b) and (c), respectively.

acts as a form of decoherence, and polarization dependent loss (PDL) acts as a local filter [35, 39, 40, 42]. As such, two PMD emulators with fixed differential group delay (DGD) and variable direction on the Bloch sphere are used to implement the decohering element $\vec{\beta}_A$ which transforms the nearly-perfect $|\phi^+\rangle$ state created by the EPS into a rank-2 Bell diagonal state [43, 58, 80]. The relative angle of the birefringence vectors applied by the two PMD emulators is adjusted using the polarization controller PC_β to maximize the total DGD of the two elements, thus maximizing the decoherence of $\vec{\beta}_A$. This results in an initial state (before filtering) with concurrence $C_0 = 0.181$ which can reach the unfaithful regime with the application of an appropriate filter $\vec{n}_A$ since the initial concurrence is less than $C_0 = \sqrt{2} - 1$ as described following Eq. (14). A PDL emulator is then used to implement the mode filter $\vec{n}_A$, whose magnitude and direction on the Bloch sphere are variable.

To achieve unfaithful entanglement, the filter $\vec{n}_A$ is aligned orthogonal to the decoherence vector $\vec{\beta}_A$ using the polarization controller PC_{A2} [81], that is, the filter is aligned along the x-axis, such that $\hat{n} = \{1, 0, 0\}$ as in Sec. 5.2A. The magnitude of the filter is increased from $\nu_A = 0.054 - 0.479$, and QST is performed for each value of ν_A. The FEF and concurrence of the resulting density matrices are plotted in Fig. 5.5(a), and the density matrices corresponding to the orange and yellow markers at $\nu_A = 0.081$ and $\nu_A = 0.479$ are
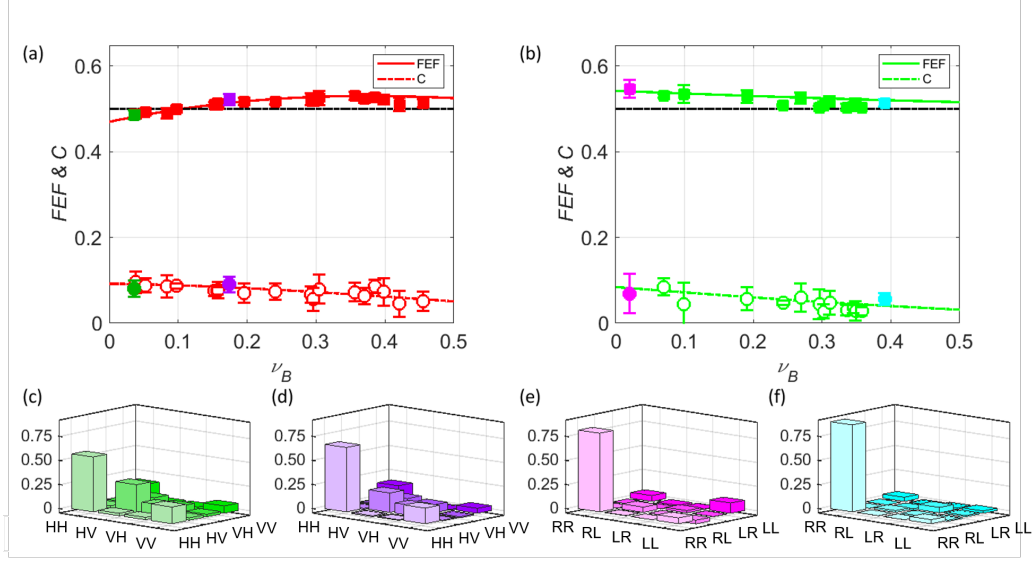
Figure 5.6: (a) - (b): Concurrence and FEF as functions of the amount (ν_B) of filtering in channel B, while ν_A is kept fixed. The markers represent experimental results, while the curves are the theoretical predictions. In (a), both filters are aligned along the direction $\hat{n} = \{1, 0, 0\}$ and $\nu_A = 0.465$ to demonstrate the anti-correlated behavior of concurrence and FEF. In (b), both filters are aligned along the direction $\hat{n} = \{0, 0, 1\}$ and $\nu_A = 0.469$ to show a configuration where the state never becomes unfaithful. The experimental density matrices in (c)-(f) refer to the markers identified by the same color.

shown in Fig. 5.5(b) and 5.5(c), respectively [2]. The behavior of the FEF and concurrence are clearly correlated as a function of ν_A, and the state becomes unfaithful, while still entangled, for $\nu_A \geq 0.426$.

Next, additional measurements are performed to demonstrate the case where faithfulness and entanglement are anti-correlated, as described in Sec. 5.3. The magnitude of the filter in channel A is fixed at $\nu_A = 0.465$, and an additional filter $\vec{n}_B$ is applied to channel B. The filter in channel B is aligned in the same direction (along the x-axis) in Stokes space as the filter in channel A using PC_B, and its magnitude is increased from $\nu_B = 0.036 - 0.455$. Tomography is performed for each value of ν_B, and the FEF and concurrence of the resulting density matrices are plotted in Fig. 5.6(a). The density matrices corresponding to the green and purple markers at $\nu_A = 0.036$ and $\nu_A = 0.174$ are shown in Fig. 5.6(c) and 5.6(d), respectively. The results clearly show that although entanglement always decreases as ν_B

---

[2] The matrices in Figs. 5.5-5.6 are expressed in the basis of the filter $\vec{n}_A$, and the x-axis in Stokes space is defined as $|H\rangle$. This basis allows for an intuitive understanding of how the filters $\vec{n}_A$ and $\vec{n}_B$ alter the density matrix; however, we note that the HV basis is rotated by $\pi/2$ (for both qubits) relative to the basis of the density matrix described by Eq. (5.26).

increases, the FEF increases over the range of $0 \leq \nu_B \leq 0.375$, and the state transitions from unfaithful to faithful at $\nu_B = 0.106$. However, the state is always faithful, i.e. the FEF asymptotically approaches 0.5 from above, when the filter in channel A is rotated such that it is collinear to the decoherence vector $\vec{\beta}_A$ (along the z-axis), and $\vec{n}_B$ is also rotated such that it remains in the same direction in Stokes space as $\vec{n}_A$. For this scenario, the magnitude of the filter in channel A is fixed at $\nu_A = 0.469$, and the magnitude of the filter in channel B is increased from $\nu_B = 0.020 - 0.392$. Tomography is once again performed for each value of ν_B, and the results are shown in Figs. 5.6(b),(e), and (f). The density matrices shown in Figs. 5.6(e) and 5.6(f) correspond to the markers of the same color at $\nu_B = 0.020$ and 0.392, respectively, in Fig. 5.6(b).

CHAPTER 6

Conclusion

In this work we have analyzed how the presence of two very common effects in fiber-optic channels, namely polarization-mode dispersion (PMD) and polarization-dependent loss (PDL), affects the distribution of polarization entanglement. We have characterized the effect of PMD as a decoherence mechanism, that turns a transmitted maximally entangled Bell state into a mixed state, and degrades the quality of its entanglement by coupling the polarization part and the time-dependent part of the two-photon state. Different scenarios were investigated, with the PMD affecting either one or both photons. We quantified the entanglement left in the photon pair by using concurrence as a metric, and we also evaluated the von Neumann entropy and the quantum mutual information which allowed us to build entropic Venn diagrams to graphically show how the presence of PMD causes a leak of information towards the environment. We discussed the effectiveness of nonlocal PMD compensation both in terms of concurrence and quantum mutual information restoration.

We then moved on to investigating the joint effect of PMD and PDL on polarization-entangled photons. To overcome the complexity introduced by a rigorous treatment of the joint presence of the two effects distributed along the photons' optical paths, we introduced a simple – yet instructive – two-element model that allowed us to extract the main characteristics of the resulting channels. For example, we discussed how the order in which PMD and PDL act on the propagating photon causes an asymmetry in the channel when a PDL element is introduced in the path of the second photon to perform nonlocal compensation, with nontrivial implications in quantum networks design. The model also has the quality of being easy to reproduce in the lab with off-the-shelf optical equipment, which allowed us to experimentally verify our findings. We have shown that, over an ample range of parameters, our two-element analytical model is quite accurate in describing the fiber channel, which makes it an effective tool for gaining insights into channel decoherence.

We concluded this work by showing how a surprisingly complicated relationship between entanglement and faithfulness emerges even for the common scenario represented by two photons in a Bell state undergoing PMD and PDL. We also showed that entanglement and

faithfulness could be traded, in some situations, with the addition of a single PDL element. The implications of these results – which have been experimentally confirmed – go beyond fiber-optic networks if one considers that PMD and PDL are just an example of decoherence and modal filtering, respectively, which are common effects in quantum communication systems.

Bibliography

[1] J. von Neumann. "Wahrscheinlichkeitstheoretischer Aufbau der Quantenmechanik". In: *Nachrichten von der Gesellschaft der Wissenschaften zu Göttingen, Mathematisch-Physikalische Klasse* 1927 (1927), pp. 245–272. URL: http://eudml.org/doc/59230.

[2] Ramamurti Shankar. *Principles of quantum mechanics*. New York, NY: Plenum, 1980. URL: https://cds.cern.ch/record/102017.

[3] Erwin Schrödinger. "Discussion of probability relations between separated systems". In: *Mathematical Proceedings of the Cambridge Philosophical Society*. Vol. 31. 4. Cambridge University Press. 1935, pp. 555–563.

[4] Ryszard Horodecki et al. "Quantum entanglement". In: *Reviews of modern physics* 81.2 (2009), p. 865.

[5] Otfried Gühne and Géza Tóth. "Entanglement detection". In: *Phys. Rep.* 474.1-6 (2009), pp. 1–75.

[6] Lluís Masanes, Yeong-Cherng Liang, and Andrew C Doherty. "All bipartite entangled states display some hidden nonlocality". In: *Physical review letters* 100.9 (2008), p. 090403.

[7] Leonid Gurvits. "Classical deterministic complexity of Edmonds' problem and quantum entanglement". In: *Proceedings of the thirty-fifth annual ACM symposium on Theory of computing*. 2003, pp. 10–19.

[8] Nikolai Wyderka. "Learning from correlations: what parts of quantum states tell about the whole". In: (2020).

[9] Ingemar Bengtsson and Karol Życzkowski. *Geometry of quantum states: an introduction to quantum entanglement*. Cambridge university press, 2017.

[10] William K Wootters. "Entanglement of formation of an arbitrary state of two qubits". In: *Physical Review Letters* 80.10 (1998), p. 2245.

[11] William K Wootters. "Entanglement of formation and concurrence." In: *Quantum Inf. Comput.* 1.1 (2001), pp. 27–44.

[12] Claude E Shannon. "A mathematical theory of communication". In: *The Bell system technical journal* 27.3 (1948), pp. 379–423.

[13] Nicolas J Cerf and Chris Adami. "Information theory of quantum entanglement and measurement". In: *Physica D: Nonlinear Phenomena* 120.1-2 (1998), pp. 62–81.

[14] Jennifer R Glick and Christoph Adami. "Quantum information theory of the Bell-state quantum eraser". In: *Physical Review A* 95.1 (2017), p. 012105.

[15] John Preskill. "Lecture notes for physics 229: Quantum information and computation". In: *California Institute of Technology* 16 (1998), p. 10.

[16] Michael M Wolf. "Quantum channels & operations: Guided tour". In: *Lecture notes available at http://www-m5. ma. tum. de/foswiki/pub M* 5 (2012).

[17] JP Gordon and H Kogelnik. "PMD fundamentals: Polarization mode dispersion in optical fibers". In: *Proc. Natl. Acad. Sci.* 97.9 (2000), pp. 4541–4550.

[18] Govind P Agrawal. "Nonlinear fiber optics". In: *Nonlinear Science at the Dawn of the 21st Century.* Springer, 2000, pp. 195–211.

[19] LE Nelson and RM Jopson. "Introduction to polarization mode dispersion in optical systems". In: *Polarization mode dispersion.* Springer, 2004, pp. 1–33.

[20] R Ulrich and A Simon. "Polarization optics of twisted single-mode fibers". In: *Applied optics* 18.13 (1979), pp. 2241–2251.

[21] Craig D Poole and Jonathan Nagel. "Polarization effects in lightwave systems". In: *Optical Fiber Telecommunications IIIA* (1997), pp. 114–161.

[22] Craig D Poole. "Statistical treatment of polarization dispersion in single-mode fiber". In: *Optics Letters* 13.8 (1988), pp. 687–689.

[23] Franco Curti et al. "Statistical treatment of the evolution of the principal states of polarization in single-mode fibers". In: *Journal of Lightwave Technology* 8.8 (1990), pp. 1162–1166.

[24] Mark Shtaif and Antonio Mecozzi. "Modelling of polarization mode dispersion in optical communications systems". In: *Journal of Optical and Fiber Communications Reports* 1.3 (2004), pp. 248–265.

[25] R Clark Jones. "A new calculus for the treatment of optical systems. IV." In: *Josa* 32.8 (1942), pp. 486–493.

[26] CD Poole and RE Wagner. "Phenomenological approach to polarisation dispersion in long single-mode fibres". In: *Electronics Letters* 22.19 (1986), pp. 1029–1030.

[27] Craig D Poole, Jack H Winters, and Jonathan A Nagel. "Dynamical equation for polarization dispersion". In: *Optics Letters* 16.6 (1991), pp. 372–374.

[28] GJ Foschini and CD Poole. "Statistical theory of polarization dispersion in single mode fibers". In: *Journal of Lightwave Technology* 9.11 (1991), pp. 1439–1456.

[29] Mark Shtaif and Antonio Mecozzi. "Study of the frequency autocorrelation of the differential group delay in fibers with polarization mode dispersion". In: *Optics letters* 25.10 (2000), pp. 707–709.

[30] Jay N Damask. *Polarization optics in telecommunications.* Vol. 101. Springer Science & Business Media, 2004.

[31] Nicolas Gisin. "Statistics of polarization dependent losses". In: *Optics communications* 114.5-6 (1995), pp. 399–405.

[32] N Frigo. "A generalized geometrical representation of coupled mode theory". In: *IEEE journal of quantum electronics* 22.11 (1986), pp. 2131–2140.

[33] Nicolas Gisin. "PMD & PDL". In: *Polarization Mode Dispersion*. Springer, 2004, pp. 113–125.

[34] Mark Shtaif and Oren Rosenberg. "Polarization-dependent loss as a waveform-distorting mechanism and its effect on fiber-optic systems". In: *J. Light. Technol.* 23.2 (2005), p. 923.

[35] Mark Shtaif, Cristian Antonelli, and Misha Brodsky. "Nonlocal compensation of polarization mode dispersion in the transmission of polarization entangled photons". In: *Opt. Express* 19.3 (2011), pp. 1728–1733.

[36] Brian J Smith et al. "Photon pair generation in birefringent optical fibers". In: *Optics express* 17.26 (2009), pp. 23589–23602.

[37] Piotr Badziag et al. "Local environment can enhance fidelity of quantum teleportation". In: *Physical Review A* 62.1 (2000), p. 012311.

[38] Ting Yu and JH Eberly. "Evolution from entanglement to decoherence of bipartite mixed" X" states". In: *Quantum Information & Computation* 7.5 (2007), pp. 459–468.

[39] Misha Brodsky et al. "Loss of polarization entanglement in a fiber-optic system with polarization mode dispersion in one optical path". In: *Opt. Lett.* 36.1 (2011), pp. 43–45.

[40] Cristian Antonelli, Mark Shtaif, and Misha Brodsky. "Sudden death of entanglement induced by polarization mode dispersion". In: *Phys. Rev. Lett.* 106.8 (2011), p. 080404.

[41] Misha Brodsky, Peter Magill, and Nicholas J Frigo. "Polarization-mode dispersion of installed recent vintage fiber as a parametric function of temperature". In: *IEEE Photonics Technology Letters* 16.1 (2004), pp. 209–211.

[42] Daniel E Jones, Brian T Kirby, and Michael Brodsky. "Tuning quantum channels to maximize polarization entanglement for telecom photon pairs". In: *npj Quantum Inf.* 4.1 (2018), p. 58.

[43] Brian T Kirby, Daniel E Jones, and Michael Brodsky. "Effect of polarization dependent loss on the quality of transmitted polarization entanglement". In: *J. Light. Technol.* 37.1 (2019), pp. 95–102.

[44] NuCrypt. *Quantum optical instrumentation.* URL: http://nucrypt.net/quantum-optical-instrumentation.html.

[45] Joseph B Altepeter, Evan R Jeffrey, and Paul G Kwiat. "Photonic state tomography". In: *Adv. Atom. Mol. Opt. Phys.* 52 (2005), pp. 105–159.

[46] OZ Optics Polarization Dependent Loss Emulator. *Quantum optical instrumentation.* URL: https://www.ozoptics.com/ALLNEW_PDF/DTS0065.pdf.

[47] Marco Fiorentino et al. "All-fiber photon-pair source for quantum communications". In: *IEEE Photonics Technol. Lett.* 14.7 (2002), pp. 983–985.

[48] Daniel E Jones, Brian T Kirby, and Michael Brodsky. "Joint Characterization of Two Single Photon Detectors with a Fiber-based Source of Entangled Photon Pairs". In: *Frontiers in Opt.* Opt. Soc. of America. 2017, JW4A–37.

[49] Daniel E Jones, Brian T Kirby, and Michael Brodsky. "In-situ calibration of fiber-optics entangled photon distribution system". In: *IEEE Photonics Soc. Summer Topical Meeting Ser.* IEEE. 2017, pp. 123–124.

[50] Shawn X Wang and Gregory S Kanter. "Robust multiwavelength all-fiber source of polarization-entangled photons with built-in analyzer alignment signal". In: *IEEE J. Sel. Top. Quantum Electron.* 15.6 (2009), pp. 1733–1740.

[51] Misha Brodsky, Nicholas J. Frigo, and Moshe Tur. "Polarization mode dispersion". In: *Optical Fiber Telecommunications A*. Ed. by Ivan P. Kaminow, Tingye Li, and Alan E. Willner. Fifth. Optics and Photonics. Burlington: Academic Press, 2008, pp. 605 –669. DOI: https://doi.org/10.1016/B978-0-12-374171-4.00017-4.

[52] M. Boroditsky et al. "In-service measurements of polarization-mode dispersion and correlation to bit-error rate". In: *IEEE Photonics Technology Letters* 15.4 (2003), pp. 572–574.

[53] Antonio Mecozzi et al. "Characterization of the time dependence of polarization mode dispersion". In: *Optics letters* 29.22 (2004), pp. 2599–2601.

[54] C. Antonelli et al. "PMD-induced penalty statistics in fiber links". In: *IEEE Photonics Technology Letters* 17.5 (2005), pp. 1013–1015.

[55] M. Brodsky et al. "Persistence of spectral variations in DGD statistics". In: *Opt. Express* 13.11 (2005), pp. 4090–4095. DOI: 10.1364/OPEX.13.004090.

[56] Odile Liboiron-Ladouceur et al. "Polarization-dependent gain in SOA-based optical multistage interconnection networks". In: *J. Light. Technol.* 24.11 (2006), pp. 3959–3967.

[57] Cristian Antonelli et al. "Stokes-Space Analysis of Modal Dispersion of SDM Fibers With Mode-Dependent Loss: Theory and Experiments". In: *Journal of Lightwave Technology* 38.7 (2019), pp. 1668–1677.

[58] Daniel E Jones et al. "Exploring classical correlations in noise to recover quantum information using local filtering". In: *New J. Phys.* 22.7 (2020), p. 073037.

[59] Adrian Kent, Noah Linden, and Serge Massar. "Optimal entanglement enhancement for mixed states". In: *Phys. Rev. Lett.* 83.13 (1999), p. 2656.

[60] Noah Linden, Serge Massar, and Sandu Popescu. "Purifying noisy entanglement requires collective measurements". In: *Phys. Rev. Lett.* 81.15 (1998), p. 3279.

[61] Frank Verstraete, Jeroen Dehaene, and Bart DeMoor. "Local filtering operations on two qubits". In: *Phys. Rev. A* 64.1 (2001), p. 010101.

[62] Gabriele Riccardi et al. "Directional asymmetry of quantum channels". In: *Frontiers in Optics.* Optical Society of America. 2020, FM7A–7.

[63] Sevag Gharibian. "Strong NP-hardness of the quantum separability problem". In: *Quantum Inf. Comput.* 10.3 (2010), pp. 343–360.

[64] Maciej Lewenstein et al. "Optimization of entanglement witnesses". In: *Physical Review A* 62.5 (2000), p. 052310.

[65] Barbara M Terhal. "Detecting quantum entanglement". In: *Theor. Comput. Sci.* 287.1 (2002), pp. 313–335.

[66] Michał Horodecki, Paweł Horodecki, and Ryszard Horodecki. "Separability of n-particle mixed states: necessary and sufficient conditions in terms of linear maps". In: *Physics Letters A* 283.1-2 (2001), pp. 1–7.

[67] Mirjam Weilenmann et al. "Entanglement detection beyond measuring fidelities". In: *Phys. Rev. Lett.* 124.20 (2020), p. 200502.

[68] Mohamed Bourennane et al. "Experimental detection of multipartite entanglement using witness operators". In: *Phys. Rev. Lett.* 92.8 (2004), p. 087902.

[69] Otfried Gühne, Yuanyuan Mao, and Xiao-Dong Yu. "Geometry of faithful entanglement". In: *Physical Review Letters* 126.14 (2021), p. 140503.

[70] Yongtao Zhan and Hoi-Kwong Lo. "Detecting Entanglement in Unfaithful States". In: *arXiv preprint arXiv:2010.06054* (2020).

[71] Matthias D Lang and Carlton M Caves. "Quantum discord and the geometry of Bell-diagonal states". In: *Phys. Rev. Lett.* 105.15 (2010), p. 150501.

[72] Ryszard Horodecki, Michał Horodecki, and Paweł Horodecki. "Teleportation, Bell's inequalities and inseparability". In: *Phys. Lett. A* 222.1-2 (1996), pp. 21–25.

[73] Michał Horodecki, Paweł Horodecki, and Ryszard Horodecki. "General teleportation channel, singlet fraction, and quasidistillation". In: *Phys. Rev. A* 60.3 (1999), p. 1888.

[74] H. L. Albrecht Q. and D. F. Mundarain. "Maximal singlet fraction vs. maximal achievable fidelity as proper entanglement measures". In: *arXiv preprint arXiv:2008.13063* (2020).

[75] J Grondalski, DM Etlinger, and DFV James. "The fully entangled fraction as an inclusive measure of entanglement applications". In: *Phys. Lett. A* 300.6 (2002), pp. 573–580.

[76] Frank Verstraete and Henri Verschelde. "Fidelity of mixed states of two qubits". In: *Phys. Rev. A* 66.2 (2002), p. 022307.

[77] Charles H Bennett et al. "Mixed-state entanglement and quantum error correction". In: *Phys. Rev. A* 54.5 (1996), p. 3824.

[78] Xiao-Dong Yu et al. "Quantum-inspired hierarchy for rank-constrained optimization". In: *arXiv preprint arXiv:2012.00554* (2020).

[79] Daniele Cozzolino et al. "High-Dimensional Quantum Communication: Benefits, Progress, and Future Challenges". In: *Advanced Quantum Technologies* 2.12 (2019), p. 1900038.

[80] Gabriele Riccardi et al. "Simultaneous Decoherence and Mode Filtering in Quantum Channels: Theory and Experiment". In: *Phys. Rev. Applied* 15.1 (2021), p. 014060.

[81] Daniel E Jones et al. *Experimental Procedure to Characterize the Effects of Filtering and Decoherence on Polarization Entangled Photons*. Tech. rep. DEVCOM U.S. Army Research Laboratory Adelphi United States, 2020.